

Acta Universitatis
Lappeenrantaensis
829



Andrey Saren

**TWIN BOUNDARY DYNAMICS IN MAGNETIC
SHAPE MEMORY ALLOY Ni-Mn-Ga FIVE-LAYERED
MODULATED MARTENSITE**



Andrey Saren

TWIN BOUNDARY DYNAMICS IN MAGNETIC SHAPE MEMORY ALLOY Ni-Mn-Ga FIVE-LAYERED MODULATED MARTENSITE

Thesis for the degree of Doctor of Science (Technology) to be presented with due permission for public examination and criticism in the Auditorium of the Student Union House at Lappeenranta University of Technology, Lappeenranta, Finland on the 10th of December, 2018, at noon.

Acta Universitatis
Lappeenrantaensis 829

- Supervisor Professor Kari Ullakko
LUT School of Engineering Science
Lappeenranta University of Technology
Finland
- Reviewers Professor Simo-Pekka Hannula
Department of Chemistry and Materials Science
Aalto University
Finland
- Professor Pasi Kallio
Faculty of Biomedical Sciences and Engineering
Tampere University of Technology
Finland
- Opponent Assistant Professor Markus Chmielus
Department of Mechanical Engineering and Materials Science
University of Pittsburgh
USA

ISBN 978-952-335-304-6
ISBN 978-952-335-305-3 (PDF)
ISSN-L 1456-4491
ISSN 1456-4491

Lappeenrannan teknillinen yliopisto
LUT Yliopistopaino 2018

Abstract

Andrey Saren

Twin boundary dynamics in magnetic shape memory alloy Ni-Mn-Ga five-layered modulated martensite

Lappeenranta 2018
98 pages

Acta Universitatis Lappeenrantaensis 829
Diss. Lappeenranta University of Technology

ISBN 978-952-335-304-6
ISBN 978-952-335-305-3 (PDF)
ISSN-L 1456-4491
ISSN 1456-4491

Ni-Mn-Ga magnetic shape memory (MSM) alloys are considered to be highly promising materials for actuation, damping, sensing and energy harvesting applications, due to the unique combination of a large transformation strain of ~6–12%, high mobility of twin boundaries (TBs) and fast, sub-millisecond response to magnetic fields. The investigation of TB dynamics in these alloys is of great importance, since the TB mobility determines the dynamic properties of MSM-based devices. However, there are only few studies on TB dynamics in Ni-Mn-Ga, having contradictory results. In these works, based on different displacement measurement techniques, only estimations of average twin boundary velocity were made. In addition, the previous studies dealt with uncontrollable TBs type and twin variants arrangement, or multiple TBs motion.

In the present work, for the first time, the TB dynamics in Ni₅₀Mn₂₈Ga₂₂ five-layered modulated martensite was investigated on the level of single TB motion induced by a pulsed magnetic field, combined with direct velocity measurements. A unique experimental setup based on laser Doppler vibrometry technique was developed to precisely measure transient velocities of single TBs propagating through the sample, and high-speed camera imaging was used to directly observe the TB motion. The results demonstrate that primarily inertia and internal friction affect the TB motion and limit the TB velocity, whereas magnetic field-dependent resistance forces such as magneto-static forces, torques and eddy currents play only a negligible role in TB dynamics, up to applied magnetic fields of 2.5 T.

A macroscopic model was developed to describe the variable-mass problem of single TB motion. The model was applied to extract the motion parameters from the measured velocity data and for simulation of the experimental results at macro- and microscale, for bulky millimetre-sized samples and micropillars. It was found that the observed velocity limitations arise from a strong dependence of twinning stress (TS) on the TB velocity. For type 1 TB, the TS drastically increases from its quasi-static value of ~0.6 to ~3 MPa

limiting the TB velocity to 3-7 m/s. For type 2 TBs, a gradual increase of the TS from ~ 0.1 MPa to ~ 2 MPa was observed with TB velocities reaching 33-39 m/s. The results obtained for Ni-Mn-Ga micropillars demonstrate a possibility of microscale MSM-based devices fabrication having working frequencies of the order of 100 kHz. The presented experimental observations and concepts differ from the known kinetic relation approach.

The results are important for the MSM-based applications development, especially for high frequency and high-speed actuation.

Keywords: Ni-Mn-Ga, Magnetic shape memory, Ferromagnetic shape memory, Twin boundary, Twinning stress, Dynamic phenomena, Modelling, Magnetic field actuation

Acknowledgements

This work was carried out in the Material Physics Laboratory, located in Savonlinna, Finland, which belongs to the School of Engineering Sciences at Lappeenranta University of Technology, Finland, between 2015 and 2018.

First I would like to express my gratitude to my supervisor, Prof. Kari Ullakko, for giving me the opportunity to start and conduct this exciting research, his support and kindness providing a good working environment.

I greatly appreciate the help from Dr. Juhani Tellinen and Dr. Alexei Sozinov who were always ready to discuss and advice the results and ideas.

As well, I would like to thank M.Sc. Denys Musiienko, Ph.D. Aaron Smith, B.Eng. Elmar Bernhardt and laboratory technician Janne Huimasalo for their cooperation and contribution during the studies.

The financial support from the Finnish Academy of Sciences (grant numbers 277996 and 287016) is greatly acknowledged.

Last, but not least, I thank my family for the patience and support during all this time.

Andrey Saren
August 2018
Savonlinna, Finland

Contents

Abstract

Acknowledgements

Contents

List of publications 9

Nomenclature 11

1 Introduction 13

- 1.1 Crystal structure and twinning in Ni-Mn-Ga alloys..... 14
 - 1.1.1 Crystal structure of Ni-Mn-Ga alloys 14
 - 1.1.2 Twinning in 5M Ni-Mn-Ga martensite..... 15
- 1.2 Twin boundary motion in 5M Ni-Mn-Ga martensite..... 18
 - 1.2.1 Mechanically induced twin boundary motion..... 18
 - 1.2.2 Magnetically induced twin boundary motion 19
 - 1.2.3 Experimental studies and modelling approaches on twin boundary dynamics 22
- 1.3 Concluding remarks 27
 - 1.3.1 Crystal structure and twinning 27
 - 1.3.2 Twin boundary dynamics 28
- 1.4 Motivation for this study 29

2 Objectives of the research 31

3 Macroscopic model for twin boundary motion 33

- 3.1 Geometrical considerations 33
- 3.2 Variable-mass system equation 34
- 3.3 Different actuation modes for single twin boundary motion 36
- 3.4 Effects of the sample's shape and size 37
- 3.5 Magnetic field-induced stress and multiple twin boundaries motion..... 39
- 3.6 Concluding remarks 41

4 Materials and methods 43

- 4.1 Ni-Mn-Ga samples 43
- 4.2 Twinning stress measurements..... 44
- 4.3 Magnetic anisotropy measurements 44
- 4.4 Pulsed magnetic field actuation setup 45
- 4.5 High-speed camera setup..... 47
- 4.6 Modelling the twin boundary motion..... 49

5 Results and discussion 51

- 5.1 MSM samples characterization 51

5.1.1	Twinning stress measurements	51
5.1.2	Magnetic anisotropy measurements.....	53
5.2	Single twin boundary motion in saturation magnetic field	54
5.2.1	Preliminary studies and development of the experimental setup	54
5.2.2	Single twin boundary motion characterized by laser Doppler vibrometry	55
5.2.3	Direct observation of twin boundaries motion.....	57
5.3	Velocity-dependent twinning stress	60
5.4	Single twin boundary motion at fields below saturation.....	65
5.5	Multiple twin boundaries motion in saturation magnetic field	70
5.6	Pulsed magnetic field actuation of MSM micropillars.....	74
5.7	Discussion on the previous studies on twin boundary dynamics	79
5.7.1	Magnitude and limits for twin boundary velocity.....	79
5.7.2	Applicability of the kinetic relation approach for twin boundary dynamics	80
6	Conclusions	83
6.1	Contribution to the field	83
6.2	Summary of the Thesis results	84
6.3	Future work	86
	References	89
	Appendix A: Electrical circuit for pulsed magnetic field actuation setup	95
	Appendix B: MATLAB code example for the model	97
	Publications	

List of publications

This thesis is based on the following papers. The rights have been granted by publishers to include the papers in dissertation.

- I. Saren, A., Musiienko, D., Smith, A.R., Ullakko, K. (2016). Pulsed magnetic field-induced single twin boundary motion in Ni–Mn–Ga 5M martensite: A laser vibrometry characterization. *Scripta Materialia*, 113, pp.154-157.
- II. Saren, A., Nicholls, T., Tellinen, J., Ullakko, K. (2016). Direct observation of fast-moving twin boundaries in magnetic shape memory alloy Ni–Mn–Ga 5M martensite. *Scripta Materialia*, 123, pp.9-12.
- III. Saren, A., Ullakko, K. (2017). Dynamic twinning stress and viscous-like damping of twin boundary motion in magnetic shape memory alloy Ni-Mn-Ga. *Scripta Materialia*, 139, pp.126-129.
- IV. Saren, A., Tellinen, J., Musiienko, D., Ullakko, K. (2016). Fast Actuation of Magnetic Shape Memory Material Ni-Mn-Ga Using Pulsed Magnetic Field. In: Borgmann, H., ed., *Proceedings of the 15th International Conference on New Actuators*, pp.101-103. Bremen: MESSE BREMEN, WFB Wirtschaftsförderung Bremen GmbH.

Author's contribution

The Author is the principal author and investigator in papers I – IV. He developed and assembled the experimental setup for pulsed magnetic field actuation, prepared and characterized the samples, conducted and interpreted the experiments, developed the model and wrote the manuscripts. M.Sc. Denys Musiienko conducted the quasi-static twinning stress measurements in Publication I. B.Sc. (currently, Ph.D.) Aaron R. Smith participated in setup and sample preparation in Publication I. Tim Nicholls operated the high-speed camera in Publication II. Dr. Juhani Tellinen contributed to the pulse generator circuit development and discussions in Publications II and IV. Prof. Kari Ullakko provided overall scientific guidance and participated in the preparation of the manuscripts in Publications I and II.

Nomenclature

List of symbols

a, b and c	lattice parameters	Å
A	sample's cross-sectional area	m ²
A_f	austenite finish temperature	K
A_s	austenite start temperature	K
α	angle in the model	deg
β	angle in the model	deg
γ	angle between a and b	deg
γ_0	amplitude of the Peierls barrier in the "kinetic relation" approach	J/m ²
ΔG	equilibrium energy difference between two differently oriented variants in magnetic field	J/m ³
ε_0	transformation strain	–
\mathbf{F}	force vector	–
F_{ext}	external force	N
F_{mag}	magnetic field-induced force	N
F_{res}	resistance force	N
f	frequency	Hz
g	driving force for twin boundary motion in the "kinetic relation" approach	J/m ³
g_0	threshold driving force in the "kinetic relation" approach	J/m ³
H	magnetic field strength	A/m
H_a	anisotropy field	A/m
H_s	saturation field	A/m
H_{sw}	switching field	A/m
I	electrical current	A
K_u	uniaxial magnetic anisotropy constant	J/m ³
k_0	coefficient in the model	–
L	twin boundary position	m
l	length of the solenoid	m
M_f	martensite finish temperature	K
M_s	martensite start temperature	K
M_S	saturation magnetization	A/m
m	mass	kg
μ	mobility coefficient in the "kinetic relation" approach	m/(Pa·s)
μ_0	magnetic constant (permeability of free space)	H/m
N	number of turns in the coil	–
R	average coil radius	m
ρ	volumetric mass density	kg/m ³
σ_{mag}	magnetic field-induced stress	Pa
σ_{res}	resistance stress	Pa
σ_{tw}	twinning stress	Pa

T	temperature	K
T_C	Curie temperature	K
t	time	s
v	velocity of the moving variant	m/s
v_C	contraction velocity	m/s
v_{TB}	twin boundary velocity	m/s

Abbreviations

5M	modulated five-layered martensite (also referred to as 10M)
7M	modulated seven-layered martensite (also referred to as 14M)
AC	alternating current
bcc	body-centered cubic
DC	direct current
EBSD	electron backscatter diffraction
FIB	focused ion beam
fps	frames per second
FSMA	ferromagnetic shape memory alloy
L2 ₁	crystal structure in Strukturbericht notation
LDV	laser Doppler vibrometer
LED	light-emitting diode
MFIS	magnetic field-induced strain
MIR	magnetically induced reorientation
MSM	magnetic shape memory
NM	non-modulated martensite
SEM	scanning electron microscopy
TB	twin boundary
TS	twinning stress

1 Introduction

Magnetic shape memory (MSM) alloys, alternatively called ferromagnetic shape memory alloys (FSMAs), are a particular class of shape memory alloys, which produce force and deformation in response to a magnetic field (Aaltio *et al.*, 2016). Unlike the thermally-responsive shape memory alloys in which the deformation is produced because of austenite-martensite transformation within a narrow temperature range, in MSM alloys externally applied magnetic field reorients the martensitic crystal lattice by means of twin boundaries (TBs) motion.

Since the first demonstration of the MSM-effect in Ni₂MnGa alloy by Ullakko *et al.* (1996), a lot of efforts was applied to search and investigate different MSM alloy families. Nevertheless, Ni-Mn-Ga-based MSM alloys still are considered as the most significant due to the unique combination of a large transformation strain of ~6–12%, high TB mobility and fast, sub-millisecond response to magnetic fields. Possible application areas of MSM alloys include actuating (based on large and fast deformation), energy harvesting (conversion of the mechanical vibration energy to electrical energy¹), vibration damping (magnetically controlled stiffness) and sensing (magnetization change under deformation). The investigation of TB dynamics in MSM alloys is of great importance, since the TB mobility dictates the dynamic properties of any MSM-based devices.

In the present work, new experimental and modelling approaches have been developed and exploited which allow much more precise characterization and deeper understanding of the TB motion in the MSM alloy Ni-Mn-Ga five-layered modulated (5M) martensite, as compared to the previous studies. The TB dynamics is characterized in a wide range of TB velocities, up to 7 m/s for type 1 and 39 m/s for type 2 TBs, under applied pulsed magnetic fields up to 2.5 T.

In this chapter, a brief literature review is provided which focuses on the crystal structure, twinning and TB motion in 5M Ni-Mn-Ga martensite, summarizes the known experimental results and modelling approaches related to the studies on TB dynamics in this material, and presents motivation for the study. The research objectives are formulated in Chapter 2. Chapter 3 presents the macroscopic mathematical model developed for single TB motion, an overview of the applicable actuation modes and briefly discusses multiple TBs motion. Chapter 4 describes the experimental setups, methods and materials used in this research. In Chapter 5, the experimental and modelling results are summarized and discussed. Chapter 6 provides the conclusions of the work.

The Author's contribution is described in the preambles to Chapters 3, 4 and 5.

¹ The mechanism for the energy harvesting is stress-induced rearrangement of the twin variants leading to change of the permeability that cause oscillations of the magnetic flux in the yoke where the MSM element is placed. This generates electrical energy by inducing an alternating current within a pick-up coil.

1.1 Crystal structure and twinning in Ni-Mn-Ga alloys

1.1.1 Crystal structure of Ni-Mn-Ga alloys

The family of $\text{Ni}_{2+x}\text{Mn}_{1-x}\text{Ga}_{1-y}$ alloys belongs to the Heusler ternary intermetallic compounds with the general formula X_2YZ . The stoichiometric Ni_2MnGa has the $L2_1$ structure at room temperature which can be represented by a bcc lattice, as shown in Figure 1.1. The cubic lattice constant a is 5.825 \AA at room temperature and the number of formula units per unit cell is 4. Down to $T \sim 200 \text{ K}$, Ni_2MnGa remains in the $L2_1$ parent phase, and then it undergoes a first-order phase transition from austenite to a martensitic tetragonal phase, with $c/a < 1$. At low temperatures the parameters of the tetragonal lattice are $a=b=5.920 \text{ \AA}$ and $c=5.566 \text{ \AA}$, with $c/a=0.94$ (Webster *et al.*, 1984). In addition, the stoichiometric Ni_2MnGa undergoes a ferromagnetic transformation with a Curie temperature of $T_C=376 \text{ K}$.

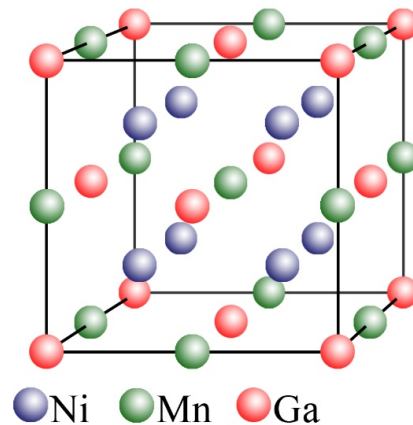


Figure 1.1: The $L2_1$ structure of the austenitic phase of Ni_2MnGa .

Almost all parameters of non-stoichiometric Ni-Mn-Ga alloys are very sensitive to the chemical composition. The samples' composition strongly affects the temperatures of phase transformations and the formation of different modulated structures in the martensitic state. On the other hand, the Curie temperature, T_C , of Ni-Mn-Ga alloys in parent, austenitic phase approximately locates in the range of $350\text{--}380 \text{ K}$ (Söderberg *et al.*, 2006; Xu *et al.*, 2013), almost independent of composition when Mn content is above 20-25 at%. The composition is usually mapped into number of valence electrons per atom, e/a , which is a widely used parameter for classifying the concentration dependence of the martensitic transformation temperature – see, *e.g.*, review by Aaltio *et al.* (2016). According to this review, the martensitic transformation temperature increases with

increasing e/a , and T_C keeps at about 370 K when the composition is close to stoichiometric. When composition is further deviated from the stoichiometry, the T_C decreases with increased electron concentration.

It has been shown that the martensite crystal structure is strongly dependent on both the alloy composition and temperature. The stoichiometric Ni_2MnGa ($e/a=7.5$) has a modulated five-layered martensite (referred to as 5M or 10M in the literature) which has approximately tetragonal lattice with $a \approx b$ and $c < a$. According to Heczko *et al.* (2009), for alloys with larger electron concentrations, the 5M martensite can transform upon cooling into seven-layered (7M or 14M) martensite (orthorhombic phase with $c < b < a$) and then into a non-modulated (NM) tetragonal phase with $a = b$ and $c > a$. Other transformation paths are also possible, including austenite \rightarrow 7M \rightarrow NM, or austenite \rightarrow NM above $e/a=7.7-7.8$. In addition, the intermartensitic transformations can be induced by a mechanical stress (Martynov and Kokorin, 1992). In the literature, there are two interpretations of modulated martensite crystal structure. The first one considers it as a long range closed packed layered structure (Pons *et al.*, 2005). The second approach, called adaptive phase theory, considers the layered structure as twin related domains with a few atomic planes width (Kaufmann *et al.*, 2010).

According to the neutron diffraction experiments by Webster *et al.* (1984), for the stoichiometric alloy Ni_2MnGa , a magnetic moment of $4.17 \mu_B$ (per formula unit) is largely confined to the Mn sites, but probably with a small moment $< 0.3 \mu_B$ associated with the Ni sites. The Mn atoms align ferromagnetically with a calculated moment of about $3.5 \mu_B$. Magnetization and theoretical studies by Enkovaara *et al.* (2003) revealed that doping has a strong effect on the saturation magnetization and the extra Mn is antiferromagnetically aligned to the other atoms in the lattice. The ordering of the extra Mn also affects the appearance of the tetragonal and orthorhombic structures and the magnetic anisotropy energy. Lázpita *et al.* (2011) found that in off-stoichiometric alloys having excess Mn and deficient in Ga, the ferromagnetic/antiferromagnetic coupling of the Mn atoms depends on the occupation site. The Mn atoms occupying Ga sites, which are nearest neighbours to properly sited Mn, couple antiferromagnetically to the dominant moment. In contrast, Mn atoms at Ga sites, which are nearest neighbours to Mn at Ni sites, couple ferromagnetically. Mn at Ni sites is always antiferromagnetic. It was also found that in Mn and Ni excess alloys, excess Ni occupies Mn sites, displacing Mn atoms into Ga positions. Therefore, the stoichiometric Ni_2MnGa has a maximum magnetic moment, which decreases with deviation from the stoichiometric composition.

1.1.2 Twinning in 5M Ni-Mn-Ga martensite

The five-layered modulated Ni-Mn-Ga martensite exhibiting typical transformation strain of $\varepsilon_0 = 1 - c/a \approx 6\%$, has approximately tetragonal lattice with less than 0.5 % difference between a and b , and a slight monoclinic distortion (the angle γ between a and b deviates from 90° less than 0.5°) (Sozinov *et al.*, 2011). Usually, the lattice is described in reference to the “cubic coordinates” of the parent austenite. In 5M Ni-Mn-Ga martensite,

the shortest c -axis is the axis of easy magnetization (in which the cell magnetic moment is oriented). Generally, after cooling the sample from the high-temperature cubic austenite, a very complex self-accommodated twin microstructure appears, composed from multiple twin variants with nearly perpendicular c -axis orientations. The twinned structure can be further modified by application of a magnetic field and/or a mechanical stress. Thus, numerous martensitic twin variants can coexist in a single crystalline sample, being connected by twin boundaries, as it is schematically shown in Figure 1.2(a). Application of a magnetic field favours such variants in which the easy magnetization c -axis is aligned along the field, leading to contraction of the sample along the field direction – see Figure 1.2(b). This effect is called magnetically induced reorientation (MIR). The sample contracts also under a compressive mechanical stress as it favours the variants with the shortest c -axis aligned with the force. Alternatively, the sample would elongate in a perpendicular magnetic field or under application of a tensile stress. In all these cases, the twin variants change their fractions thanks to the TB motion through which the reorientation of the crystal structure occurs. It should be noted, however, that deformation twinning is a result of application of a *shear* stress arising from shear forces, which are pair of equal and opposing forces acting on opposite sides of a crystal and applied along the twinning plane – see Figure 1.3. Thus, when a *normal* stress is applied to a sample, only the force component which is parallel to the twinning plane, causes the crystal lattice reorientation.

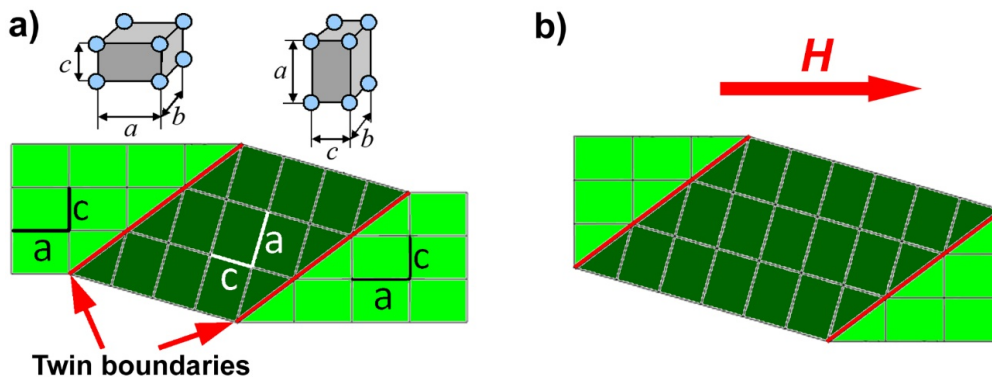


Figure 1.2: (a) A schematic view of a Ni-Mn-Ga sample with three-variant twinned structure and two TBs connecting the variants with differently oriented easy magnetization c -axis. The upper part shows two orientations of the tetragonal cells composing the variants. (b) Magnetically induced reorientation of the crystal lattice through TB motion (compare with (a)) by a magnetic field applied along the direction marked with the red arrow. The a/c ratio in (a, b) is enlarged for clarity.

Two crystallographically different types of TBs have been observed in 5M Ni-Mn-Ga: type 1 having rational twinning plane and irrational shear direction (twinning plane

between *reflection* twins²), and type 2 with irrational twinning plane and rational shear direction (twinning plane between *rotation* twins) (Sozinov *et al.*, 2011; Straka *et al.*, 2011). Different TB types differ in the projections on two opposite sample's facets (implying that the sample is cut closely to $\{100\}$ planes of cubic austenite): type 1 boundary exhibits nearly parallel projection relative to the crystal's edges while that of type 2 is inclined by about 6° . The projections on the other two facets for both types are the same and have nearly 45° projections (like in Figure 1.2). Both TB types are movable under mechanical or magnetic field-induced stress but exhibit substantially different properties that will be discussed in the following sections.

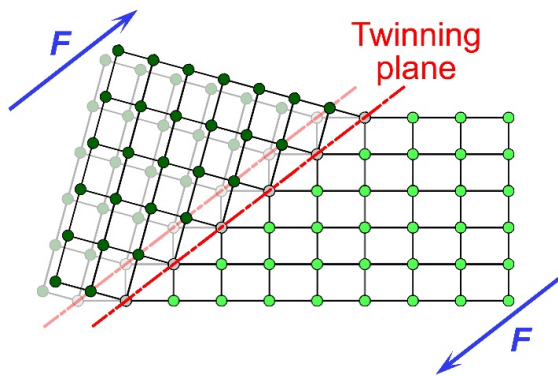


Figure 1.3: Deformation twinning in a tetragonal lattice caused by a shear stress. Twinning plane is denoted by a dash-dotted red line, and the applied shear forces by blue arrows. The correspondent crystal lattice reorientation and twinning plane shift are shown.

Recent studies reveal that rather complex microstructures can be observed at the mobile interfaces between martensitic variants, as compared to the simplified *a-c* twins depicted in Figure 1.2. Because of the monoclinic lattice symmetry, the 5M martensite is able to form modulation twins and *a-b* twins, which are such types of twins that the orientation of the *c*-axis does not change over the twinning plane. Fine laminates of these types of twins were found in the vicinity of the mobile TBs by Straka *et al.* (2011), Heczko *et al.* (2013b) and Chulist *et al.* (2013). Therefore, the mobile TB is a macro-twin interface between two laminates. Seiner *et al.* (2014) presented a continuum-based model of microstructures forming at the macro-twin interfaces in thermoelastic martensites and applied this model to mobile interfaces in 5M modulated Ni-Mn-Ga martensite.

In contrast to the complex twin microstructure and despite of the differences between the TB types, the magnetic domain structure in the vicinity of type 1 and type 2 TBs is very similar and simple (Heczko *et al.*, 2015). The authors conclude that the complex twin

² See the detailed description of the twins crystallography, *e.g.*, in Kelly *et al.* (2000).

structure does not influence on the domain structure. In addition, Lai (2009) demonstrated earlier that there is no 180° domain wall motion during TB propagation through the sample under applied magnetic field. Both observations are in a good agreement with the high uniaxial anisotropy observed in 5M Ni-Mn-Ga martensite.

1.2 Twin boundary motion in 5M Ni-Mn-Ga martensite

1.2.1 Mechanically induced twin boundary motion

Mechanically induced TB motion is first of all characterized by *twinning stress* (TS), which is a key property describing the TB mobility in MSM alloys. TS determines the threshold level of an applied uniaxial mechanical stress required for twin variant reorientation *via* TB motion. Therefore, TS characterizes the mobility of an existing TB and should be distinguished from the stress required for *nucleation* of another variant and formation of a new TB, which is usually few times higher (Aaltio *et al.*, 2010). Generally, TS is defined experimentally from uniaxial normal stress *versus* strain measurements for samples which are cut nearly along $\{100\}$ planes of the parent austenite, and very rarely in the shear mode. TS in single crystals is known to depend on defects, the arrangement of TBs, the twin hierarchy, and training (the correspondent references can be found in Straka *et al.* (2011)).

It was found that in 5M Ni-Mn-Ga martensite, type 1 and type 2 TBs demonstrate substantially different TS measured at room temperature: typically ~ 1 MPa for type 1, and ~ 0.05 - 0.3 MPa for highly mobile type 2 (Sozinov *et al.*, 2011; Straka *et al.*, 2011). The temperature behaviour of TS is also quite different: type 2 TBs can move in a wide range of temperatures exhibiting low TS values, even down to 1.7 K, whereas the TS for type 1 TBs has a strong thermal dependence (Straka *et al.*, 2012; Heczko *et al.*, 2013a). Heczko *et al.* (2013b) note that this behaviour suggests that the mobility of the TB depends mainly on the internal structure of the boundary itself.

Despite the exciting properties of type 2 TB, the mechanism behind the ultra-high mobility of type 2 interfaces down to cryogenic temperatures is not yet understood. Qualitative explanations can be found in studies by Heczko *et al.* (2013b) and Seiner *et al.* (2014). As discussed by Heczko *et al.* (2013b), type 1 interface at the meso-scale runs along (101) crystallographic plane of the lattice, while type 2 twinning plane is irrational and thus its high mobility or very low TS can be explained by considering the difference in potential energy landscape on an atomic scale. Seiner *et al.* (2014) discuss multi-scale picture of the TB motion. Three distinct spatial scales are considered: meso-scale (modulation twinning), micro-scale (compound *a-b* lamination), and nano-scale (nanotwinning in the concept of adaptive martensite). According to this study, two mobile interfaces – type 1 and type 2 macro-twins, have different micromorphologies at all considered spatial scales, which can qualitatively explain their different TS values observed in the experiments: while for the type 2 there are no reasons for microstructural

pinning at any of the considered scales, the motion of the type 1 can be hindered by such pinning at all scales.

The electron backscatter diffraction (EBSD) analysis by Chulist *et al.* (2013) also revealed that there can exist interfaces composed of segments of type 1 and type 2 twins. The TS for such an interface is between the TS for type 1 and type 2.

Usually, the TS is determined in quasi-static conditions using conventional stress-strain apparatus, thus describing TB properties in a limited range of TB velocities, typically well below 0.1 m/s. Currently, there is almost no experimental data in the literature on the TS dependence on TB velocity. Only recently Zreihan *et al.* (2018) reported on TS dependence on the load rate for type 2 TB. In their work, the average TS changed from 0.09 to 0.15 MPa while the load rate changed from 5×10^{-6} to 2×10^{-3} m/s that corresponds to the TB velocity ranged from 8×10^{-5} to 3×10^{-2} m/s (recalculated for a single moving TB). However, all the presented stress-strain curves demonstrate an unusually noisy behaviour with abrupt changes of the stress which are much larger as compared to the average TS values taken from the “best”, initial parts of the curves. In connection to this, the authors note that based on the videos the abrupt large stress peaks relate to instances at which the moving TB stopped and another type 2 TB started to move. Thus, the presented data reflect behaviour of a sample whose quality is worse as compared to other studies where a single type 2 TB propagated through the whole crystal (see, *e.g.*, stress-strain measurements presented by Sozinov *et al.* (2011) and Straka *et al.* (2011)).

1.2.2 Magnetically induced twin boundary motion

In 5M Ni–Mn–Ga martensite, a giant 6% magnetic field-induced strain (MFIS) can occur under application of a magnetic field. In the literature, different modelling approaches describing MIR in Ni-Mn-Ga alloys can be found, based on: micromagnetics (James *et al.*, 1999; Paul *et al.*, 2007), general thermodynamics (O’Handley, 1998; Likhachev and Ullakko, 2000; Henry *et al.*, 2001), statistical approaches (Glavatska *et al.*, 2003), the motion of twinning dislocations (Müllner *et al.*, 2003), and magnetoelastic interactions (Chernenko and L’vov, 2008). In these models, the authors derived analytical expressions describing the equilibrium strain and magnetization as a function of the applied magnetic field and, in some models, of the external mechanical stress. This corresponds to the presented experimental results that generally include quasi-static uniaxial stress-strain measurements with magnetic field applied perpendicularly to the stress direction. Some of the models give so similar outputs that it becomes difficult to conceive an experiment that would distinguish the right one (see, *e.g.*, Heczko (2010)).

Without going into detailed discussions, we note that the variety of the suggested and somewhat contradictory models is partially related to the early experimental data obtained on low-quality Ni-Mn-Ga crystals and, secondly, to inadequate control of the twin variant structure until its importance became clear. The quality of the samples often did not allow full twin variant reorientation (correspondent to the maximum transformation strain, ε_0) because of defects and impurities, and residual twins could not be eliminated.

Uncontrolled twin variant arrangement led to high twinning stresses or prevented TB propagation. A substantial work has been done on the development of the high-quality Ni-Mn-Ga crystals (*e.g.*, by AdaptaMat Ltd., Finland), which greatly helped the researches and brought better insight into the phenomenon of MIR.

In our further review we will concentrate on the widely used approach in which MIR is described based on the magnetocrystalline anisotropy and Zeeman energy interplay. These ideas were developed and supported experimentally in many studies mentioned below and match well the experimental results obtained in this Thesis.

The magnetocrystalline anisotropy energy was mentioned to be responsible for the observed 0.2% MFIS in Ni₂MnGa crystal in the pioneer work by Ullakko *et al.* (1996). Another contributor to the free energy is Zeeman energy (O’Handley, 1998; Likhachev and Ullakko, 1999; O’Handley *et al.*, 2000). The equilibrium orientation of the magnetization inside a specified single-variant volume of the sample will result from interplay between the Zeeman energy and anisotropy energy. An expression describing the equilibrium energy difference per unit volume, ΔG , between two differently oriented variants in magnetic field (if the field is aligned along the easy c -axis in one of the variants) can be written in the following form (see, *e.g.*, Marioni *et al.* (2003b)):

$$\Delta G = U_{\parallel} - U_{\perp} = \begin{cases} -K_u(2\eta - \eta^2) & \text{if } \eta \leq 1 \\ -K_u & \text{if } \eta > 1 \end{cases} \quad (1.1)$$

where U_{\parallel} and U_{\perp} mean free energies of two variants where magnetic field is applied in parallel and perpendicularly to the easy axis, respectively. The dimensionless parameter $\eta = \mu_0 M_S H / 2K_u$ is defined for a convenience, μ_0 is vacuum permeability, M_S is the saturation magnetization, H is the applied magnetic field, and K_u stands for the uniaxial magnetic anisotropy constant, which is a measure of the work required to turn the magnetization away from the easy c -axis by 90 degrees. Although Equation 1.1 is obtained for equilibrium conditions, it can also be used in a dynamic case of TB motion, because TB velocities are much slower compared to the magnetization rotation response inside the crystal unit cells. Experimentally the energy difference ΔG can be found from magnetization curves measured for a single variant sample with magnetic field parallel and perpendicular to the easy axis (Likhachev and Ullakko, 2000). According to Likhachev *et al.* (2006), the experimentally measured single-variant partial magnetization free energies already consist of the important contributions like the magnetic anisotropy, Zeeman and magnetostatic energies.

We note that Equation 1.1 gives an averaged value of the free energy difference, since in reality the magnetization is not uniform, especially at small magnetic fields (*i.e.*, at small values of η) and in the variant where the external field is applied along the hard axis. One can expect that with increase of the external field, the magnetization distribution becomes more uniform.

From Equation 1.1, it follows that at a certain field value, $H_S = 2K_u/\mu_0 M_S$, a saturation of the magnetic driving force, ΔG , occurs. Physically saturation means that all the individual magnetic moments in both variants are aligned with the magnetic field and correspondent magnetic field-induced stress for TB motion approaches its maximum value. Importantly, an increase of the external magnetic field beyond the value H_S does not provide any further increase of the magnetic driving force for the TB motion. Thus, at fields $H \geq H_S$, $\Delta G = K_u$. If we neglect the demagnetizing factor, H_S coincides with the anisotropy field of the alloy, H_a .

Based on the energy ΔG , a correspondent magnetic field-induced stress (or “magnetic pressure” acting on the TB) can be obtained. Indeed, one can expect that the same macroscopic deformation can be achieved either by applying a magnetic or mechanical force, independently on the physical nature of the force. Using general thermodynamic approach, Likhachev and Ullakko (2000) derived an expression for the equivalent magnetic field-induced stress, σ_{mag} :

$$\sigma_{mag} = \Delta G/\varepsilon_0. \quad (1.2)$$

From Equations 1.1 and 1.2, it follows that at fields beyond the saturation field, H_s , the magnetic field-induced stress reaches its maximum value: $\sigma_{mag} = K_u/\varepsilon_0$.

In order to actuate TB motion by a magnetic field, the magnetic field-induced stress must exceed the twinning stress. At room temperature, in 5M Ni-Mn-Ga martensite, typical values for σ_{mag} in saturation field are around 3 MPa, which is enough for MIR to appear as the typical TS values lie in the range 0.1-1 MPa. The closer the TS approaches zero, the higher is the efficiency of MIR.

Analogously to the TS characterizing the threshold stress in mechanically induced TB motion, the threshold applied magnetic field for TB motion can be determined in magnetic measurements, which is called a switching field, H_{sw} . As it was early mentioned, the magnetic field and the correspondent magnetization along the TB are not uniform at small fields because of the high uniaxial magnetic anisotropy. Therefore, the experimentally measured switching field is dependent on the sample geometry and location of the TBs in the sample. For example, Heczko *et al.* (2015) reported on H_{sw} varied in the range from 8 to 32 kA/m for the same TB of type 2 located at different positions within 16 mm from the edge of the sample, while the mechanical TS was approximately constant. The maximum switching field was observed when the TB was located at the very edge of the sample. The experimental results were compared with a model taking into account magnetostatic interactions and demagnetization effects in addition to magnetocrystalline and Zeeman energies, and demonstrate that the switching field depends on the shapes and relative size of the individual twin variants separated by the type 2 interface. We note that using Equations 1.1 and 1.2 together with K_u , M_S , H_a and ε_0 values mentioned in the article, for the lowest switching field value of 8 kA/m one can derive a correspondent magnetic field-induced stress of ~ 0.1 MPa, which is in a very good agreement with the measured TS of ~ 0.11 MPa.

1.2.3 Experimental studies and modelling approaches on twin boundary dynamics

In the present section, we will concentrate on the published experimental results and modelling approaches devoted to twin boundary dynamics in 5M Ni-Mn-Ga martensite. In addition, some remarkable results related to characterization of the actuators based on this material, are discussed.

Understanding the mobility of TBs, namely, the TB velocity dependence on the magnetic field strength, the role of inertia and possible resistance forces, was readily recognized for having a great scientific and practical importance (Marioni *et al.*, 2002). After discovery of type 1 and type 2 TBs, a great interest aroused to understand the origins of the large difference in mobility of these two boundary types.

The early research on TB dynamics in Ni-Mn-Ga single crystals under a magnetic field excitation was performed using AC field-induced strain measurement under load (Henry *et al.*, 2001; Henry *et al.*, 2003). The authors used a compression spring to reset the sample when the magnetic field approached zero value, and sample's displacement was measured with a proximity sensor. Maximum actuation frequency of 500 Hz at 1.5 % strain was demonstrated for a sample measured $2 \times 6 \times 18 \text{ mm}^3$. The type and number of the TBs were not controlled in these experiments.

Marioni (2003) (see also Marioni *et al.*, 2003a and 2003b) used a compact air-core Helmholtz coil to actuate Ni-Mn-Ga samples by magnetic field pulses of various intensities lasting 620 μs and having semi-sinusoidal shape. In these experiments, one end of the crystal was fixed, and time-resolved displacement of the free end was measured with a reflected laser beam. An advantage of the used setup can be clearly seen: the driving force is purely magnetic and no load stresses are applied, with no possible inertia of any measurement device (except a light-weight mirror glued to the sample's free end). It is shown that the complete field-induced strain can be obtained in 250 μs , which implies the possibility of full 6% cycling of Ni-Mn-Ga at 2 kHz, for crystals having dimensions in the range of a few mm. The reported values for maximum actuation velocity and acceleration (numerically derived from the displacement data) achieved at saturation driving force are $\sim 6 \text{ m/s}$ and $50 \pm 10 \text{ m/s}^2$ respectively. It is worth noting that both peak velocity and peak acceleration reached their maximum values at the maximum driving force calculated according to Equation 1.1, and remained unchanged at fields beyond saturation. The extension onset time (time from the beginning of the field pulse at which the extension reached a set threshold value above the noise level) lay in the range of 40–200 μs . These delays were attributed to: (i) the time it takes for the magnetic field to reach the threshold level of actuation, and (ii) mass-inertia which depends on the position and number of mobile TBs. According to a model that takes the sample inertia into account, the maximum observed delay matches to a single TB moving from the fixed to the free end of the crystal, and the minimum delay corresponds to uniformly distributed TBs. The number and type of TBs were not controlled in these experiments. In addition, the author reports on defects such cracks and pinning sites, which caused the TBs to stop at certain

points of the crystal and remain pinned unless the field is increased. The observed scatter in the field-induced extension measurements data, points to non-repeatable TBs configuration. The threshold field $H = 4$ kOe (318 kA/m) registered at the onset time of 40 μ s during pulsed actuation, was considerably large compared to the threshold field of 1.5 kOe (120 kA/m) observed at slowly increasing field. Further experimental data clearly pointing to the pinning obstacles that affected the TB motion in the investigated crystal, can be found in Marioni *et al.* (2004).

Suorsa *et al.* (2004) reported on MSM actuator performance measurements. The actuator design included a spring load and allowed actuation at 5 kHz. For a pulsed actuation, the maximum actuation speed of 1.3 m/s and acceleration of 5000 m/s² are reported (derived from the displacement). The type and number of the TBs were not controlled.

The results presented by Korpiola *et al.* (2013) demonstrate larger maximum actuation velocities of 1.9-3.1 m/s (calculated from the time needed for 5% deformation), under pulsed magnetic field actuation with the pulse length of ~ 1 ms and rise time (to saturation field) of ~ 20 μ s. The twin variant configuration was not controlled in these experiments.

Stroboscopic imaging technique under AC excitation up to 600 Hz with a spring load, was used by Lai *et al.* (2008) to investigate the motion of individual TBs. Based on the acquired images, the average TB velocity was calculated based on the changes in twin variant width during cycling. Unfortunately, the TB type is not known from the experiment because the images were taken from the side view with polarized light contrast, where the two types are indistinguishable. The maximum (average) observed TB velocity was 0.21 m/s. The velocity is shown to be inversely proportional to the density of TBs. The data implies that TB velocity is not the limiting factor of the actuation performance. Moreover, the maximum strain (measured locally) was found to increase with the actuation frequency. The authors believe that the fast motion of the TBs in high-frequency actuation may increase the TB mobility. Presumably, with increasing the frequency, the TBs are driven faster because they can overcome more defects and travel further under the same driving force. The findings also indicate that the motion of TBs is the main source of the observed energy losses (fast heating of the sample occurred during actuation – see Lai (2009), p.48), and the undissipated heat at the moving TB cannot be excluded from contributing to the found phenomena (a decrease of twinning stress is expected at elevated temperatures). On the other hand, the authors reduced the heating effect making the measurement time short, less than one second. We note, however, that the strain was measured only *locally*, for a particular twin variant band, and thus the mentioned effect could be compensated by a slower motion of some other TBs. In this respect, the reported effect could indicate just a difference in the mobility of TBs located at different places, and *redistribution of the strain* along the sample at different frequencies cannot be excluded. Indeed, Lai (2009, p.77) notes that the TB motion was not uniform and the particular twin variant under observation in each sample had the largest change in variant width within the investigated region. Another observation which somewhat contradicts the enhanced mobility at higher frequencies, is the increase of the hysteresis of the TB motion with increasing frequency (Lai *et al.*, 2008). In addition, the

TB motion was obviously lagging behind the field at 600 Hz actuation frequency. Experiments with pulsed magnetic field (see Lai (2009), p.79) aimed to support the idea of the TB mobility enhancement as they showed an increase of the twin variant width as the field rise time decreased. However, the author did not take into account that in the presented experiments the applied magnetic field profiles were different for each pulse while the twin variant width was measured after the same time from the pulse start. Thus, this result might be more naturally explained by the different effective actuation times. The effect of sample inertia which might affect the strain distribution in the sample, was not analysed in these studies.

A special attention should be devoted to a series of papers published by Faran and Shilo (2011, 2012, 2013, 2014, and 2015). The aim of this study was to find the relation between the velocity of an individual TB and the magnitude of the applied magnetically induced driving force. This relation is referred to as the "*kinetic relation*" and describes the velocity of a propagating interface as a function of the thermodynamic driving force that acts on it (see, *e.g.*, Abeyaratne and Vedantam, 2003, and references found in papers by Faran and Shilo).

Faran and Shilo used an original experimental approach to study individual TBs motion under pulsed magnetic field actuation in 5M Ni_{50.0}Mn_{28.3}Ga_{21.7}. In these studies, one band of the second variant (and, consequently, two TBs) was introduced into a single variant sample and photo images were taken before and after the field pulse. Average velocity evaluation of the TBs of both types was performed based on the measurements of the distance that individual interfaces passed due to the application of a magnetic field pulse of a known length (more exactly, from the estimated TB velocity along [100] direction, the authors calculated sideways TB velocity which is directed perpendicularly to the TB plane). Importantly, the authors evaluated the effect of inertia as negligible for the used crystal size of 3.0×2.4×0.9 mm³ (Faran and Shilo, 2011) and assumed that the average velocity is approximately equal to the instantaneous velocity. The sample was placed inside a Helmholtz coil using an insulating, non-constraining adapter. The coil was powered with a custom-made power supply that provided near-square current pulses lasting 10–120 μs, with rise and fall times shorter than 15% of the pulse duration. By changing the pulse amplitude, it was possible to control the magnetic driving force, g , which is the thermodynamic driving force for twin wall motion (energy per unit volume). In addition to the Zeeman and anisotropy energies (see Equation 1.1), the authors included an additional term describing "demagnetization energy", whose sign and value relate to the magnetic field direction and the size of the band variant inside the sample. The calculated velocities of type 1 and type 2 TBs are of the order of 1–2 m/s in fields below 0.3 T. At fields above 0.75 T (providing saturated driving force), TB velocity saturated at a value of ~2 m/s (Faran and Shilo, 2014). No signs of pinning were observed. However, a very large scattering of the velocity values can be seen for a given driving force. The authors assume that while twin walls are not pinned, there is probably some local interaction with defects, which results in a large velocity variation: local mobility increased by nearly an order of magnitude whereas the TB position was shifted by only 30 μm (Faran and Shilo, 2013). Based on these observations, the authors concluded that

for a large number of data points, the maximal velocity for each driving force is close to the velocity in a defect-free crystal.

The main conclusion from the studies by Faran and Shilo is that the dynamics of the TBs exhibits some kind of bimodal behaviour with a threshold driving force g_0 – see Figure 1.4. The threshold driving force values are different for two TB types: for type 1, $g_0 = 106.2 \text{ kJ/m}^3$, and for type 2, $g_0 = 84.2 \text{ kJ/m}^3$ (Faran and Shilo, 2013). At low driving force, $g < g_0$, velocity changes moderately with the driving force. Above g_0 , the behaviour changes abruptly and TB velocity increases much faster with the driving force. Importantly, for both type 1 and 2 TBs, the transition driving force g_0 is much larger than the critical driving force associated with the twinning stress. Based on these observations, the authors conclude that TB follows two distinct kinetic relations, at different ranges of the driving force g . According to the developed microscopic model, in the range $g < g_0$ the TB motion is governed by a thermally activated process in which 2D steps are nucleated on the twin plane and then grow by a motion of the step edges. The corresponding kinetic law is described by an exponential function. Above g_0 , this mechanism is overridden by athermal and fast motion of twinning dislocations that is represented by the following equation for the local TB velocity, \bar{v}_{TB} :

$$\bar{v}_{TB} = \mu \sqrt{g^2 - g_0^2}, \quad (1.3)$$

where μ is a mobility coefficient describing a viscous motion. The threshold driving force, g_0 , is associated with the Peierls barrier: $g_0 = \gamma_0 \pi / d$. Here, γ_0 is the amplitude of the barrier (energy per unit area), and d is the lattice periodicity along the [011] direction.

Another important contribution to characterizing and modelling the TB motion is presented in the study by Smith *et al.* (2014). In this paper, a novel experimental method was developed that aimed to observe the velocity of a single TB under magnetic field pulse actuation. A fully elongated, single-variant sample was placed near a solenoid used as a magnetic field source, with one end located at the opening of the solenoid, and the other end fixed to a holder. By application of a magnetic field pulse of $\sim 30 \mu\text{s}$ length and $\sim 3 \text{ MA/m}$ peak field, the free end of the sample was transformed to another variant with the easy c -axis aligned with the solenoid axis. Due to the kinking, the total reflected light from the sample surface changed during the actuation, and was measured by a photosensor having a short response time of $\sim 0.3 \mu\text{s}$. The measured signal was recalculated to the position of the TB, under an assumption that a single TB was nucleated and moved during the experiment – see Figure 1.5. Afterwards, the position signal was fitted with a hyperbolic function, from which velocity and acceleration were derived. The calculated curves demonstrate maximum TB velocity and acceleration of 82.5 m/s and $2.9 \times 10^7 \text{ m/s}^2$, respectively, and maximum sample contraction velocity and acceleration of 4.6 m/s and $1.6 \times 10^6 \text{ m/s}^2$. A theoretical model was developed which is based on variable-mass equation for the growing variant. The force is equal to the difference between magnetic field-induced stress and constant twinning stress, both multiplied by the sample's cross-section. The modelled results are in a good agreement with the data

calculated from the experiment. Although the results look very attractive, there are few points that should be noted: (i) incorrect direction of the velocity of the moving variant and the applied force (along the sample instead of the shear direction) assumed in the model, leads to overestimation of the theoretical TB velocity (by ~ 1.5 times) and acceleration. (ii) The measured optical signal is proportional to the volume fraction of the growing variant, not directly to the TB position. For example, multiple parallel bands of the second variant could appear and grow during the pulse resulting in the same signal and final twin variant configuration. (iii) The possibility to nucleate a TB by a magnetic field pulse is doubtful and it is not supported by any experiments (the authors note that nucleation requires at least 5 times more energy compared to the motion of an existing TB). Alternatively, some residual TBs could present in the sample initially, which could not be resolved with the used microscopic inspection method. (iv) There is no data concerning the chemical composition and transformation temperatures of the alloy, TB type, nor magnetization characteristics such as saturation magnetization and anisotropy field measurements.

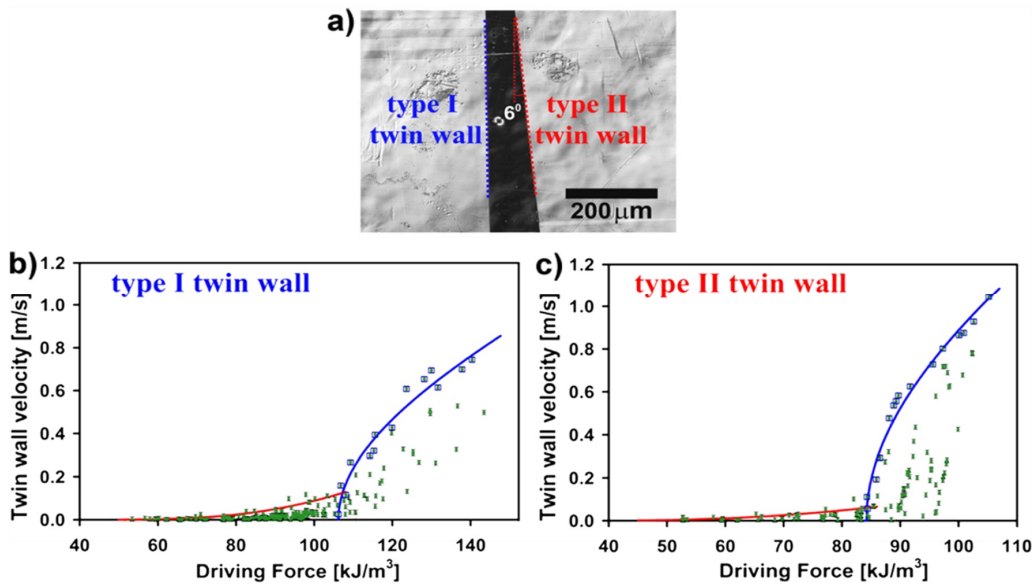


Figure 1.4: Twin wall velocity *versus* the driving force, g , for type I and type II twin walls in a NiMnGa crystal (Faran and Shilo, 2013): (a) microscope image showing the two walls and their relative projection with respect to the $(1\ 0\ 0)$ faces of the crystal. In (b) and (c), the experimental data obtained from both walls reveals two different kinetic behaviours at different ranges of the driving force. At the higher driving force range, $g > g_0$, the square root kinetic relation (Equation 1.3) is fitted to the maximal velocity values, yielding the solid blue lines. At the lower driving force range, $g < g_0$, the exponential type relation is fitted to the maximal points, yielding the solid red lines. © Elsevier Ltd. Reproduced with permission. All rights reserved.

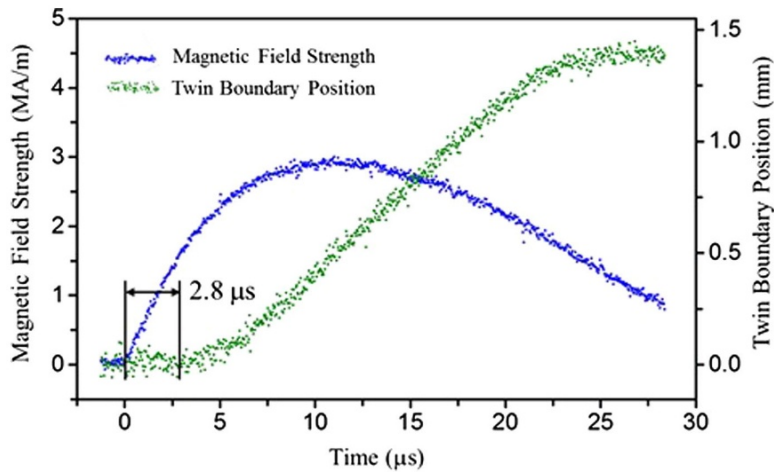


Figure 1.5: A graph showing the magnetic field and TB position as functions of time obtained from a typical experiment by Smith *et al.* (2014). The blue curve is the magnetic field, calculated from the current through the solenoid, and the green curve is the TB position recalculated from the photosensor signal. A delay of $2.8 \mu\text{s}$ can be seen between the onsets of the two curves, which is attributed to the time for a TB to nucleate within this time frame. © Elsevier Ltd. Reproduced with permission. All rights reserved.

1.3 Concluding remarks

From the presented literature review, the following conclusions can be made regarding 5M Ni-Mn-Ga martensite structure and twin boundary mobility.

1.3.1 Crystal structure and twinning

The crystal structure, to a first approximation, can be considered tetragonal with $a \approx b$ and $c/a < 1$. The crystal lattice reorientation is possible *via* twin boundary motion which naturally occurs in a shear mode.

Two crystallographically different TB types, type 1 and type 2, were found that can be identified visually by the difference in their projections on the sample's faces. These types exhibit substantially different mobility properties that is most likely connected to the different internal structure at the atomic level. The differences are reflected in mechanical (twinning stress behaviour), magnetic (switching field and TB velocity) and temperature-dependent measurements.

Complex twin microstructures were observed at the mobile interfaces at different spatial scales related to modulation twinning, a - b lamination and nanotwinning, which can qualitatively explain the different behaviour of the two TB types observed in the

experiments. In contrast to that, the magnetic domain structure remains simple and similar for both TB types, thanks to the high uniaxial anisotropy.

Twinning stress is a key parameter characterizing TB mobility under a mechanical stress which is generally measured with a conventional stress-strain apparatus thus describing the TB motion at velocities well below 0.1 m/s. A similar property in magnetically induced motion is the switching field.

Few models were suggested to explain magnetically driven TB motion and some of them are still under discussion. The idea originally proposed by Ullakko *et al.* (1996), which is based on the magnetocrystalline anisotropy energy difference between the twin variants in a magnetic field, was developed further and seems to be accepted in the majority of the studies.

1.3.2 Twin boundary dynamics

Two experimental approaches used in the TB dynamics studies are presented in the literature: (i) AC magnetic field-induced TB motion under a spring load (where the magnetic field is applied in the perpendicular direction to the mechanical load), and (ii) pulsed magnetic field actuation of MSM samples.

The first approach provides cyclic actuation of MSM samples and is useful for actuating devices characterization (such as frequency response). In this complex configuration of two simultaneously acting forces of different nature, it is practically difficult or even impossible to estimate the stress (or driving force) acting on an individual TB. In addition, the TB arrangement and type were not controlled in these studies. Practically, the only reliable result is the observation of the average TB velocity up to 0.21 m/s for an individual TB with the use of a stroboscopic technique by Lai *et al.* (2008).

The second approach, based on the pulsed magnetic field actuation, obviously provides better possibilities to control the driving force by the change of the field strength. However, in the studies by Marioni *et al.*, Suorsa *et al.*, and Korpiola *et al.*, only actuation velocities were estimated from the displacement of the whole sample having uncontrolled TB configuration, *i.e.*, with multiple TBs propagation. Importantly, these works indicate the possibility of a rapid actuation of an MSM sample within sub-millisecond time-scale, with actuation velocities reaching 6 m/s (Marioni, 2003). This implies that the maximum velocity of individual TBs should represent a noticeable part of this value (taking into account the maximum transformation strain of ~ 0.06).

Only in the studies by Faran and Shilo (2011-2015), and by Smith *et al.* (2014), the authors aimed to follow the motion of individual TBs under controlled and/or saturated magnetic driving force. The main contradictory conclusion coming from the experiments of these two groups, is more than an order difference in the maximum TB velocity: ~ 2 m/s *versus* ~ 80 m/s. In addition, there are many controversial questions concerning the experimental procedures and modelling, as it was discussed in Section 1.2.3. One of the

important questions is the role of the mass inertia in the TB motion which was interpreted oppositely in these works.

It is worth noting that all the above studies utilized different measurement techniques based on the displacement measurements (or on the signal proportional to the twin variant fraction in the case of Smith *et al.* which can be recalculated to the sample's contraction displacement) that allowed only an estimation of the averaged velocities. No instant TB velocity or TB position measurement was done.

Finally, it can be seen from the literature that crystal quality plays an important role in the MSM effect investigations. Both the crystal structure (internal defects) and surface defects can affect the TB mobility. In worse cases, defects can lead to pinning obstacles and formation of residual twin variants which restrict TB motion. Therefore, a thorough selection and preparation of the samples is required.

1.4 Motivation for this study

The overall motivation for this study is the necessity of a deeper characterization and understanding of the twin boundary dynamics in 5M Ni-Mn-Ga martensite at the level of individual interfaces. In practice, this would enable the development of applications that could take full advantage of the material's properties. In the literature, however, there are only a few studies directly related to this research problem. Moreover, the existing results are controversial and reveal many issues and problems in both the experimental approaches and theoretical modelling.

In particular, the current study was motivated by the previous research done by Smith *et al.* (2014) at Material Physics Laboratory in Savonlinna, Finland, with a goal to more deeply characterize and understand the phenomenon of fast TB motion by means of more advantage experimental approach based on laser Doppler vibrometry technique.

Next, it was important to compare the new results with the experimental studies and the so-called "kinetic relation" approach presented by Faran and Shilo (2011, 2012, 2013, 2014, and 2015). First, as it was already discussed, their estimated maximum TB velocities differ from the research by Smith *et al.* (2014) by an order of magnitude. The second important question is the role of inertia in the pulsed magnetic field experiments, which was treated in completely different ways. Next, the bimodal behaviour with a threshold driving force g_0 needs to be validated by an independent research.

Finally, other possible forces, such as magneto-static forces and torques, which might affect the TB motion but remained out of scope in the previous research on TB dynamics, should be addressed and experimentally investigated.

2 Objectives of the research

The goal of this Thesis is to provide more insight in the twin boundary dynamics in 5M Ni-Mn-Ga martensite, namely, to precisely characterize transient twin boundary motion under pulsed magnetic field actuation and evaluate the effects of mass inertia and resistance forces of different nature in twin boundary dynamics.

Summarizing the studies found in the literature, the research objectives of the present work were formulated as follows:

- Development of a new experimental setup utilizing the laser Doppler vibrometry technique, which permits direct non-contact time-resolved measurement of the sample actuation velocity, with a pulsed magnetic field generation apparatus to be used as the actuation method with a variable driving force.
- Modifying the above experimental setup to enable the direct observation of twin boundary motion with the use of the high-speed camera technique. Comparison with the results obtained with the laser Doppler vibrometry setup.
- Detailed experimental characterization of single twin boundary motion including time-resolved velocity and displacement measurements, for both type 1 and type 2 boundaries, at saturated magnetic driving force. Finding limitations for twin boundary velocity. Characterization of the sample actuation response, in terms of actuation velocity and acceleration measurements, and response times.
- Development of a macroscopic model for single twin boundary motion induced by a pulsed magnetic field. Analysing the possible actuation modes, effects of the sample's geometry (shape and size) and revealing the main motion parameters. Providing rationale for the experimental setup development.
- Application of the developed model for extraction of the motion parameters from the experimental data and for simulation of the experimental results. Revealing and analysing the effects of mass inertia, internal friction, and field-dependent forces such as magneto-static forces, torques and eddy currents, in twin boundary motion.
- Experimental characterization of single twin boundary motion, for type 1 and 2 interfaces, at different magnetic fields below saturation. Finding threshold (switching) fields for TB motion. Analysing the results and comparison with the so-called kinetic relation approach.
- Experimental characterization of multiple twin boundary motion in saturation field and comparison with the results obtained for single twin boundary motion.
- Application of the developed experimental setup and model to measure and analyse pulsed magnetic field-induced actuation of micropillars having cross-sections of the order of $50 \times 50 \mu\text{m}^2$, prepared with focused ion beam (FIB) milling

technique. Revealing the possible scaling effects, *i.e.*, change in the dynamic behaviour with the sample size.

- Comparison of the results obtained in this Thesis with the results by Smith *et al.* (2014), and the kinetic relation approach developed by Faran and Shilo (2011, 2012, 2013, 2014, and 2015).

3 Macroscopic model for twin boundary motion

In this chapter we present an original approach for modelling the twin boundary motion developed by the Author of this Thesis. We will first introduce a macroscopic mathematical model for the case of a single twin boundary motion induced by a magnetic field pulse, corresponding to contraction of the crystal and increasing mass of the moving variant. Then, other possible actuation modes, sample's geometry effects, scaling and multiple twin boundaries motion will be briefly discussed. These theoretical considerations provide the required bases for both the experimental setup development and analysis of the results.

3.1 Geometrical considerations

Figure 3.1 shows a schematic side view of the crystal cut along $\{100\}$ planes of the parent austenite, explaining the twin variants arrangement before the actuation pulse, and crystal shape change during the TB motion. In the initial state (see Figure 3.1(a)), the crystal consists of two differently oriented variants, with a single TB in between. As a first approximation, we consider the unit cell of Ni-Mn-Ga 5M martensite as a tetragonal with $a \approx b$ and $c/a \approx 0.94$. From the ratio c/a , one can directly derive the transformation strain, $\varepsilon_0 = 1 - c/a \approx 0.06$, which gives an upper limit for the maximum strain available for the crystal during full conversion from one variant to another. When we introduce a TB inside the crystal, the crystal faces are tilted at the points where TB is crossing the crystallographic $\{100\}$ planes. Two specific angles, α and β , one can calculate using following equations: $\alpha = \text{atan}(c/a) \approx 43.23^\circ$ and $\beta = \frac{\pi}{2} - 2\alpha \approx 3.54^\circ$. Different TB types visually differ in the projections on $\{100\}$ plane (here applicable for the top side of the sample): type 1 boundary exhibits nearly parallel projection relative to the crystal's edges while that of type 2 is inclined by about 6° (Sozinov *et al.*, 2011). The projections on the side view for both types are the same.

When the sample is subjected to a magnetic field pulse, the TB will move in the direction, which leads to the free energy minimization. The driving force for the motion arises from the energy difference of the twin variants with different orientations of the easy c -axis in respect to the magnetic field direction. Thus, TB will move to the right in a case of applying a sufficiently strong magnetic field along the sample's largest dimension. Two steps of this motion are depicted in Figure 3.1(b), showing correspondent TB position change from L_0 to L_1 (note that the sample's right end is fixed to a holder so that only the left variant is allowed to move). Here the left variant is growing at the expense of the right one having its easy axis perpendicular to the external field direction. Note that the crystal structure limits the motion allowing only shear mode of deformation. Therefore, any point and the whole mass of the crystal behind the TB move in the direction, which is parallel to the TB plane – see the vector \vec{v} in Figure 3.1(b). As a result, the sample will contract with time at a velocity v_C . The TB velocity, v_{TB} , defined here as the velocity of the boundary along $[100]$ direction in the right, non-moving part, is directly proportional to the contraction velocity: $v_{TB} = v_C / (\cos \beta - c/a) \approx v_C / \varepsilon_0$. From the crystal geometry,

it follows that the absolute values v and v_{TB} are in a direct proportion: $v_{TB} = k_0 v$, where $k_0 = \cos \alpha + \sin \alpha / \tan \beta \approx 11.8$.

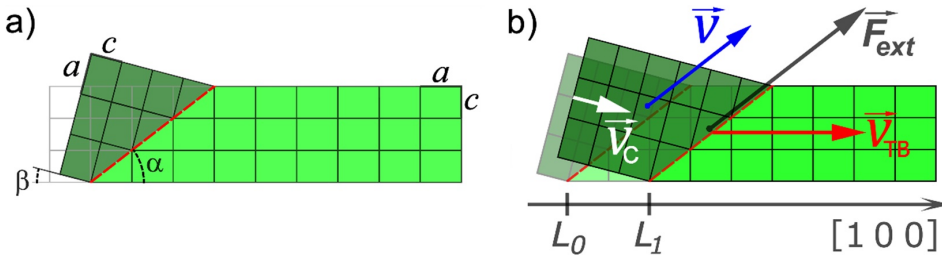


Figure 3.1: Schematic side view of the Ni-Mn-Ga sample. (a) Initial twin variant arrangement. The red dashed line denotes the TB. The ratio a/c is enlarged for clarity. (b) Two subsequent configurations of the sample during the TB motion, with correspondent TB position change from L_0 to L_1 , when a magnetic field is applied along $[100]$ direction. The sample's right end is glued to a sample holder (not shown). Description for the velocity and force vectors (not to scale) is presented in the text. [Publication III]

3.2 Variable-mass system equation

During the pulsed magnetic field actuation, three different regions – acceleration, saturation and deceleration, can be observed. We imply here that the right part of the sample is fixed to a rigid holder and cannot move that corresponds to the real experimental conditions in the present study.

Acceleration At the beginning of the pulse, when the magnetic field-induced stress is enough to overcome the twinning stress, the TB starts to move. The motion of the TB means that the whole part of the crystal behind the TB also moves in the direction parallel to the TB plane. As the TB is propagating further, new parts of the crystal are involved into the motion being accelerated along the same direction. Thus, the mass of the variant behind the TB is continuously growing and accelerating.

Saturation At a limited value of the driving force and enough long pulse, a saturation of the TB velocity will occur. The saturation means that the velocity of the moving variant reaches such a value, at which the driving stress (meaning the magnetic field-induced stress minus all possible resistant stresses) is able only to accelerate a new portion of the sample up to the same velocity at every instant of time. In other words, the whole momentum of the moving mass increases only due to the increase of the mass.

Deceleration At the descending part of the magnetic field pulse, the magnetic field-induced stress drops down. The mass involved in motion decelerates, but still grows until the TB stops. Because of the inertia, the TB will continue its motion after the end of the pulse. The traveling distance before it stops is dependent on the resistance stress value.

An important conclusion coming from the above description is that inertia plays a significant role at any stage of the TB motion. The moving mass behind the TB changes all the time during the motion, so we have an example of a variable-mass system. Hence, we can write for that system Newton's second law in the form of the momentum change (Sommerfeld, 1959): $d\vec{p}/dt = \vec{F}_{ext}$, where $\vec{p} = m\vec{v}$ is the momentum of the mass m (the mass of the growing variant) moving at the velocity \vec{v} , t is time, and \vec{F}_{ext} is the vector sum of all external forces applied to the mass m in the direction of \vec{p} (see Figure 3.1(b)). The mass m can be expressed as a function of the TB position L : $m(L) = m_0 + \rho A_0(L - L_0)$, where m_0 is the initial mass of the moving variant, ρ – volumetric mass density of the alloy, $\sim 8000 \text{ kg/m}^3$, A_0 – cross-sectional area of the sample on the right side of the TB, and L_0 – initial position of the TB. Now we can rewrite Newton's second law in the following form:

$$\rho A_0 \frac{dL}{dt} \vec{v} + (m_0 + \rho A_0(L - L_0)) \frac{d\vec{v}}{dt} = \vec{F}_{ext}. \quad (3.1)$$

In order to convert Equation 3.1 into a scalar form, we can take into account the proportionality between v_{TB} and v , and the relationship $v_{TB} = dL/dt$. Defining the positive direction as the direction of the vector \vec{v} , we get a scalar differential equation for the function $L(t)$:

$$\frac{\rho A_0}{k_0} \left(\frac{dL}{dt} \right)^2 + \frac{m_0 + \rho A_0(L - L_0)}{k_0} \frac{d^2L}{dt^2} = F_{ext}. \quad (3.2)$$

The value F_{ext} in the right part of Equation 3.2 is the absolute value of the vector \vec{F}_{ext} , and is positive if the vectors \vec{F}_{ext} and \vec{v} are co-directional. More definitely, the force F_{ext} can be represented by a difference between the magnetic driving force, F_{mag} , which promotes the TB motion, and a sum of resistance forces of different nature, F_{res} : $F_{ext} = F_{mag} - F_{res}$. These forces are naturally shear forces, and may have a distribution along the TB plane. For a convenience of the further discussion, we change these forces to equivalent normal stresses (or pressures) acting on the TB in the direction [100]. Thus, the equivalent magnetic field-induced stress, σ_{mag} , will relate to the force F_{mag} as $\sigma_{mag} = F_{mag}/(A_0 \cos \alpha)$, and for the resistance stress we can write: $\sigma_{res} = F_{res}/(A_0 \cos \alpha)$. Substituting in Equation 3.2 forces by the normal stresses and multiplying both sides by $k_0/(\rho A_0)$, we finally get:

$$\left(\frac{dL}{dt} \right)^2 + \left[\frac{m_0}{\rho A_0} + (L - L_0) \right] \frac{d^2L}{dt^2} = \frac{k_0}{\rho} \cos \alpha [\sigma_{mag} - \sigma_{res}]. \quad (3.3)$$

From Equation 3.3, it follows that at a constant total driving stress, $\sigma_{mag} - \sigma_{res}$, the TB velocity will saturate at a maximum value defined by the following equation:

$$v_{TB}^{max} = \left(\frac{dL}{dt} \right)_{max} = \sqrt{\frac{k_0}{\rho} \cos \alpha [\sigma_{mag} - \sigma_{res}]}. \quad (3.4)$$

In the most general case, the stresses included in the right part in Equations 3.3 and 3.4, are both dependent on the applied magnetic field strength and field distribution along the TB plane located at position L . Another parameter which is expected to affect the TB motion, is the TB velocity that could contribute in σ_{res} . Therefore, the stresses can be represented as $\sigma_{mag} = f_1(H(t), L(t))$ and $\sigma_{res} = f_2(H(t), L(t), \frac{dL}{dt}(t))$, where $H(t)$ is the applied magnetic field pulse.

3.3 Different actuation modes for single twin boundary motion

For a single TB motion, four actuation modes are possible which are schematically shown in Figure 3.2: two contraction modes (a, c) with the magnetic field aligned along the sample, and two elongation modes (b, d) with the field applied perpendicularly to the sample. The correspondent TB velocities and forces acting on the moving variant are also shown. Importantly, for the modes named “*Contraction I*” and “*Elongation I*”, the mass of the moving variant is continuously increasing, leading to similar dynamics equations (see Equation 3.3 obtained for the case “*Contraction I*”). The only minor correction for the case “*Elongation I*” is caused by a slightly different geometry which leads to small differences in values of the angle and the parameters A_0 and k_0 .

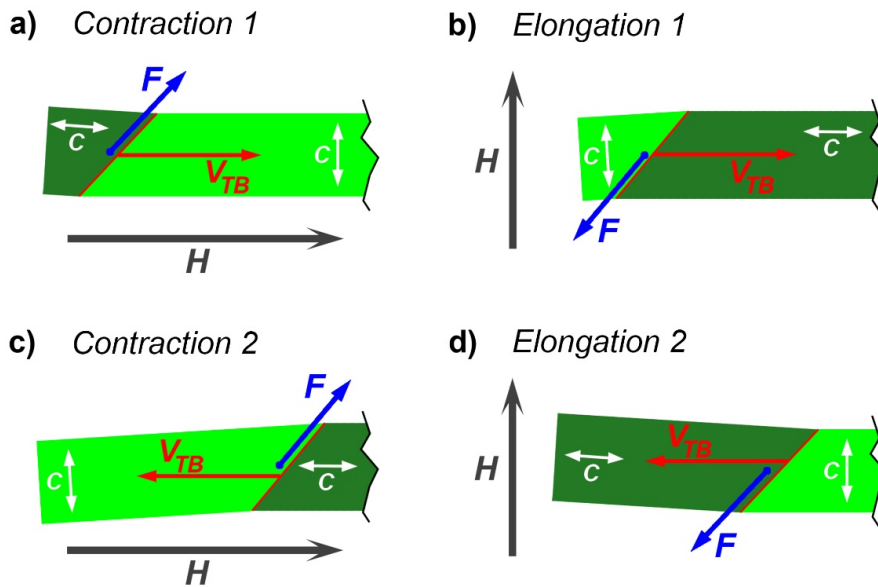


Figure 3.2: (a-d) Different actuation modes for single twin boundary motion. The sample’s right end is rigidly connected to a sample holder (not shown) while the left variant is allowed to move. White arrows show the c -axis orientation inside the twin variants. Vectors H , V_{TB} and F denote the magnetic field direction, twin boundary velocity and the force acting on the moving variant, respectively.

Two other modes named “*Contraction 2*” and “*Elongation 2*” (see Figure 3.2(c) and (d)), correspond to a case in which the mass of the moving variant is continuously decreasing. For these modes, a different equation is valid. Below we provide a differential equation derived for the mode “*Contraction 2*”:

$$\left(\frac{dL}{dt}\right)^2 + \left[\frac{m_0}{\rho A'_0} + (L - L_0)\right] \frac{d^2L}{dt^2} = -\frac{k'_0}{\rho} \cos(\alpha + \beta) [\sigma_{mag} - \sigma_{res}], \quad (3.5)$$

where A'_0 is the cross-section of the right part of the sample, $k'_0 = \frac{c}{a} k_0$, and the TB position L is measured along the right variant with positive change towards right.

The main difference between the last equation and Equation 3.3 lies in the opposite sign of the right part. According to our preliminary study, in some cases this equation does not provide a stable solution. The TB velocity saturation can occur at some conditions but at higher velocities compared to the modes with increasing mass.

3.4 Effects of the sample's shape and size

Now we will reveal how the sample's shape can affect the dynamics of a single TB motion. Let us consider the case “*Contraction 1*” (see Figure 3.2(a)) with an arbitrary shape described by a function $A(L)$, which defines the sample's cross-section dependence on the position L . Using this function, one can describe the mass of the moving variant, m , as a function of the TB position L as follows:

$$m(L) = m_0 + \rho \int_{L_0}^L A(L) dL, \quad (3.6)$$

where m_0 is the initial mass of the moving variant and L_0 is the initial position of the TB. Repeating the same calculations like earlier (see Section 3.2), we get the following equation:

$$\left(\frac{dL}{dt}\right)^2 + \left[\frac{m_0}{\rho A(L)} + \frac{\int_{L_0}^L A(L) dL}{A(L)}\right] \frac{d^2L}{dt^2} = \frac{k_0}{\rho} \cos \alpha [\sigma_{mag} - \sigma_{res}]. \quad (3.7)$$

From this equation, it follows that after acceleration the TB velocity will saturate at the same value as in the constant cross-section case (see Equation 3.4). Thus, the cross-section change will affect only on temporal variations of the TB velocity mainly during acceleration/deceleration, and has no effect on saturation velocity value.

The next important question is scaling or size effect. First, it can be directly seen that the saturation TB velocity defined by Equation 3.4, is not depended on the sample size. But, there is another term in the left part of Equation 3.3 that is related to the size effect, which is the coefficient multiplied by the TB acceleration, $\frac{d^2L}{dt^2}$.

Let us consider two cuboid samples having different sizes: one with a cross-section of $1 \times 1 \text{ mm}^2$ and the second with 400 times smaller cross-section of $50 \times 50 \text{ }\mu\text{m}^2$. Let the initial twin variant configuration in both samples be like it is depicted in Figure 3.3(a), in which by m_0 we denote the initial mass of the left, growing variant, and by A_0 the cross-section of the right, non-moving variant. When the magnetic field is switched on, the TB accelerates and moves to the right. The initial TB acceleration, as it follows from Equation 3.3 with $L=L_0$ and $\frac{dL}{dt} = 0$, is defined as:

$$\frac{d^2L}{dt^2} = \frac{\frac{k_0}{\rho} \cos \alpha [\sigma_{mag} - \sigma_{res}]}{m_0 / \rho A_0} = \frac{\frac{k_0}{\rho} \cos \alpha [\sigma_{mag} - \sigma_{res}]}{V_0 / A_0}, \quad (3.8)$$

where V_0 is the initial volume of the moving variant. The relation V_0/A_0 can be further modified: $V_0/A_0 = h_0/2 \tan \alpha$, where h_0 stands for the height of the sample on its right side. Using the last expression, we can compare the values of the denominator in Equation 3.8 for different sample sizes: they will relate as the samples' heights. From this, it follows that the initial acceleration for the smaller sample will be 20 times higher as compared to the larger sample. This scaling effect occurs because the driving force scales proportionally to the dimension in square whereas the mass scales proportionally to the dimension in cube. Similar conclusions can be made for all the actuation modes presented in Figure 3.2.

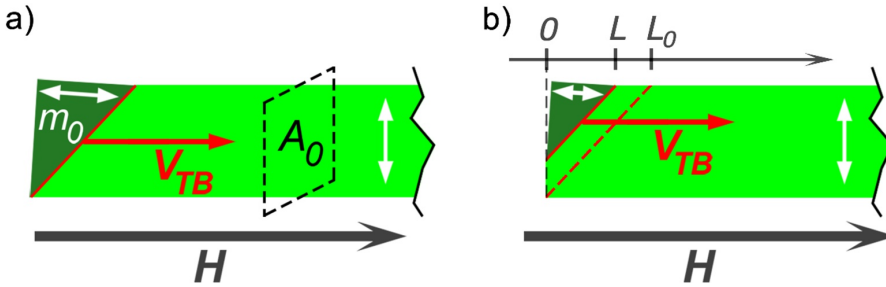


Figure 3.3: (a, b) Initial twin variant configurations in an MSM sample for description of the size effect. White arrows show the c -axis orientation inside the twin variants. m_0 denotes the initial mass of the moving variant and A_0 is the cross-section of the right variant. The vectors \mathbf{H} and \mathbf{V}_{TB} denote the applied magnetic field and TB velocity, respectively.

In addition, the model predicts a large acceleration change in a sample of any size if the initial volume of the moving twin variant approaches zero. For a triangular-shaped moving variant shown in Figure 3.3(b) corresponding to TB position change from 0 to $L_0 = h_0/\tan \alpha$, the motion law is defined by the following equation:

$$\left(\frac{dL}{dt}\right)^2 + \frac{L}{2} \frac{d^2L}{dt^2} = \frac{k_0}{\rho} \cos \alpha [\sigma_{mag} - \sigma_{res}]. \quad (3.9)$$

According to this equation, the initial acceleration can have an arbitrarily large value as the initial TB position L approaches zero, reflecting the same scaling effect, caused by different scaling of the force and the accelerated mass. Practically, this means that at a huge initial acceleration, during a short time the TB velocity will reach its saturation value defined by the total driving force, $\sigma_{mag} - \sigma_{res}$.

3.5 Magnetic field-induced stress and multiple twin boundaries motion

In Section 1.2.2, we already cited an expression for the equivalent magnetic field-induced stress (see Equation 1.2), derived by Likhachev and Ullakko (2000) using general thermodynamic approach and taking into account volume fractions of distributed variants. Importantly, this expression is valid for *any distribution* of twin variants and thus provides an estimation for a maximum stress output for an MSM sample actuated by a magnetic field. Now, it is important to derive the magnetic field-induced stress acting on a single TB and then analyse multiple TBs motion.

Let us assume that a single TB is moving by means of a compressive mechanical stress σ applied to the sample along the a -axis in the right variant (see Figure 3.1(b)), changing its position from L_0 to L_1 . The mechanical work done, W , can be calculated by multiplication the corresponding force, σA_0 , by the displacement of the sample's left edge, which is directly proportional to the TB position change: $W = \sigma A_0 (L_1 - L_0) \varepsilon_0$ (here we neglect a small correction related to the tilt angle β). On the other hand, the same position change could be produced if the boundary was moved by a magnetic field. In the latter case there is a free energy change of $\Delta G (L_1 - L_0) A_0$, where ΔG is the energy difference between two differently oriented variants per unit volume³. After equalization of the mechanical work and the free energy change, we get an expression for the equivalent magnetic field-induced stress applied to the TB: $\sigma = \Delta G / \varepsilon_0$.

The last result repeats the expression derived by Likhachev and Ullakko which could seem now to be in a contradiction with the stress obtained here for a single TB. Indeed, let us consider a simple case of two adjacent TBs in the sample subjected to a magnetic field which is strong enough to saturate magnetization in all twin variants⁴. If we now try to consider the stresses acting on these two TBs as two independent normal stresses, we can get double increase of the maximum stress: $\sigma = 2 K_u / \varepsilon_0$. By increasing the number of TBs, we could get even larger stress output. This obviously contradicts the limited

³ Actually, ΔG is dependent on the local magnetic field distribution on both sides of the TB, at fields below saturation. As the TB was shifted by a distance $L_1 - L_0$, the field distribution also changed. However, the TB position change can be made so small that the field distribution "shifts" with the boundary.

⁴ A case with multiple TBs is more complex because the local field distribution is now affected by the arrangement of the neighbor twin variants. At fields beyond the saturation field, ΔG is equal to K_u , magnetization becomes uniform and the driving stress acting on a particular TB is not dependent on the location and number of the differently oriented twin variants presenting in the sample.

stress concept derived from the general thermodynamics approach and the experimental observations found in the literature.

The above contradiction came because of incorrectly treated *normal* stress concept which is not enough to describe multiple TB motion. In fact, only *shear* forces applied to twin variants along TB plane induce TB motion. If we now consider shear forces acting on the twin variants shown in Figure 3.4(a), it becomes apparent that the forces F_2 and F_3 compensate each other so that the resulting normal stress for the whole sample will be equivalent to the stress acting on one TB. It can be concluded further that for any number of parallel adjacent TBs the shear forces in the internal variants will compensate each other (in static conditions at saturation field).

Figure 3.4(b) presents another example of three twin variants arrangement in which two TBs are not parallel. Here we can see that the forces acting on the middle variant, F_2 and F_3 , do not compensate each other and will cause the middle variant to move in the vertical direction.

The next factor that should be taken into account, is mass inertia. For example, in the case depicted in Figure 3.4(a), one can expect that in a free, “levitating” sample (if we neglect the torques), the centre of mass of the middle variant will not move at all, while the side variants will move by the forces F_1 and F_4 , and the TBs will move towards the edges at equal velocities. But, if the side variants have different masses, the same forces will accelerate these variants to different speeds and the velocities of the TBs will be not equal.

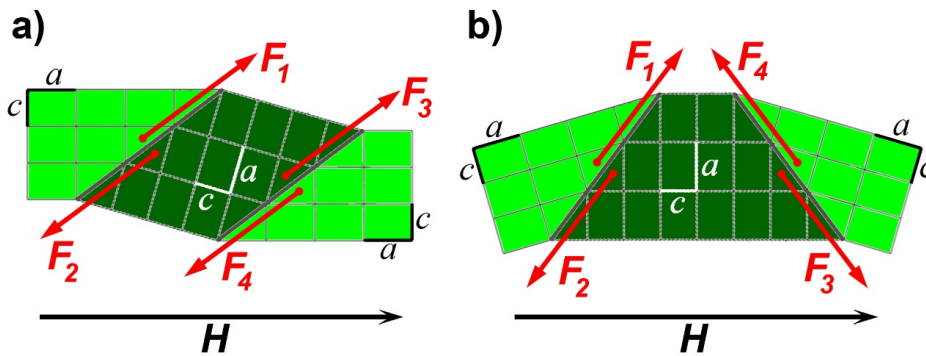


Figure 3.4: Shear stresses induced by a magnetic field in an MSM sample having three twin variants structure: (a) with parallel TBs, and (b) with non-parallel TBs. The vectors F_1 - F_4 denote the shear forces induced by the applied magnetic field H . At any boundary the shear stresses appear as pairs of equivalent forces (e.g., $F_1=F_2$ and $F_3=F_4$).

Therefore, the equivalent normal stress, defined by Equation 1.2, is valid for a particular TB (with the energy ΔG dependent on the local field distribution), and the actual shear

forces acting on twin variants on both sides of the TB can be calculated from this normal stress. In the case of multiple TB motion, one should take into account the shear forces acting on all twin variants and solve a system of differential equations to describe each twin variant's variable-mass motion.

3.6 Concluding remarks

The presented macroscopic model demonstrates a novel approach to twin boundary dynamics taking into consideration the masses of the twin variants moving in the shear direction. The following important conclusions can be made based on the model analysis:

- Four different actuation modes are possible for a single TB motion, from which two modes correspond to increase, and two other modes correspond to decrease of the mass of the moving variant. In both cases, elongation and contraction of the sample can occur, depending on the c -axis orientation in respect to the magnetic field direction. For each actuation mode, a second-order differential equation for the TB position is derived.
- Based on the analysis of the differential equations obtained for different actuation modes, we found that a stable solution always exist in the case of increasing mass of the moving variant which is therefore most suitable for the experimental observations. Equation 3.3 enables one to retrieve such motion parameter as the total driving stress, $\sigma_{mag} - \sigma_{res}$, from the measured temporal TB velocity and position dependence, if differentiation of the velocity signal is applicable. Alternatively, simulation of the TB velocity and position temporal dependencies can be done by solving the above equation with modelled magnetic field-induced and resistance stresses. Saturation of TB velocity is predicted to occur after the acceleration region (Equation 3.4).
- The magnetic field-induced stress, σ_{mag} , can be evaluated using Equation 1.2, for a particular TB. From this normal stress, the actual shear forces acting on twin variants on both sides of the TB can be obtained. In a case of multiple TBs motion, one should calculate the shear forces acting on all twin variants and solve a system of differential equations describing each twin variant's variable-mass motion.
- A sample's cross-section variation along the path of a TB is shown to cause only temporal variation of the TB velocity (*i.e.*, change in acceleration/deceleration) without affecting the saturation velocity value defined by Equation 3.4.
- A scaling effect, which follows directly from the derived motion law, points to an increase of the initial acceleration proportionally to the decrease of the sample height (more exactly, to the initial height of the moving variant). This can lead to a nearly proportional decrease of the actuation acceleration times with decreasing the sample size.

- The shear forces developed by a magnetic field, lead to a deformation of the sample's shape. Therefore, one should avoid constraining of the sample in an experiment. In particular, the sample cannot just lay on a support, but preferably it should be fixed rigidly on some point to a holder, without any constrains applied to the parts which are allowed to move.

4 Materials and methods

The present chapter describes the materials, tools and apparatus used in the experimental investigations, and modelling methods utilized in this Thesis. The Author contributed in the development of the apparatus for twinning stress and magnetic anisotropy measurements, assembled and developed the pulsed magnetic field actuation and high-speed camera setups, and wrote the scripts for modelling the twin boundary motion.

4.1 Ni-Mn-Ga samples

Few high-quality $\text{Ni}_{50.0}\text{Mn}_{27.9}\text{Ga}_{22.1}$ (± 0.5 , at. %) samples obtained from AdaptaMat Ltd., Finland, were studied. According to the manufacturer data, the martensite-austenite transformation temperatures of the used alloy are about 40°C and structure of the samples is five-layered modulated martensite at room temperature. The lattice parameters at room temperature are: $a=5.965 \text{ \AA}$, $b=5.945 \text{ \AA}$, $c=5.605 \text{ \AA}$ and $\gamma=90.3^\circ$, and the Curie temperature, T_C , is $376\pm 1 \text{ K}$, which are typical for the mentioned composition.

Using home-made AC low-field magnetic susceptibility apparatus, we determined the martensite transformation temperatures of the alloy as follows: $(A_s + A_f) / 2 = 317\pm 1 \text{ K}$ and $(M_s + M_f) / 2 = 310\pm 1 \text{ K}$, with the differences $|A_s - A_f| \approx |M_s - M_f|$ not exceeding 3 degrees. The temperature values and the sharp forward and reverse martensite transformations correspond well to the data presented in the literature for similar alloy compositions (see, e.g., Straka *et al.*, 2013).

The austenite start temperature of the samples was enough high, so that they never transformed into austenite during the experiments. If a sample cools down after such a transformation, it would immediately create a randomly oriented twins which were never observed in our studies. Instead, the Author was able to control the samples' twin variant structure on the level of individual twin boundaries in all the experiments.

The maximum transformation strain, ε_0 , was measured to be $6.0\pm 0.1 \%$, which is typical for 5M Ni-Mn-Ga alloys and agrees with the strain of $\sim 6.06 \%$ calculated from the lattice parameters, taking average of a and b .

Initially there were three samples with dimensions of $\sim 1 \times 2.5 \times 20 \text{ mm}^3$, with all faces nearly parallel to the $\{1\ 0\ 0\}$ planes of the cubic austenite. From these samples, one was saved for the magnetization characterization and two others were cut into smaller cuboid pieces with cross-sections of approximately $1 \times 1 \text{ mm}^2$ and lengths varied from 6 to 10 mm, by a precision wire saw (Princeton Scientific Corp., WS-22). The cut samples were mechanically polished and after that electropolished at 253 K in an electrolyte solution of 3 parts of 60% nitric acid mixed with 1 part of ethanol, at a constant voltage of 16 V during $\sim 20 \text{ s}$.

4.2 Twinning stress measurements

Quasi-static twinning stress measurements were conducted with a custom-made uniaxial compressive stress-strain measurement setup. A linear piezo actuator (PI, PIFOC PD72Z4CAQ) was used to strain the sample and to measure the displacement with a built-in capacitive sensor. The force was measured by a piezo differential force sensor (Kistler, Type 9207) mounted on the above piezo actuator. A metal rod with a thin tip was connected to the force sensor, which pushed the sample during the measurements. The used differential force sensor was unable to determine the absolute force, but it produced consistent results when the measurement started just before the tip touched the sample thus giving the zero force level. Both the piezo actuator and force sensor were operated using the controllers (PI, E-709) and (Kistler, Type 5867B), correspondingly, which include data acquisition capabilities.

Prior to the measurements, the sample was put into a fully elongated single variant state by means of a mechanical stress and application of 1 T magnetic field, and glued on one side with epoxy to a rigid holder. Then, a single twin boundary was introduced on the free end of the sample by means of a mechanical stress. The type of the boundary was identified according to its projection on (100) plane (Sozinov *et al.*, 2011). The twinning stress was obtained by dividing the measured force by the sample cross-section.

4.3 Magnetic anisotropy measurements

To provide characterization of the magnetic properties of the studied samples, a special setup was assembled for magnetization measurements.

Prior to the measurements, a long MSM sample (measured $1.13 \times 2.61 \times 19.49$ mm³ in the contracted state) was converted into a single-variant state by means of a mechanical stress and 1 T magnetic field application, with the shortest *c*-axis oriented along the sample (*i.e.*, into a fully contracted state), for easy-axis magnetization measurements, or perpendicular to the sample's largest dimension (fully elongated state), for hard-axis magnetization measurement. A coil made from insulated copper wire of 0.1 mm in diameter, was wound around the middle part of the sample, having 40 turns. When elongated, the sample with the coil was glued with epoxy to a non-magnetic support, to prevent magnetic field-induced reorientation during the measurements with magnetization along the hard axis.

The MSM sample with the coil was placed between the poles of an electromagnet (LakeShore, EM4-HVA) with its largest dimension aligned with the field. The magnetic field was sweeping in the range of ± 700 kA/m at a frequency of 1 Hz using a transistor H-bridge connected to the output of a DC power supply (Delta Elektronika, SM45-70D). The applied field was measured with a standard search probe coil located close to the sample's surface in the middle. The sample's internal field was measured with the coil wound around the central part of the sample. Both coil voltages were integrated using a flux meter (M-Pulse, M-Flux 3000), to obtain the flux values that were recorded with a data acquisition board (NI, USB-6361). The flux data were transferred to a PC and then

recalculated to the correspondent field values. During the measurements, the sample was in a direct contact with the poles (estimated air gap was ~ 0.1 mm or less because of the sample edges' roughness), which allowed us to neglect the demagnetization factor in the field calculations.

4.4 Pulsed magnetic field actuation setup

In this study, we utilized laser Doppler vibrometry technique to measure the actuation velocity of a Ni-Mn-Ga sample subjected to a pulsed magnetic field. The main advantage of this method is direct non-contact velocity measurement based on the Doppler shift of the reflected laser beam frequency due to the motion of the target surface. Usually the output of a laser Doppler vibrometer (LDV) is a continuous analogue voltage that is directly proportional to the target velocity component along the direction of the laser beam. The LDV used here also provided a displacement signal from counting the light / dark fringes on its detector.

Figure 4.1 shows a schematic of the experimental setup explaining the arrangement of the LDV laser head, solenoid, sample holder and the MSM sample. The laser head, solenoid and sample holder were mounted on a vibration isolation platform (VIBRAPLANE 2210, Kinetic Systems, Inc.) to exclude mechanical noises from the surroundings. The sample was glued on one side (the right side in the figure) with an epoxy to the sample holder, which enabled rigid mounting to the solenoid holder so that the free, unglued end of the sample could be placed inside the solenoid. All the above holders and also screws were made from plastics and ensured mounting of the coil with the sample at 3-4 centimetres away from any other metal parts of the setup.

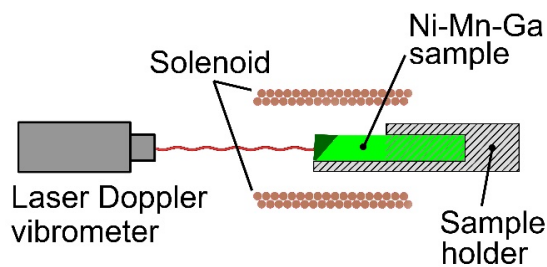


Figure 4.1: A schematic of the experimental setup for pulsed magnetic field actuation (not to scale). Two differently oriented twin variants in the sample are coloured with different shades of green.

The solenoid was connected to a high-voltage pulse generator (EMC, Transient 1000). An additional passive circuit was designed and connected in series with the solenoid to square and extend the current pulse (the passive circuit schematics and current pulses are

presented in Appendix A). The actuation velocity and displacement of the sample's free end were measured using an LDV from Polytec, Germany (Polytec, OFV-5000 and OFV-534), with a spot size of about $40\ \mu\text{m}$ at the used stand-off distance⁵. The coil current was calculated from the voltage drop on a wire resistor of $0.2\ \text{Ohm}$ connected in series with the solenoid. The current, actuation velocity and actuation displacement signals were digitized by an oscilloscope (Metrix® Scopix III OX 7204) which was triggered from the pulse generator⁶. For each pulse, the data including actuation velocity, displacement and current were recorded with the above oscilloscope and then transferred to a PC for a subsequent analysis. The measurement setup is capable to measure transient velocities up to $10\ \text{m/s}$ with time resolution of better than $1\ \mu\text{s}$ (the exact time resolution is dependent on the oscilloscope settings). A photo image of the LDV-based setup is presented in Figure 4.2.

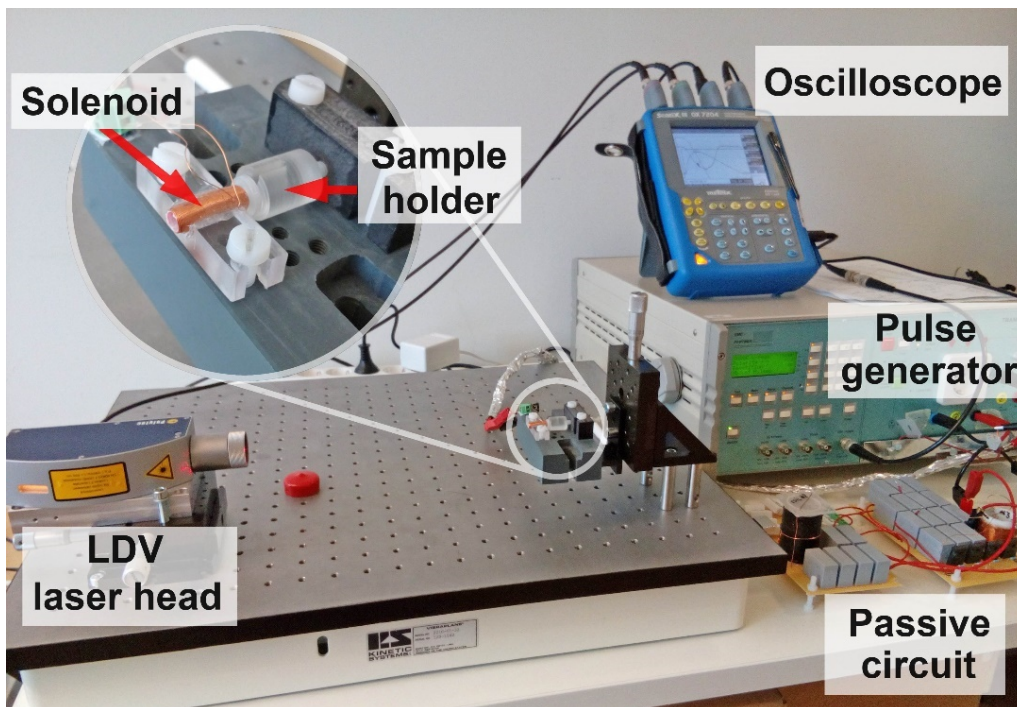


Figure 4.2: Photo image of the LDV-based setup with the solenoid of $16.3\ \text{mm}$ length.

⁵ In the experiments on fast actuation of MSM micropillars described in Section 5.6, we used an additional lens that reduced the spot size down to $1.5\ \mu\text{m}$ enabling focusing on the pillar's top surface.

⁶ In the initial setup, the sample actuation velocity signal was digitized with a data acquisition board (NI USB-6361) connected to a PC and triggered from the pulse generator. The time resolution in that case was limited to $0.5\ \mu\text{s}$ at 16 bit resolution. This modification was used only in Publication I.

Two solenoids were used as magnetic field sources for samples' actuation in different experiments. The first, mainly used solenoid has an inner/outer diameter of 4.3/5.1 mm, a length of $l=16.3$ mm, and consists of $N=140$ turns of an insulated copper wire of 0.2 mm in diameter, wound in 2 layers. The axial component of the magnetic field inside the solenoid was calculated using the following equation:

$$H(I, x) = \frac{IN}{2l} \left[\frac{x}{\sqrt{R^2+x^2}} + \frac{l-x}{\sqrt{R^2+(l-x)^2}} \right], \quad (4.1)$$

where I is the coil current, R is the average coil radius ($R=2.4$ mm in the present case), and x is the distance from the coil edge. The axial field distribution is presented in Figure 4.3(a). The dashed area represents the working region of 6 mm in length where the active part of the sample was located during the measurements. According to Equation 4.1, the field deviation from the maximum value does not exceed 2% within this area. The maximum field value in the centre was used as the standard field in the experiments (see the formula in the inset in Figure 4.3(a)).

The second solenoid had a 3.15 mm inner diameter, 6.7 mm length and 60 turns in 2 layers of the same wire. The working region was restricted to 2 mm length with the field deviation within 2%, and it was used only with short, $\sim 50-70$ μs , magnetic field pulses. The magnetic field strength in the centre, as acquired by Formula 4.1, is: $H = 7.89 \frac{\text{kA}}{\text{m}}/A$.

The setup allows magnetic field generation in a wide range of fields ($\sim 0.01-2.5$ T), pulse durations ($\sim 50-120$ μs) and shapes (nearly square, semi-sinusoidal and others).

4.5 High-speed camera setup

In order to capture the TB motion with a high-speed camera, the setup described in the previous section was modified. Instead of the solenoid, two coaxial coils connected in series (Helmholtz configuration) were used to generate the magnetic field. Each coil has an inner/outer diameter of 8.1/10 mm and consists of $N=20$ turns of an insulated copper wire of 0.2 mm in diameter. The coils are separated by an edge to edge distance of 4.2 mm. Because the actual geometry slightly differs from the Helmholtz configuration, we used the following expression to calculate the axial magnetic field distribution:

$$H(I, x) = \frac{INR^2}{2} \left[\frac{1}{(R^2+(x-b/2)^2)^{3/2}} + \frac{1}{(R^2+(x+b/2)^2)^{3/2}} \right], \quad (4.2)$$

where I is the coil current, R is the average coil radius ($R=4.5$ mm in this case), b is the distance between the coils centres ($b=5.2$ mm), and x is the distance measured along the coils' axis. The calculated axial magnetic field distribution is presented in Figure 4.3(b).

A schematic of the modified setup with the Helmholtz coil is shown in Figure 4.4. The coils' frame has an axial hole and a few openings between the coils, for mounting the sample holder with a sample and observing the surface of the sample with the high-speed

camera. The Helmholtz coil can be rotated by 90° providing the possibility to apply a magnetic field perpendicularly to the sample's length.

A high-speed camera (Photron, FASTCAM SA5) working at a frame rate of 775000 fps with a shutter time of 369 ns and pixel resolution of 256×16 , was used to acquire real-time images of the sample. These camera settings and optics accessories provided a time resolution of $1.29 \mu\text{s}$ and a spatial resolution of $\sim 8.3 \mu\text{m}/\text{pixel}$ in both directions. The high-speed camera and the oscilloscope were triggered using the pulse generator trigger output.

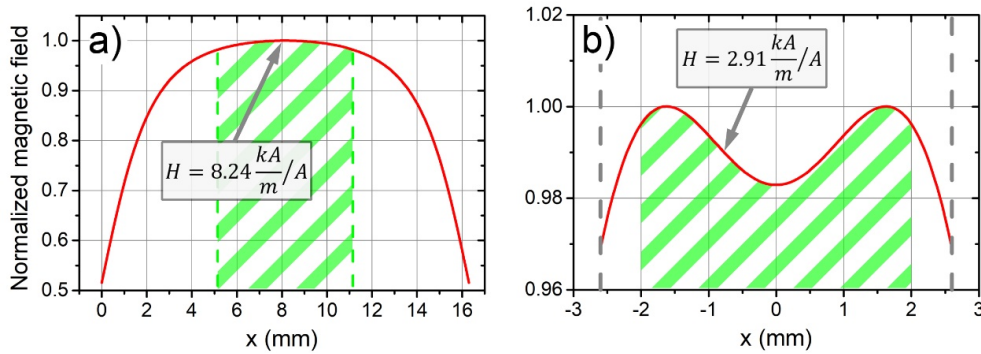


Figure 4.3: Calculated distribution of the magnetic field axial component inside the solenoid of 16.3 mm length (a) and the Helmholtz coil (b). The coordinate $x=0$ corresponds to the left edge of the solenoid in (a), and to the central position between two coils in (b), with the coils' centres marked by the grey dashed lines. The green dashed areas represent the working regions in which the field deviates within 2% of the maximum field value. Formulas in the insets were used for magnetic field strength calculation based on the coil current measurement.

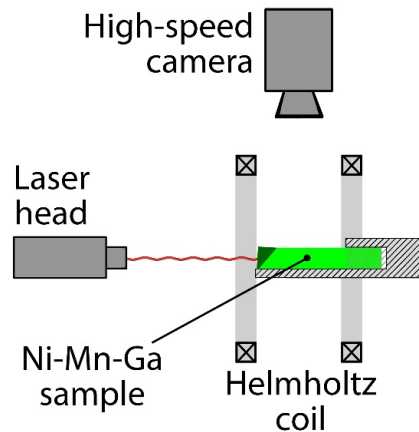


Figure 4.4: A schematic of the high-speed camera setup.

The high-speed imaging requires a special light source with a high intensity. In our experiments, we used a high power light-emitting diode (LED) light source (Photonic, F5100) to avoid heating of the sample, and switched off the light between the shootings.

The described setup allowed simultaneous real-time imaging and actuation velocity measurement of an MSM sample during the pulsed magnetic field actuation. A photo image of the setup is presented in Figure 4.5. We also used a modification of this setup in which the high-speed camera was attached to a microscope (Meiji, MT7000).

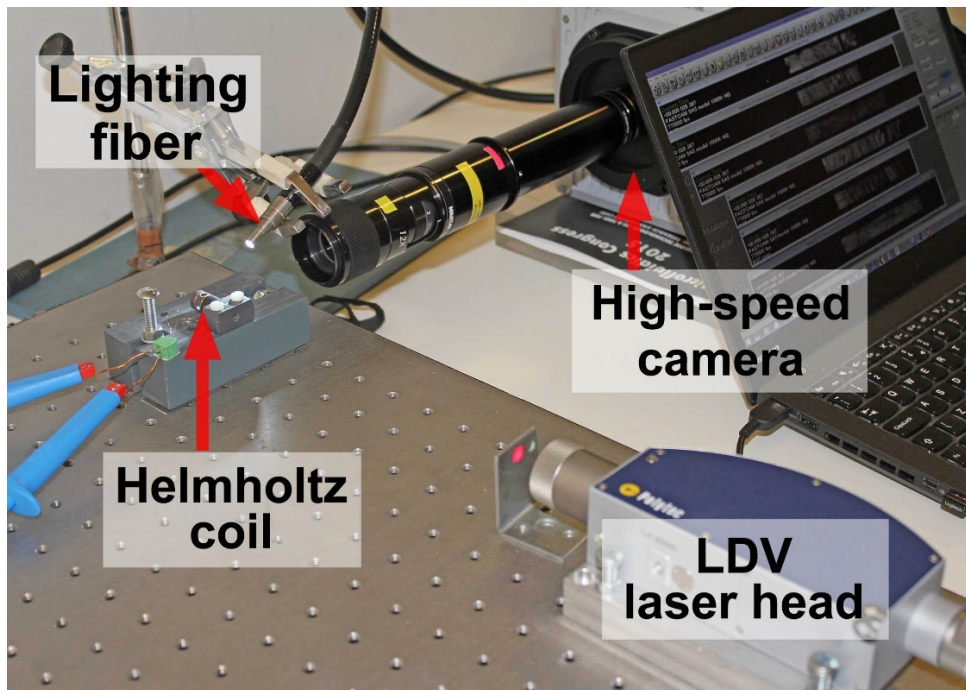


Figure 4.5: Photo image of the high-speed camera setup.

4.6 Modelling the twin boundary motion

The modelled temporal TB position, velocity and acceleration dependencies presented in this Thesis were obtained with standard numerical solving algorithms for ordinary differential equations found in Mathcad® Professional 14.0 and MATLAB® R2017a software.

The magnetic field was calculated based on the measured current pulse, using formulas found in Sections 4.4 and 4.5, and the magnetic field-induced stress was calculated according to Equations 1.1 and 1.2.

In Mathcad®, we used *odesolve* function which automatically uses the Adams-Bashforth methods. We specified the overall number of points so that the equivalent time interval was 10^{-8} s that ensured a stable solution.

In MATLAB®, we used *ODE45* function with the *RelTol* (relative error tolerance) parameter set to 10^{-4} . An example of the MATLAB script for numerical solving Equation 3.3 is presented in Appendix B.

5 Results and discussion

In this chapter we present and discuss the experimental and modelling results obtained in this Thesis. We start from the experimental characterization of the basic properties of the studied MSM samples, such as twinning stress and magnetization behaviour, which are required for the analysis of the main results. In Section 5.2, the experimental studies on single twin boundary motion of both types in saturation magnetic field are discussed. Next, we analyse the measured twin boundary velocities and their time dependencies in the context of the proposed macroscopic model, which allows us to evaluate the changes in twinning stress during twin boundary motion and leads to a concept of the velocity-dependent twinning stress. In Section 5.4, we investigate single twin boundary motion at fields below saturation, down to the switching fields that correspond to the mechanically measured twinning stresses. Section 5.5 describes the main features of the multiple twin boundary motion in saturation field and provides a comparison with the single twin boundary motion. In Section 5.6, we present the results on fast actuation of MSM micropillars demonstrating the scaling effect described by the model. Finally, Section 5.7 provides a discussion on the previous studies on twin boundary dynamics in relation to the results obtained in the present work.

All the presented experiments were conducted by the Author of this Thesis, except the twinning stress measurements and MSM micropillar actuation experiments described in Sections 5.1.1 and 5.6, correspondingly, which were performed by the Author together with M.Sc. D. Musiienko (Lappeenranta University of Technology, Finland). All the presented results were analyzed and interpreted by the Author.

All the measurements were conducted at room temperature of $21\pm 1^\circ\text{C}$.

5.1 MSM samples characterization

5.1.1 Twinning stress measurements

Figure 5.1 represents the results of the twinning stress measurements with one of the studied MSM samples. The sample cross-section was 0.9 mm^2 . Few scans were made for each TB type with a single TB propagating through the sample. The speed of the pushing tip was 0.035 mm/s that corresponds to the TB velocity of $\sim 0.6\text{ mm/s}$. After each scan the pushing tip was returned back to its zero position, and the TB was mechanically moved back to its initial position. The inset describes the initial twin variant arrangement for a TB of type 1. The TS was calculated for the cross-section measured for the right part of the sample. This explains the initial quasi-linear increase of the TS because the actual cross-section was continuously growing until the TB reached a “zero” position (see the red dashed line in the inset). In the case of type 2, the TB was initially put closer to the “zero” position and the initial stress growth is less pronounced.

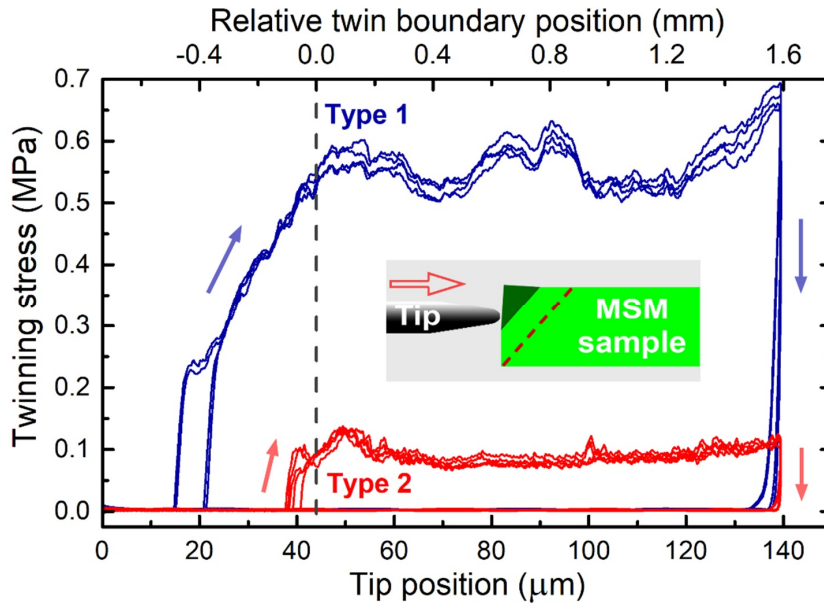


Figure 5.1: Twinning stress curves obtained for single type 1 (blue lines) and type 2 (red lines) TBs propagating through the MSM sample. Four scans for the TB of type 1 and five scans for the TB of type 2 are shown. The relative TB position was calculated based on the tip position and transformation strain. The inset schematically shows the initial two-variant arrangement in the case of type 1 TB, with the left (dark green) variant having c -axis directed along the sample. The red arrow shows the tip's motion direction. "Zero" TB position is denoted by the red dashed line.

From Figure 5.1, it can be seen that for both TB types the traveling path inside the sample was approximately 1.6 mm starting from the "zero" position. The average TS for type 1 TB is 0.56 MPa varying from 0.5 to 0.65 MPa. For type 2 TB, the average TS is 0.1 MPa with a plateau at ~ 0.08 MPa, and smaller deviation of ~ 0.06 MPa from the average value. Note that the subsequent scans demonstrate highly repeatable features revealing internal and/or surface defects which affect the TB motion. It can also be concluded that type 1 TB is more sensitive to these defects, as the curves for type 1 show much larger variation in TS value as compared to type 2 TB, for the same path. Both the average TS values and patterns are typical for 5M martensite (see, *e.g.*, twinning stress measurements for 50° C alloy presented by Sozinov *et al.* (2011) and Straka *et al.* (2011)). The smaller average TS value for type 1 of 0.56 MPa compared to 1 MPa for 50° C alloy, is explained by a strong temperature dependence of the TS for this boundary type – see Straka *et al.* (2012).

We note that the twinning stress measurements demonstrate a good quality of the investigated sample because a single TB of either type repeatedly propagated through the sample without any signs of pinning, or other TBs formation during the experiment.

5.1.2 Magnetic anisotropy measurements

Figure 5.2 presents the results of magnetization measurements for the long (~ 20 mm) MSM sample. The graphs numbered from 1 to 3 represent different sample states as follows: (1) a single variant state with the c -axis aligned with the field direction (magnetization along the easy axis). (2) A mixed variant state, *i.e.*, a state with multiple twin variants with both parallel and perpendicular orientations of the c -axis in respect to the magnetic field direction. (3) A nearly single variant state composed mainly of twin variants with the c -axis directed perpendicularly to the applied field (magnetization along the hard axis). The inset shows recalculated magnetization *versus* the applied field for the three states.

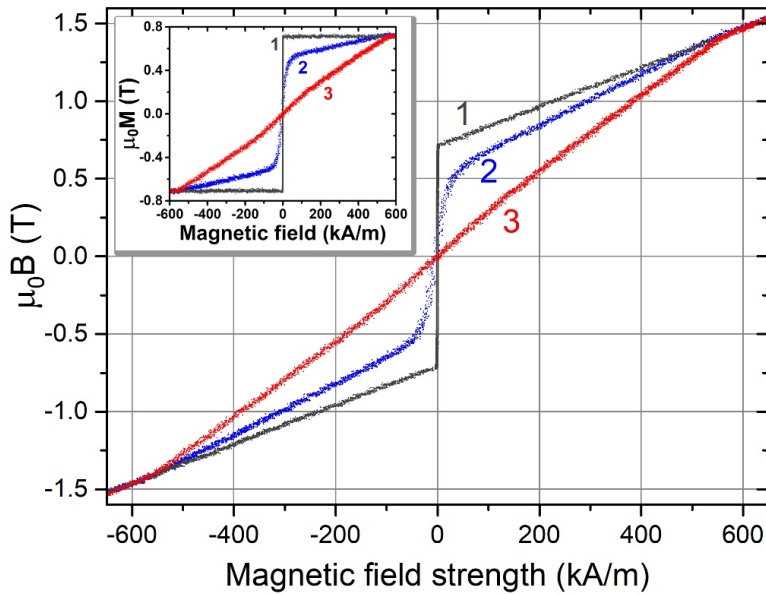


Figure 5.2: Magnetization curves in B - H coordinates measured for the MSM sample in different states: (1) single variant state with the easy c -axis aligned with the applied field, (2) mixed variant state, (3) nearly single variant state with the c -axis aligned perpendicularly to the applied field. The inset shows the dependence of magnetization M on the applied field H , recalculated from the B - H data.

The presented dependences are typical for 5M Ni-Mn-Ga martensite and reflect the basic magnetization mechanisms in this material. The magnetization along the easy axis quickly saturates (curve 1) because the magnetization process occurs only by the motion of 180° magnetic domain walls (with saturation field measured of about 2.5 kA/m in our case). In the case of the hard axis (curve 3), the internal magnetization starts to rotate

toward the applied magnetic field direction and the process is determined primarily by magnetocrystalline anisotropy energy. A slight deviation from a straight line indicates the presence of a small fraction of the easy variant appeared during magnetization. In the intermediate mixed case (curve 2), both magnetization processes are visible.

From the magnetization data, it is possible to retrieve the saturation magnetization, M_S , and anisotropy field, H_a , values. From the magnetization curve for the easy variant, we obtained: $\mu_0 M_S = 0.705 \pm 0.005$ T. The H_a value was determined from the intersection between the saturation level of the easy variant and a straight line fit found for the hard variant dependence: $H_a = 560 \pm 15$ kA/m.

Knowing the two parameters, M_S and H_a , one can calculate the uniaxial magnetic anisotropy constant, K_u :

$$K_u = \frac{\mu_0 M_S H_a}{2} = \frac{0.7 \text{ T} \times 560 \text{ kA/m}}{2} = 1.96 \times 10^5 \text{ J/m}^3. \quad (5.1)$$

The obtained K_u value coincides well with the value reported for a similar alloy composition at room temperature (Aaltio *et al.*, 2016). According to Equation 1.2, the maximum magnetic field-induced stress applied to a TB in magnetic fields $H \geq H_a$, is:

$$\sigma_{mag}^{max} = \frac{K_u}{\varepsilon_0} = 3.27 \text{ MPa}. \quad (5.2)$$

5.2 Single twin boundary motion in saturation magnetic field

5.2.1 Preliminary studies and development of the experimental setup

First, we will make a few remarks concerning our initial studies on the magnetic field-induced TB motion by the laser Doppler vibrometry technique, and development of the experimental setup.

We started from a setup similar to the described by Smith *et al.* (2014) placing a Ni-Mn-Ga sample in a single variant state close to the edge and outside of an air coil. But, instead of measuring the change in the reflected light from the top surface of the sample, we measured the sample's actuation velocity with the LDV. These first attempts immediately revealed several important things that needed to be solved: (i) the temporal dependencies of the velocity were not repeatable and sometimes few twin bands with different or mixed TB types appeared at different places after the pulsed actuation. In addition, the velocity signal often showed very fast and abrupt variations attributed to annihilation of the moving TBs. (ii) There was a tendency for the new TBs to appear near the corners of the sample. (iii) The magnetic driving force could not be controlled because the magnetic field decays quickly outside the air coil. In fact, only saturation fields could be applied for times less than 30 μs with a penetration depth limited to ~ 1 -1.5 mm.

Based on these preliminary experiments, the following conclusions were made: (i) a single TB of a known type should be created in the sample before the pulsed actuation. (ii) Preferably, the introduced twin variant at the end should occupy both corners of the sample. (iii) The sample (more exactly, its active part) should be placed inside a solenoid having enough length to create a nearly uniform magnetic field along the path of the TB.

All the measurements presented in the following sections have been acquired using setups described in Sections 4.4 and 4.5, and in accordance with the above conclusions. We have made hundreds of experiments with consistent and repeatable results, from which the most representative ones have been chosen to be placed in this Thesis.

5.2.2 Single twin boundary motion characterized by laser Doppler vibrometry

Prior to the measurements, the sample was set into a single variant state by applying a 1 T magnetic field along its shortest dimension, which fully elongated the sample. Further, by means of a mechanical stress (*i.e.*, by application of a force in the shear direction), the very corner of the sample was converted to the second variant in which the easy magnetization c -axis was aligned along the sample's length, like it is depicted in Figure 3.1(a). Thus, a single TB was created near the free end. The sample was glued on one side (the right side in the figure) to the sample holder. Importantly, only one variant was allowed to move, and no constraints were applied to it from the sample holder. Before and after the field pulse, the sample was photographed in a polarized light, to reveal the traveling distance of the TB. The type of the TB was identified according to the difference in the projections on (100) plane (applicable for the top side of the sample in the presented images).

Figure 5.3 presents photo images taken during an experiment on a single TB motion before (a, b) and after (c) the magnetic field pulse actuation. Here, the TB was identified to be of type 2. The driving force for the motion arises from the energy difference of the twin variants with different orientations of the easy c -axis in respect to the magnetic field direction. In the present case, the left variant is growing at the expense of the right one, and the boundary moves to the right. Consequently, contraction of the sample occurs along [100] direction of the crystal since the lengths of the martensitic crystallographic axes are different. The actuation velocity of the free end of the sample measured by the LDV is directly proportional to the TB velocity, with a coefficient nearly equal to the maximum transformation strain of the sample, ε_0 (see Section 3.1 for details).

Figure 5.4 shows the time dependencies of the actuation velocity measured for both TB types along with the applied current pulse. The calculated maximum magnetic field strength for the pulse is 900 kA/m and the magnetic induction is 1.1 T. From the actuation velocity data, it can be clearly seen that the process involves three parts: acceleration, a constant velocity region and deceleration. First, during the beginning of the current pulse, the motion starts when the magnetic field-induced stress is high enough to overcome the twinning stress. As the motion of the TB starts, both the mass behind it and the mass involved into the motion are accelerating. At some point, the magnetic field strength

creates saturation inside the sample and the magnetic field-induced stress, σ_{mag} , that tends the boundary to propagate further, reaches its maximum value (according to calculations, the saturation occurs at 8-10 μs from the pulse start). When the driving force is at the maximum and the moving mass is enough accelerated, a constant velocity region begins. Within this region, the whole mass behind the boundary is moving at a constant velocity. As the TB propagates further, new sample volumes are involved into the motion, being accelerated up to the same velocity. Thus, inertia plays an important role for limiting the maximum velocity. It can be seen from the figure that the constant velocity region begins at $\sim 10 \mu\text{s}$ for type 1 and at $\sim 20 \mu\text{s}$ for type 2 boundary. To a first approximation, this difference can be explained by the different masses being involved into the motion during the acceleration path (the initial masses of the growing variant are nearly the same for both types). At the descending part of the current pulse, when the sample is no longer in saturation, the driving force drops and the motion slows down. Because of the inertia of the already moving part of the sample, and depending on the resistance forces (including twinning stress), motion can last longer than the current pulse itself.

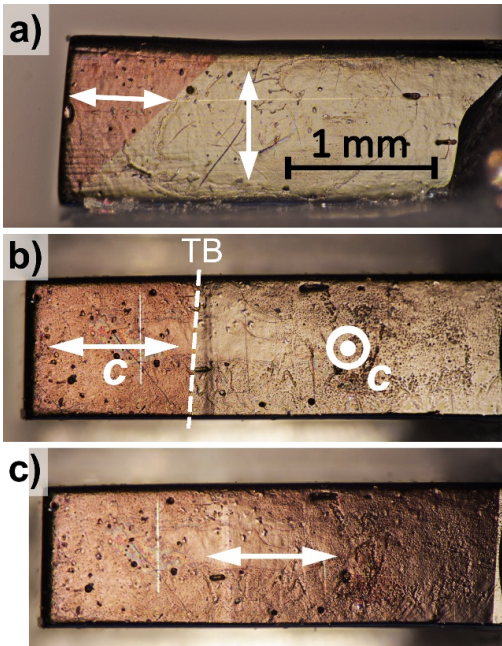


Figure 5.3: Optical images of a Ni-Mn-Ga sample with a single twin boundary of type 2. (a) Side view before the magnetic field pulse. (b) Top view before the pulse with the dashed line marking the TB. (c) Top view after the pulse. The colour contrast that differentiates the twin variants is due to the use of polarized light. White arrows show the orientation of the easy c -axis inside the twin variants. The magnetic field was applied along the sample with the solenoid of 6.7 mm length (see Section 4.4 for details of the setup). [Publication I]

From the measured actuation velocity data, the velocity of a single TB can be obtained by dividing the actuation velocity by the full transformation strain, ε_0 , of 6%. (In the case of the measurement exactly along the $[100]$ direction in the non-moving variant, we have to take into account the tilt angle β , but it gives only a small correction of $\sim 3\%$ that lies within the experimental error.) This gives the maximum TB velocities of 4.2 m/s and 33 m/s for type 1 and type 2 TBs, respectively, using the data in Figure 5.4.

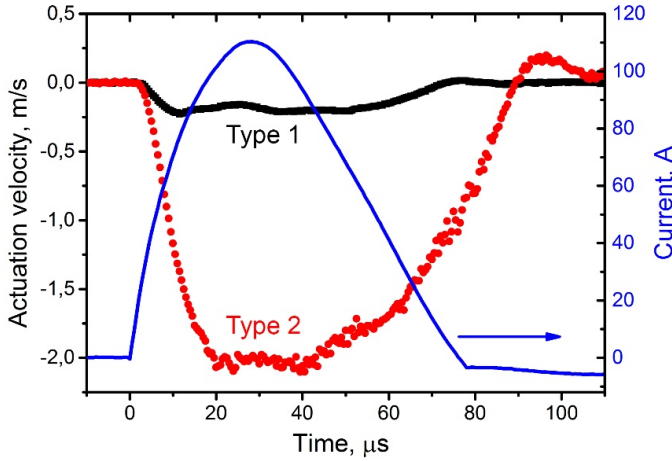


Figure 5.4: Actuation velocity (left axis) measured for a single twin boundary of type 1 (black) and type 2 (red) propagating through the sample during the magnetic field pulse. The blue curve shows the measured current pulse. [Publication I]

The TB traveling distance obtained from the top view photo images was further compared with the distance calculated from the actuation velocity data. For this, numerical integration of the actuation velocity temporal dependence was performed and the obtained value was divided by ε_0 . The calculated traveling distance for the twin boundary of type 2 is 2.05 mm. This value coincides well with the distance of 2.01 ± 0.05 mm obtained from the corresponded photo images (see Figure 5.3(b) and (c)). The same calculation performed for the type 1 boundary gives a value of 187 μm , which again is in a good agreement with the corresponding value of 0.19 ± 0.01 mm measured from the photo images (not presented).

From the measured actuation velocity we derived the actuation accelerations for both boundary types, during the rising part of the current pulse. By direct numerical differentiation of the measured velocity data we get maximum actuation acceleration values of 3.7×10^4 and 2×10^5 m/s^2 for type 1 and type 2 TBs, respectively.

5.2.3 Direct observation of twin boundaries motion

Although the LDV approach allowed us to capture the transient actuation velocity of the sample and estimate the TB velocity from these data, we were still lacking the direct observation of the TB motion. Thus, the next step was to capture the TB motion directly with the high-speed camera setup described in Section 4.5. This setup included a Helmholtz coil instead of the solenoid, in order to observe the sample surface during the pulsed magnetic field actuation. The TB position was directly acquired by the high-speed camera utilizing the light intensity contrast between the two variants, which arises from the surface tilting, under appropriate lighting. At the same time, we measured the sample's contraction velocity with the LDV as earlier.

The initial twin variant configuration in the sample was prepared as it was described in the previous section. Figure 5.5(a) and (b) show photo images taken from two sides of the sample (named here as S3) before the actuation, and Figure 5.5(c) and (d) show frame sequences (each third frame shown) acquired by the high-speed camera during two identical field pulses. For the initial position of the TB, we superimposed and scaled the frames from the camera on the top of the photo images (see Figure 5.5(a, b)), according to the clearly distinguishable features on the sample surface. This procedure was performed for every measurement revealing the actual spatial resolution. As it is seen from Figure 5.5(a) (top view), the introduced TB is of type 2. The frames shown below (see Figure 5.5(c)) clearly indicate that the boundary propagated through the visible part of the sample without any signs of splitting or additional boundaries nucleation. One can clearly see the acceleration region, nearly constant velocity region, and deceleration region in the TB motion. From the side view frame sequence shown on Figure 5.5(d), one can conclude that the motion of the growing variant occurs in a direction, which is parallel to the TB plane.

Note that the right part of the sample remains stable during the field pulse. Thus, the relative position of the TB for each top view frame can be determined as the coordinate of the boundary pixel multiplied by the spatial resolution. The calculated position data from the measurements with three different samples, named S1-S3, are shown in Figure 5.6(a), along with the magnetic field pulses. The lower field pulse was used to actuate the samples S1 and S2. Both pulses produced field enough for sample saturation during $\sim 70\%$ of the pulse length, with rise times (to saturation level) less than $4 \mu\text{s}$.

Figure 5.6(b) shows the TB velocity data numerically derived from the position dependencies. The samples exhibit a slightly different behaviour after the acceleration part, reaching different maximum velocities ranging from 36 m/s for S1 to 39 m/s for S3. TB velocity for S1 after reaching its maximum value at $\sim 22\text{-}32 \mu\text{s}$ starts to decrease and the boundary almost stops before the end of the pulse. From the high-speed camera frames, it was revealed that during the pulse an additional twin variant with two TBs of type 1 appeared and grew in the front of the initial TB preventing its motion⁷. For S2, there were no signs of additional TBs nucleation during the pulse time. Nevertheless, the TB motion decelerates while the field is above the saturation threshold. On the other hand, TB velocity for the sample S3 first saturates at the value of $\sim 31 \text{ m/s}$ and after that demonstrates second saturation region with higher velocities of $37\text{-}39 \text{ m/s}$. We attribute this behaviour to the samples internal and/or surface inhomogeneity, which affects the TB mobility. The other important feature of the observed motion is the acceleration region of $\sim 20\text{-}30 \mu\text{s}$, under maximum driving force, that is pronounced for all samples before reaching the saturation velocity. This phenomenon is attributed to both inertia of the accelerating mass, and strong internal friction dependence on the TB velocity.

⁷ Based on our observations, we believe that it was a residual twin presenting in the sample prior to the actuation. The thickness of this twin was so small that it could not be revealed by optical inspection.

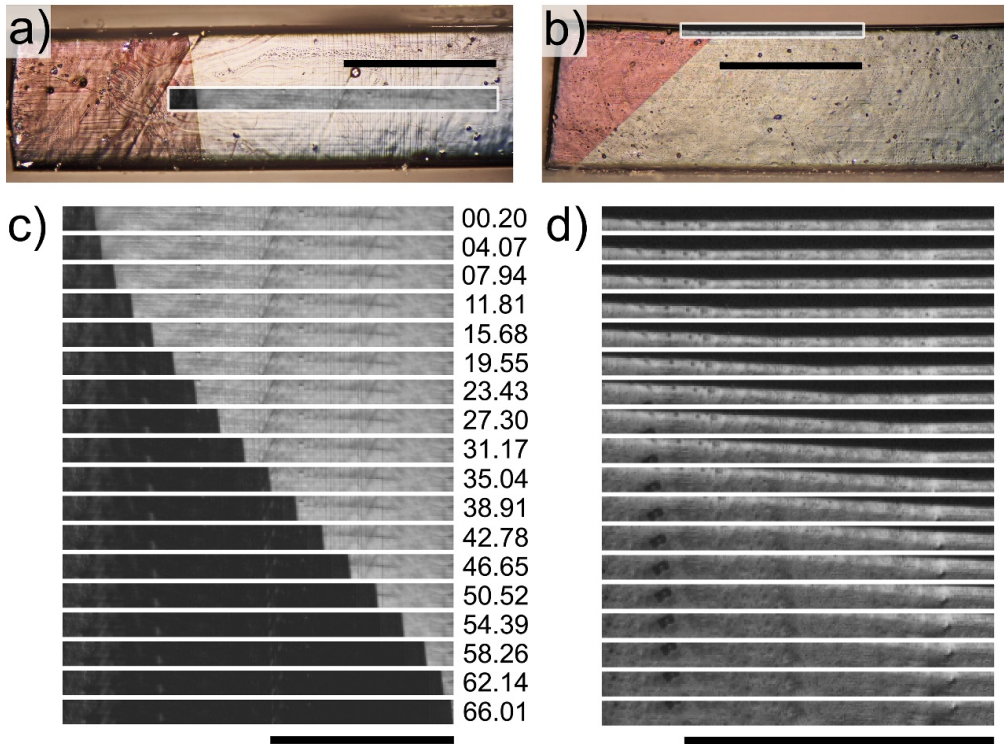


Figure 5.5: (a, b) Optical top view (a) and side view (b) images of the sample S3 with a single TB before the actuation. The colour contrast that differentiates the twin variants is due to the use of polarized light. The areas captured by the high-speed camera are outlined. (c, d) High-speed camera images acquired during two identical field pulses: top view (c) and side view (d). Time stamps are in μs . The scale bars are of 1 mm. [Publication II]

We compared the high-speed camera measurement described above with the actuation velocity measurement done using the LDV. In Figure 5.6(c), the solid red line repeats the TB velocity data obtained for S3, and open circles represent simultaneously measured actuation velocity signal. Here, the scaling factor between the axes is equal to ε_0 . The curves coincide well, proving that the LDV measurement properly describes the TB motion. A small excursion in the negative direction after the field pulse ends, is due to the glue acting as a spring, as is also visible in the high-speed camera frames (not shown). The velocity onset time, defined as the time between the start of the current pulse and the actuation velocity onset above the noise threshold, was $\sim 1 \mu\text{s}$.

Figure 5.6(d) shows the peak actuation velocity dependence on the magnetic field for sample S3, for single TB motion of type 2. The right axis represents the corresponding TB velocity scale. This graph clearly demonstrates velocity saturation at fields exceeding $\sim 0.5 \text{ MA/m}$ up to 1 MA/m . A conclusion can be made that there is no significant influence of the field-dependent resistance forces like magneto-static forces, on the TB motion.

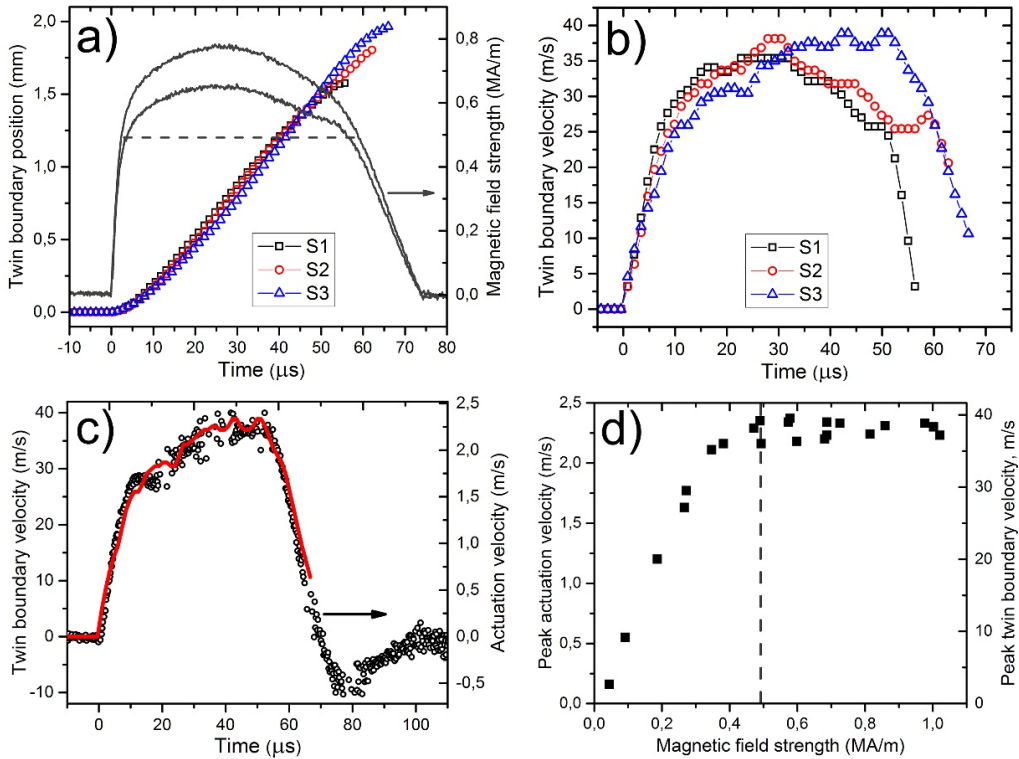


Figure 5.6: (a) TB position detected with the high-speed camera for samples S1-S3 (left axis) and magnetic field (right axis) *versus* time. (b) Calculated TB velocity *versus* time. (c) Superimposed graphs for calculated TB velocity (left axis, red line) and actuation velocity simultaneously measured with LDV (right axis, open circles). (d) Peak actuation velocity dependence on magnetic field. Dashed lines in graphs (a) and (d) represent the field level that saturates the driving force for TB motion.⁸ [Publication II]

5.3 Velocity-dependent twinning stress

From the results presented in the previous sections, it follows that there is a large difference in mobility of TBs of different types. Based on the obtained experimental data, in Publication II it was concluded that inertia and internal friction significantly affect the TB dynamics at the measured speeds. In addition, these results showed a minor role of the field-dependent resistance forces, such as magneto-static forces, on TB motion. To further clarify the underlying mechanisms governing the TB dynamics, we introduced a macroscopic mathematical model presented in Chapter 3. To more precisely characterize the TB motion, the LDV-based measurement setup was also modified by changing the 6.7 mm solenoid to a longer, 16.3 mm one, and improving the electrical circuit for current

⁸ The saturation magnetic field level was estimated here to be of ~ 500 kA/m, before the magnetization measurements were done. The measured anisotropy field is 560 ± 15 kA/m (see Section 5.1.2).

pulse generation. These modifications allowed us to extend the pulse length up to $\sim 120 \mu\text{s}$ having nearly square pulse shape with the rise time (to saturation field level) of the order of $2 \mu\text{s}$. With these pulse parameters, we could follow the TB motion at longer paths, measured up to 4-5 mm for type 2 and 0.3-0.5 mm for type 1 TBs.

We specially designed the LDV setup to have saturation field conditions during the actuation pulse. Physically saturation means that all the individual magnetic moments in both variants are aligned with the magnetic field and correspondent magnetic field-induced stress, σ_{mag} , reaches its maximum value of K_u/ϵ_0 (see Equation 5.2). In addition, the effects of magnetization rotation at the TB interface and domain walls motion are excluded from the resistance stress, σ_{res} , in saturation field.⁹

The applied magnetic field pulse is presented in Figure 5.7(a). The saturation field is achieved at $\sim 1.8 \mu\text{s}$ and maintained during $\sim 100 \mu\text{s}$. Prior to each actuation, the samples were photographed in polarized light to evaluate the TB type, the initial mass of the moving variant, m_0 , and the initial TB position, L_0 . Figure 5.7(b) shows $v_{TB}(t)$ dependencies derived from the measured contraction velocity $v_C(t)$, for both types of individual TBs propagated in the MSM samples. The boundaries travelled $\sim 5 \text{ mm}$ in the case of type 2, and $\sim 0.3 \text{ mm}$ of type 1. The velocity graphs clearly demonstrate three parts of the kinetics: (1) acceleration and (2) velocity saturation during the magnetic field pulse, and (3) deceleration after the field drops to zero. There is a distinct, about an order, difference between saturation velocities achieved for type 1 ($v_{TB} \sim 2\text{-}4 \text{ m/s}$) and type 2 ($v_{TB} \sim 35 \text{ m/s}$) boundaries. The acceleration and deceleration parts are very short for type 1 interface, whereas in the case of type 2, there is a very clear sign of the inertia effect. This effect is more pronounced after the field turns off and the mass (about 8 times larger compared to m_0 , for type 2 TBs), moving at $\sim 3 \text{ m/s}$ velocity, starts to decelerate because of the resistance forces. There are also oscillations visible in the measured velocity signal, which represent second-order effects, and will not be discussed here.

Based on the measured velocity data and the known parameters m_0 , L_0 and A_0 , the temporal dependence of the total driving stress, $\sigma_{mag} - \sigma_{res}$, was evaluated for the type 2 case, using Equation 3.3. The result is shown in Figure 5.7(c). It is seen that at the time $t \sim 1.5\text{-}2 \mu\text{s}$ from the beginning of the field pulse, the total driving stress sharply reaches $\sim 3 \text{ MPa}$ and then drops down to $1\text{-}1.5 \text{ MPa}$ within $\sim 10\text{-}20 \mu\text{s}$. The TB velocity changes from ~ 10 to 33 m/s . After few oscillations, the driving stress remains stabilized at $\sim 1\text{-}1.2 \text{ MPa}$ for both samples, until the magnetic field is switched off. After the field is removed, the driving stress immediately becomes negative reaching about -3.5 MPa , meaning that the resistance forces begin to decelerate the moving mass. Again, two different parts can be distinguished during deceleration: (1) fast deceleration part lasting approximately $50 \mu\text{s}$, with the velocity dropping from 30 m/s down to 5 m/s , and (2) slow deceleration part when the resistance stress approaches a nearly zero value (slight oscillations are caused by the noise) and the TB velocity diminishes very slowly.

⁹ We refer the reader to Sections 3.1 and 3.2 where we introduced all the parameters used hereafter.

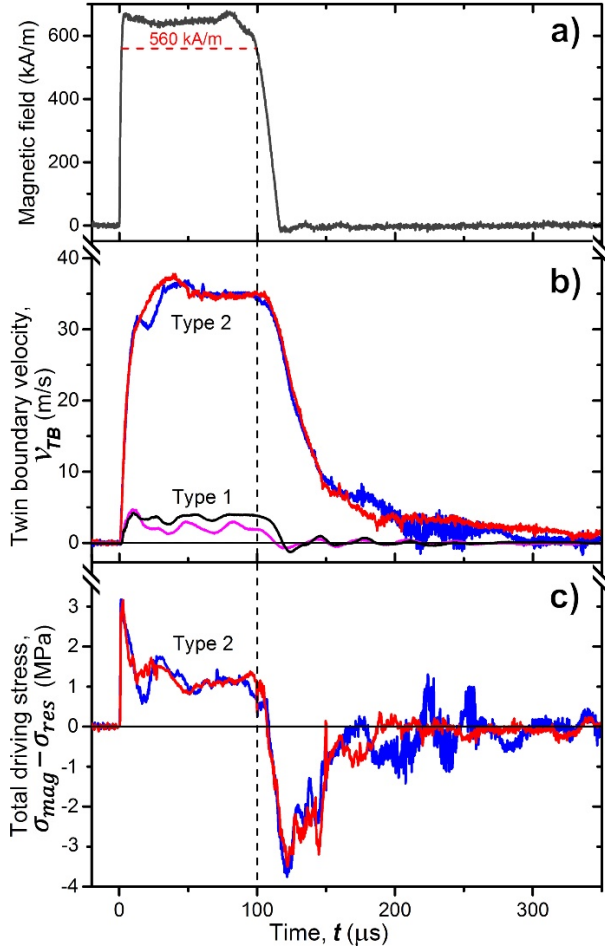


Figure 5.7: (a) Magnetic field pulse. (b) TB velocity, v_{TB} , dependencies on time, for single TBs motion of type 1 and 2, obtained from the measured contraction velocity, v_C . (c) The total driving stress, $\sigma_{mag} - \sigma_{res}$, versus time dependencies, derived from the TB velocity data for type 2. [Publication III]

The investigation of the possible resistance forces acting on the TB during its motion was of our particular interest. The twinning stress (TS) is the first obvious term that should be included in σ_{res} . If substituted into Equation 3.4, the predicted saturation TB velocities reach 53-58 m/s for the measured quasi-static TS ranged from 0.6 down to 0.1 MPa, at $\sigma_{mag} \sim 3.27$ MPa, determined by Equation 5.2. These values are much higher as compared to experimentally observed saturation TB velocities. Thus, additional terms should be added to the quasi-static TS in order to explain the difference.

We discuss first the saturation field conditions. One can expect few possible effects arising from the magnetic field that could suppress the motion of the TB. First, the skin effect from the eddy currents can influence at quickly rising/falling fields. The estimated penetration depth is of the order of 1 mm at the front of the actuation pulse. This effect

can only explain the observed lag of $\sim 0.8 \mu\text{s}$ between the magnetic field pulse start and the velocity signal onset, as the field pulse has nearly square shape. Other possible effects are related to magneto-static forces, torques because of the kinked shape of the sample, and eddy currents generated because of the motion of the sample in a strong magnetic field. All these magnetic field-related effects should be dependent on the field strength. However, our previous results (see Section 5.2.3) showed no decrease of the maximum TB velocity at fields beyond the saturation field, H_a .¹⁰ Thus, the above-mentioned field-related effects can be excluded. Furthermore, these effects are not related to the TB type. Therefore, they would suppress the supposed 53-58 m/s velocities to a similar extent, whereas an order of magnitude difference appears between the saturation velocities for the two different TB types.

Our hypothesis, which explains the experimental results, is velocity-dependent or dynamic TS caused by viscous-like damping of the TB motion. We describe the resistance stress σ_{res} as a sum of quasi-static TS value and a second, velocity-dependent term. To reveal the relationship between the TB velocity and the dynamic TS in saturation field, we subtract the total driving stress (values depicted in Figure 5.7(c) at $t < 100 \mu\text{s}$) from the saturation σ_{mag} value of 3.27 MPa. Figure 5.8(a) shows the obtained dynamic TS versus TB velocity for type 2 TBs (see the grey symbols). As it is seen from the graph, there is a very weak TS dependence on the velocity up to $\sim 8-10 \text{ m/s}$. Above these velocities, the dynamic TS starts to grow gradually, approaching $\sim 2 \text{ MPa}$ at TB velocities higher than 30 m/s.

The solid triangles represent the dynamic TS, σ_{res} , obtained with Equation 3.4 for saturation velocities measured with different samples, including our earlier results. The solid line is a fitting to a power law of the TS data, connecting two fixed points: at zero velocity (quasi-static TS, open circle) and saturation velocity of 35 m/s.

Due to the oscillations in the measured velocity, we could not perform the above calculations for type 1 boundary. Nevertheless, the TS estimation can be done based on the saturation TB velocity measured as 2-4 m/s. From Equation 3.4, it follows that the dynamic TS changes from the quasi-static value of $\sim 0.6 \text{ MPa}$ up to $\sim 3.26 \text{ MPa}$, actually depleting σ_{mag} . Taking into account previous studies showing velocity-independent TS at small TB velocities, at least up to 10^{-2} m/s (Faran and Shilo, 2015), we conclude that the dynamic TS for type 1 boundary has a sublinear and sharp dependence on the TB velocity (see the dashed line in Figure 5.8(a)).

According to the total driving stress dependence obtained for type 2 TBs moving at zero field (at $t > 120 \mu\text{s}$ in Figure 5.7(c)), the dynamic TS is about two times that in saturation field, for same velocity values. Evidently, compared to saturation field conditions, additional energy dissipative mechanisms are involved, primarily due to magnetization rotation and domain wall motion as the TB propagates further. From our data, these

¹⁰ We experimentally investigated that the saturation TB velocity does not decrease at magnetic fields up to 2.5 T, for both type 1 and type 2 TBs.

contributions are estimated to have negligible effect at velocities less than ~ 5 -8 m/s. Since this type of resistance forces is not related to the TB type, we can expect no such effect for type 1 TBs moving at ~ 3 -4 m/s.

Finally, to provide a validation of the proposed model, we compared experimental and simulated dependencies $v_{TB}(t)$ in saturation field, changing the initial mass of the moving variant, m_0 . The modelled curves demonstrate good agreement with the measured data, as seen in Figure 5.8(b).

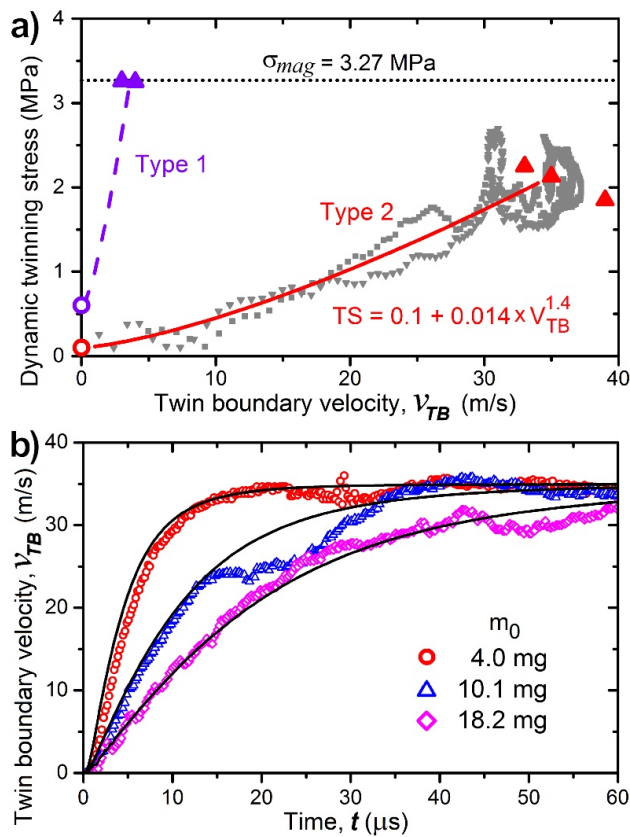


Figure 5.8: (a) Estimated dynamic TS dependencies on TB velocity in saturation magnetic field, for different TB types. Open circles represent the quasi-static TS and solid triangles – dynamic TS values at saturation velocities for different samples, according to Equation 3.4. Grey symbols represent the dynamic TS derived from the data displayed in Figure 5.7(c) for $t < 100 \mu$ s. Solid line is a power law fit to the grey symbols. (b) Measured (symbols) and simulated (lines) type 2 TB velocity dependencies on time in saturation magnetic field, for different initial masses m_0 . The dynamic TS was modelled with the formula in panel (a) and Equation 3.3 solved using Mathcad software with time interval of 10^{-8} s. [Publication III]

5.4 Single twin boundary motion at fields below saturation

In this section, we present the results on single TB velocity measurements in the mode “*Contraction 1*” (see Section 3.3), for both TB types at magnetic fields below saturation, with the LDV measurement setup.

Figure 5.9 demonstrates the results of our experiments on magnetic field-induced motion of a single TB of type 2 at different fields. Panel (a) presents the measured current and calculated magnetic field, and panel (b) shows the measured actuation velocity *versus* time. It can be seen that the applied field pulses have nearly square shapes thus allowing us to effectively control the field amplitude maintaining it close to a specified value during $\sim 100 \mu\text{s}$. The velocity graphs clearly demonstrate acceleration, velocity saturation and deceleration regions at all field amplitudes.

For type 1 TBs, due to the large vibrations in the velocity signal under square pulse actuation (see Figure 5.7(b)), we used a current pulse shape with a gradual increase and decrease. Figure 5.10 shows the curves obtained for a single type 1 TB motion. One can see saturation of the velocity as the field approaches and exceeds the anisotropy field of about 0.7 T, similarly to type 2 TBs, but at much smaller values of the TB velocity.

Using the data presented in Figure 5.9 and Figure 5.10, we obtained dependencies of the peak twin boundary velocity on the applied magnetic field and magnetic driving force, which are shown in Figure 5.11. For TB of type 2 the peak velocity is, therefore, the saturation velocity. In the case of type 1 TB, it was experimentally tested that the TB can follow the change of the magnetic field with the used current profiles. Thus, the used peak values we believe to be close to saturation values because of the low mobility of type 1 TBs. In addition, the down triangles in Figure 5.11 represent the threshold fields and correspondent driving stress levels at which the motion of TBs was observed to begin.

In Figure 5.11(a) the TB velocity saturation can be clearly seen for both TB types as the magnetic field approaches the anisotropy field of $\sim 560 \text{ kA/m}$. The minimal observed threshold (switching) magnetic field values are 14 and 50 kA/m, for type 2 and type 1 TBs, respectively (with correspondent TB velocity detection threshold better than 0.1 m/s). There is a distinct difference in the velocity behaviour as the field drops closer to the threshold value, which is more pronounced in Figure 5.11(b), where the peak velocity is plotted *versus* magnetic driving force. The threshold magnetic field-induced stresses, according to Equation 1.2, are 0.16 and 0.55 MPa, for type 2 and type 1 TBs, respectively. These values are in a very good agreement with the measured quasi-static twinning stress values of 0.1 and 0.56 MPa (see Section 5.1.1).

We should note, however, that the actual field distribution at low fields is expected to be highly inhomogeneous along the TB plane due to the high anisotropy of the alloy, whereas Equation 1.1 assumes homogeneous field distribution. Therefore, we can expect an overestimation of the driving force at low fields, at least below $\sim 100 \text{ kA/m}$.

At moderate field values, between ~ 100 kA/m and the anisotropy field of 560 kA/m that correspond to driving forces from ~ 60 to ~ 190 kJ/m³, both curves demonstrate a quasi-linear trends with slopes of 2.1×10^{-4} and 4.7×10^{-5} m⁴/(J·s), for type 2 and type 1 TBs, respectively. Note, that there are no signs of any threshold-like or bimodal behaviour in this range of the driving force, for both TB types.

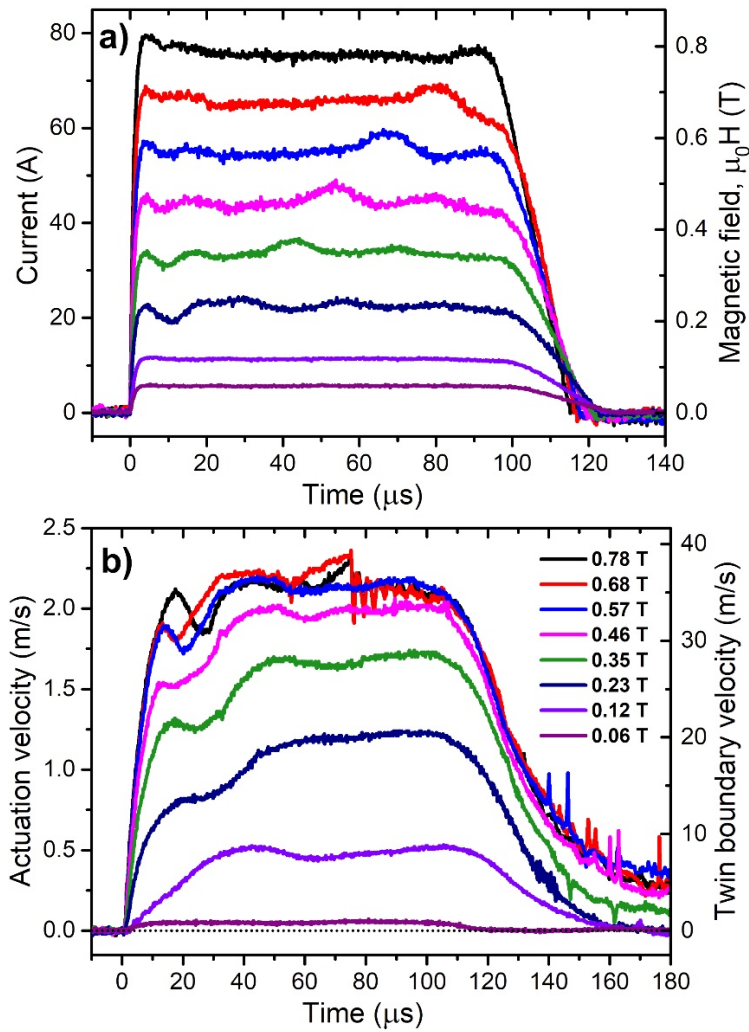


Figure 5.9: (a) Measured current (left axis) and calculated magnetic field (right axis) for pulses of different amplitudes. (b) Measured actuation velocity (left axis) and calculated TB velocity (right axis) *versus* time for a single type 2 twin boundary motion induced by the pulses presented in (a). The same colour scheme is used in both panels.

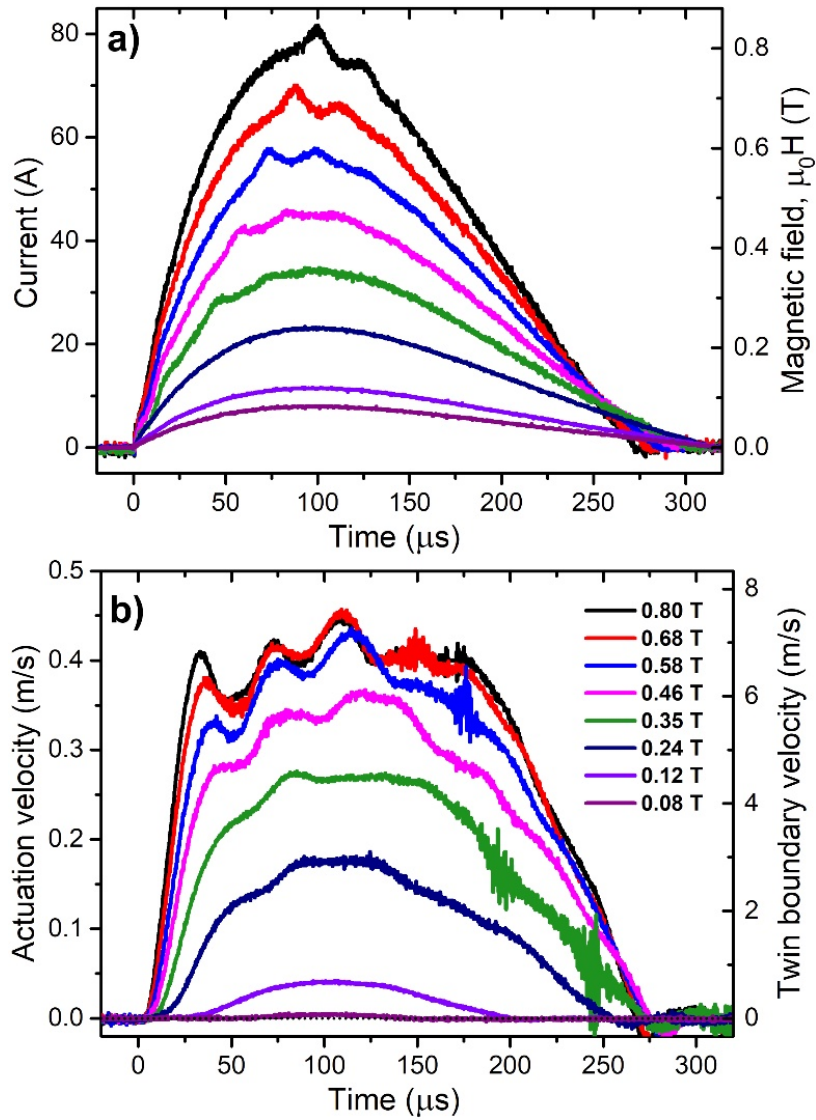


Figure 5.10: (a) Measured current (left axis) and calculated magnetic field (right axis) for pulses of different amplitudes. (b) Measured actuation velocity (left axis) and calculated TB velocity (right axis) *versus* time for a single type 1 twin boundary motion induced by the pulses presented in (a). The same colour scheme is used in both panels.

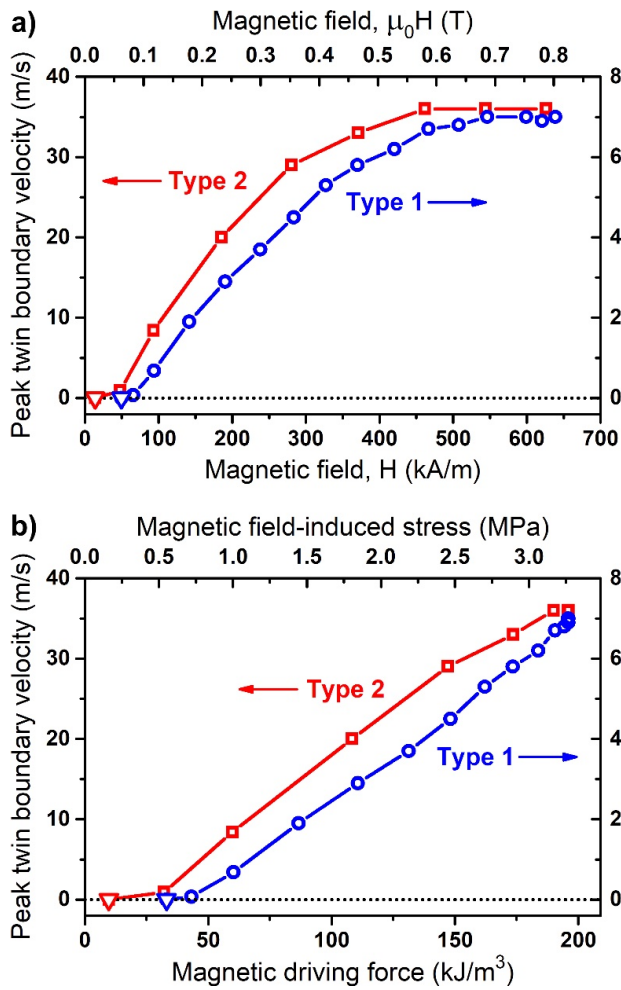


Figure 5.11: Peak twin boundary velocity *versus* applied magnetic field (a), and magnetic driving force (b), for type 2 (red squares, left axis) and type 1 (blue circles, right axis) boundaries. The points are plotted based on the data presented in the two previous figures. The downward triangles represent the threshold field level (*i.e.*, switching field) measurements, at which the TB motion starts. Magnetic field was calculated from the measured current. Magnetic driving force and magnetic field-induced stress were calculated using Equations 1.1 and 1.2, correspondingly.

The data points presented in Figure 5.11(b) describe the TB motion in a sense of the kinetic relation approach, *i.e.*, they show the relation between TB velocity and the driving force. In the kinetic relation approach, inertia is neglected and the instant TB velocity is directly defined by the driving force. In this respect, we should emphasize that TB acceleration and velocity are defined not only by the applied driving force, but also by variable-mass dynamics and velocity-dependent twinning stress as it was shown in the previous section. In fact, the peak velocities shown in Figure 5.11 were achieved by the moving TBs because of reaching a balance between the magnetic driving force, velocity-dependent resistance force and inertia of the growing mass. Thus, the kinetic relation approach based on a formal relation between the saturation (or average) TB velocity and the driving force, is valid only for steady-state conditions and actually ignores the dynamics-related effects like inertia and velocity-dependent forces.

In the previous section, we observed a viscous-like damping of the TB motion which was described by the dynamic twinning stress dependencies on TB velocity for both TB types (see Figure 5.8(a)). These dependencies were estimated for saturation field conditions and at zero field. The data in Figure 5.11(b), obtained at fields below saturation, allows us to construct similar dependencies using Equation 3.4. The result is shown in Figure 5.12.

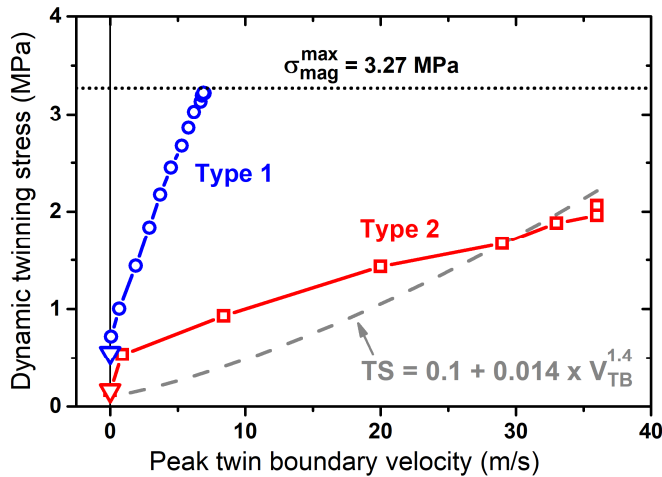


Figure 5.12: Dependencies of the dynamic twinning stress on TB velocity for type 1 and type 2 boundaries, derived from the data presented in Figure 5.11(b). The grey dashed line shows estimated dependence for type 2 TB in saturation field from Figure 5.8(a).

It is seen from Figure 5.12 that in the case of type 1 TB, we have a very good agreement with the previously assumed quasi-linear behaviour depicted in Figure 5.8(a). For type 2, the threshold stress (correspondent to switching field) and stresses correspondent to large TB velocities of 30-40 m/s, are laying very close to the saturation field stress curve. At moderate TB velocities the points are located above the saturation field stress curve showing larger resistance stresses as compared to saturation. This behaviour can be naturally explained by additional energy dissipative mechanisms due to magnetization rotation and domain wall motion as the magnetic field is far below the saturation field. At very small velocities, however, when both the field and TB velocity approach zero values, these mechanisms again disappear and the resistance stress approaches its quasi-static value. All these effects are weaker in the case of type 1 TB because the velocity-related component in the resistance stress is much stronger.

We note again that the used equation for magnetic driving force leads to an overestimation of the magnetic field-induced stress and, therefore, of the resistance stress. Then, for velocities less than 10-15 m/s in the case of type 2, and 2-3 m/s of type 1, the real resistance stress should be lower.

In connection to our observations, we can mention the recent study by Zreihan *et al.* (2018) who reported on mechanically measured twinning stress dependence on the load rate for type 2 TBs (see our comments on this work in Section 1.2.1). For TB velocity ranged from 8×10^{-5} to 0.03 m/s, they observed an increase of the TS from 0.09 to 0.15 MPa, *i.e.*, by 1.5 times.

We can therefore conclude that an additional research is required in order to clarify the velocity dependence of the dynamic twinning stress in the region of small driving forces.

5.5 Multiple twin boundaries motion in saturation magnetic field

In this section, we compare the actuation velocities and accelerations for single and multiple TBs motion of type 2 interfaces, acquired with the LDV measurement setup.

For single TB motion, we realized two actuation modes named “*Contraction 1*” and “*Elongation 1*” (see Section 3.3) which correspond to an increase of the mass of the moving variant. For multiple TBs motion, we introduced few type 2 TBs by means of a mechanical stress. The initial twin variant arrangements can be seen in Figure 5.13, in which the directions of the applied field and TB velocities are marked by arrows. We used the solenoid as the magnetic field source for contraction mode, and the Helmholtz coil rotated by 90° for elongation mode. The saturation field conditions were reached during $\sim 4 \mu\text{s}$ from the pulse start and maintained up to 50-60 μs , except the multiple TBs motion in contraction mode where the saturation field region lasted about 25 μs .

Figure 5.14(a) summarizes the results of the actuation velocity measurements, obtained for contraction and elongation modes, for single TB and multiple TBs motion. Figure 5.14(b) shows actuation acceleration curves that were numerically derived from the actuation velocity data.

First, we note that in the case of single TB motion, the velocity graphs look very similar both in contraction and elongation, with approximately same saturation velocities of ~ 2.1 - 2.3 m/s and peak actuation acceleration of $(3.2\text{-}3.7) \times 10^5$ m/s² at $t \sim 3 \mu\text{s}$. This points to the same dynamics behaviour with increasing mass of the moving variant as it was described in the model (see Section 3.3).

Next, one can expect that in the case of multiple TBs motion, the actuation velocity and acceleration will be increased due to the simultaneous motion of few TBs, in comparison to single TB motion. Indeed, we can observe 5.5 m/s peak actuation velocity in contraction mode for three simultaneously moving TBs compared to ~ 2 m/s measured for a single TB. Actuation acceleration graphs demonstrate accelerations up to 7×10^5 m/s² for multiple TBs motion, *i.e.*, about two times more compared to a single TB.

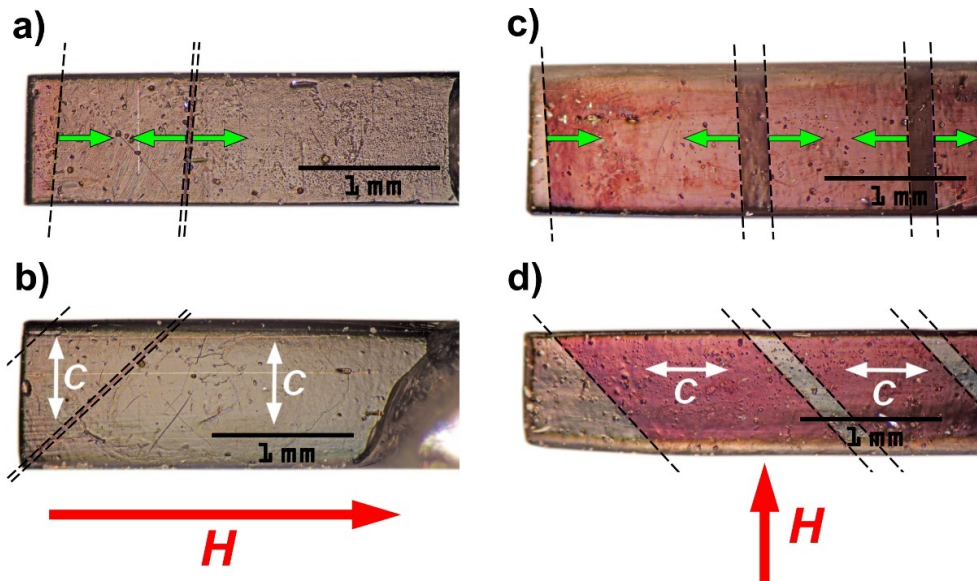


Figure 5.13: Optical images showing initial twin variant arrangements in the samples used for multiple type 2 TBs motion observation. (a, b) Top (a) and side (b) views of the sample actuated in contraction mode. The laser beam was focused on the upper part in (b) so that the motion of all the TBs could be captured from the very beginning of the magnetic field pulse. (c, d) Top (c) and side (d) views of the sample actuated in elongation mode. In all images, the left end of the sample is the free end. The TBs are marked by thin dashed lines. The colour contrast that differentiates the twin variants is due to the use of polarized light. Green arrows in (a) and (c) show the twin boundaries' motion directions. White arrows in (b) and (d) show the orientation of the easy c -axis inside the larger twin variants. The magnetic field directions are denoted by the red arrows in respect to the side views (b) and (d).

On the other hand, five TBs moving in elongation mode, show noticeably smaller peak velocity and acceleration as compared to the three TBs moving in contraction mode. This difference can be explained by the effect of inertia. First, in the case of contraction, the most left twin variant has a very small mass as compared to the elongation case (see Figure 5.13(b) and (d)). According to the model, we can expect that the initial acceleration in contraction will be much larger because of the scaling effect explained in Section 3.4. Second, each TB takes part in the motion and, moreover, we can expect the same magnetic-field induced stress acting on each TB in saturation field (see Section 3.5). However, the mass behind the TB increases with the distance from the free end, meaning that acceleration will decrease for far-standing TBs. In addition, the actual shear forces distribution should be taken into account. Therefore, the three TBs all located close to the free end can produce faster motion compared to five TBs distributed along the sample length. An important conclusion coming from these observations is that mass inertia and shear forces distribution significantly affect the dynamics of multiple TBs motion which cannot be reduced to a simple superposition of individual twin boundaries movements.

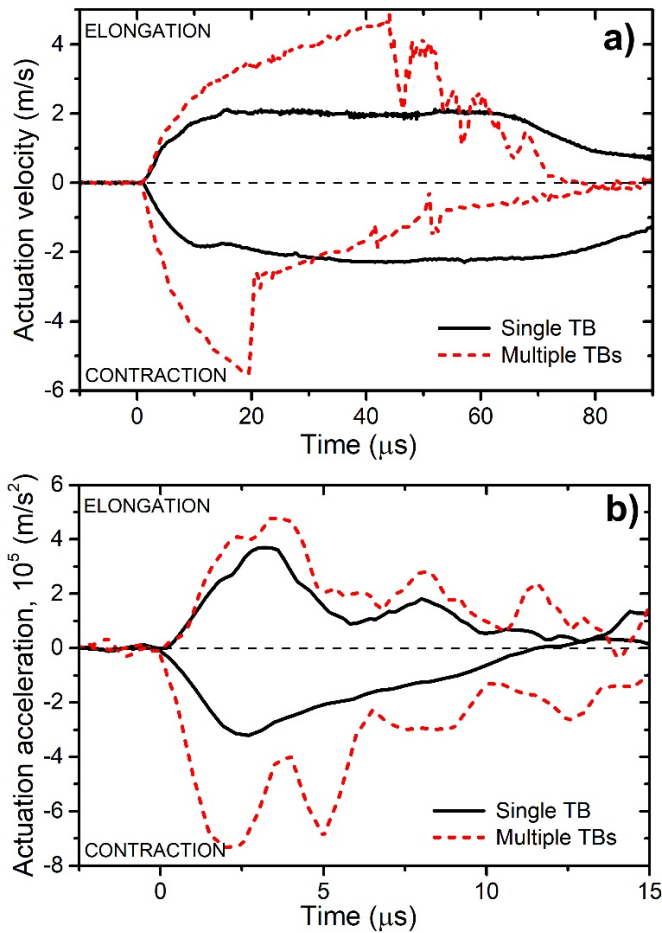


Figure 5.14: (a) LDV measurements of actuation velocity for single TB (solid lines) and multiple TBs (dashed lines) motion under pulsed magnetic field excitation. Positive values correspond to elongation mode, and negative values to contraction mode. (b) Actuation acceleration numerically derived from the velocity data presented in (a). [Publication IV]

Another feature, which is clearly observed in the actuation velocity graphs measured in the multiple TBs case, is the abrupt changes of the actuation velocity signal. These changes are obviously related to annihilation of the TBs moved towards each other. Particularly, the annihilation of the first and second TBs in contraction mode leads to the abrupt velocity change from -5.5 m/s to -2.8 m/s during 1 μs , registered at $t \sim 20$ μs . Gradual deceleration of the third TB after this moment is related to the fast current pulse decay in this particular measurement.

The TBs annihilation in elongation mode is more difficult to follow, but it is likely to occur at larger times (because of the previously discussed inertia effect) which is indeed seen in the velocity graph starting from $t \sim 45$ μs . After few pulsations, the velocity signal quickly decays at $t \sim 75$ μs before the current pulse ends, indicating that the active part of the sample was (nearly) fully converted into the field-favoured variant.

Finally, we integrated the actuation velocity curves to get the actuation displacement *versus* time. The result is shown in Figure 5.15. The saturation levels of 150 and 200 μm for multiple TBs motion (see the blue and red dashed curves) correspond to 2.5 and 3.3 mm increase of the field-favourable variant length in the sample (which is equal to the overall path of all the TBs). This corresponds to the active part lengths of the samples taking into account the initial twin variant distributions.

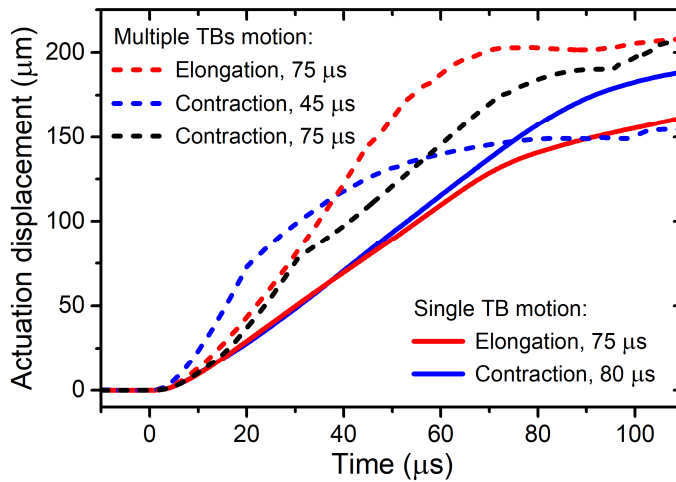


Figure 5.15: Actuation displacement for single TB (solid lines) and multiple TBs (dashed lines) motion under pulsed magnetic field excitation obtained by integration of the actuation velocity data presented in Figure 5.14(a). The black dashed line represents an additional measurement with three TBs moving in contraction mode at the field pulse length of 75 μs . The actuation pulse length is noted for each measurement. For contraction mode, the displacement sign was changed to positive.

A comparison of the actuation velocity and displacement curves leads to an important conclusion that the displacement signal does not provide sufficient information to clearly differentiate between single and multiple TBs motion. For a better comparison, in Figure 5.15 we plotted one more displacement curve (see the black dashed line) obtained for three TBs moving in contraction mode at the field pulse length of 75 μs . (The blue dashed line corresponds to the shorter current pulse of ~ 45 μs length.) It can be clearly seen from the presented curves that it would be quite difficult or even impossible to make a conclusion about the instant velocity based on these displacement curves, especially if we take into account the noise appearing in a real displacement measurement. The only reliable information one could obtain from such a measurement is the displacement onset time and an average actuation velocity, with almost no difference in the shapes of the curves for single and multiple TBs motion. Therefore, LDV-based direct actuation

velocity measurement provides a great advantage over any displacement measurement technique in characterizing the TB dynamics.

5.6 Pulsed magnetic field actuation of MSM micropillars

Scaling down to microscale is one of the most advantageous development directions in the field of MSM. Recently, we have demonstrated the MSM effect in a foil thinned down to 1 μm (Musiienko *et al.*, 2017) and in micropillars (Musiienko *et al.*, 2018), both fabricated from bulk Ni-Mn-Ga crystals. The present section demonstrates our results on fast magnetic actuation of Ni-Mn-Ga micropillars using the pulsed magnetic field actuation setup developed in this Thesis.¹¹

In the research by Musiienko *et al.* (2018), a fully reversible magnetic-field-induced strain of 6% was demonstrated in single-crystalline $\sim 50 \times 50 \times 100 \mu\text{m}^3$ cuboid micropillars fabricated from a bulk $\text{Ni}_{50}\text{Mn}_{28.5}\text{Ga}_{21.5}$ single crystal having transformation strain $\varepsilon_0=0.059$. The micropillars were manufactured by means of the Xe plasma source FIB column milling technology. After manufacturing, the micropillars were electropolished in order to remove of about 2 μm of ion-beam-damaged surface layer thus enabling actuation by a magnetic field.

Figure 5.16(a) shows a scanning electron microscopy (SEM) image of a FIB-milled MSM micropillar. The micropillar was milled at the corner of a bulk specimen, so that its top and front sides can be optically accessed. For fast actuation experiments, the micropillar was placed inside the Helmholtz coil (see description of the setup in Sections 4.4 and 4.5), and the LDV beam was focused on the top side of the micropillar, as it is shown in Figure 5.16(b). The Helmholtz coil could be rotated by 90° providing the possibility to apply a pulsed magnetic field along or perpendicularly to the micropillar. The easy c -axis in the bulk substrate was aligned with the micropillar and this state was fixed by gluing the substrate to a non-magnetic metallic holder. Application of a magnetic field in either of two perpendicular directions caused the micropillar to elongate or contract, and the motion of the pillar's top surface was monitored by the LDV.

The applied magnetic field pulse (not shown) had a full duration of 75 μs . The saturation field level ($\sim 0.65 \text{ T}$) was reached at $\sim 2 \mu\text{s}$ from the pulse start, and the saturation field region lasted approximately 55 μs .

¹¹ The experiments described in the present section were conducted by the Author of this Thesis together with M.Sc. D. Musiienko (Lappeenranta University of Technology, Finland). A manuscript based on these results has been recently submitted to *Scripta Materialia* ("Ultrafast actuation of Ni-Mn-Ga micropillars by pulsed magnetic field" by D. Musiienko, A. Saren, L. Straka, M. Vronka, J. Kopeček, O. Heczko, A. Sozinov, and K. Ullakko).

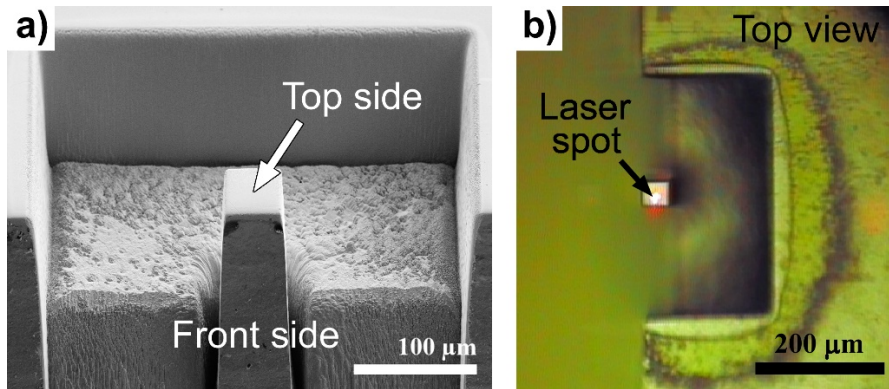


Figure 5.16: (a) SEM image of a FIB-milled MSM micropillar (Musiienko *et al.*, 2018). (b) Top view photo image of the micropillar captured with the LDV built-in camera before actuation. LDV laser beam is focused to a microspot of $\sim 1.5 \mu\text{m}$ in diameter on the top side of the pillar, with the use of an additional lens.

Prior to the pulsed actuation, the micropillar was converted into a single-variant, fully contracted state, *i.e.*, with the easy magnetization c -axis aligned along the pillar, by application of $\sim 1 \text{ T}$ magnetic field. In one series of experiments, we succeeded to introduce a single TB which can be seen in Figure 5.17(a). Thus, a second variant with a perpendicular direction of the easy axis was created in the free end of the pillar. After application of a magnetic field pulse with the field direction favouring the introduced variant, the TB moved by $\sim 60 \mu\text{m}$ inside the pillar, which caused its elongation – see Figure 5.17(b). Subsequent application of a magnetic field along the pillar caused its contraction, as it is seen in Figure 5.17(c). Note that the active part of the pillar (where the magnetic field-induced TB motion can be observed) has a length of about $100 \mu\text{m}$ which corresponds to the maximum actuation displacement of the pillar's top of $\sim 6 \mu\text{m}$.

In the second series of experiments conducted on the same micropillar, elongation and contraction occurred by motion of spontaneously generated (or residual) TBs. The optical images in polarized light taken between actuations (not shown) were similar to Figure 5.17(b) and (c).

In our experiments, we could not determine the TB type based on the presented front side images, but the LDV measurements demonstrated a distinct difference in actuation behaviour between the two series of measurements – see Figure 5.18. From these graphs, it follows that full elongation or contraction of the micropillar can occur within $\sim 25\text{-}30 \mu\text{s}$ for series 1, and within only $\sim 4\text{-}5 \mu\text{s}$ for series 2. Different maximum displacements in series 1 are explained mainly by the fact that the TB path was shorter for elongation (see Figure 5.17).

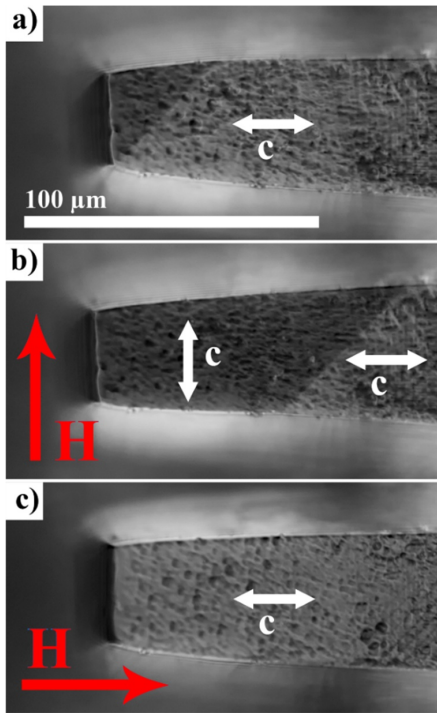


Figure 5.17: Optical micrographs of the front side of the micropillar: (a) with mechanically introduced TB, (b) fully elongated active part of the micropillar after application of the pulsed magnetic field in perpendicular direction, and (c) fully contracted micropillar after application of the pulsed magnetic field along the pillar. The contrast that differentiates the twin variants is due to the use of polarized light. The magnetic field directions are marked with the red arrows, and the easy c -axis directions with the white arrows. (Courtesy of M.Sc. D. Musiienko, published with permission.)

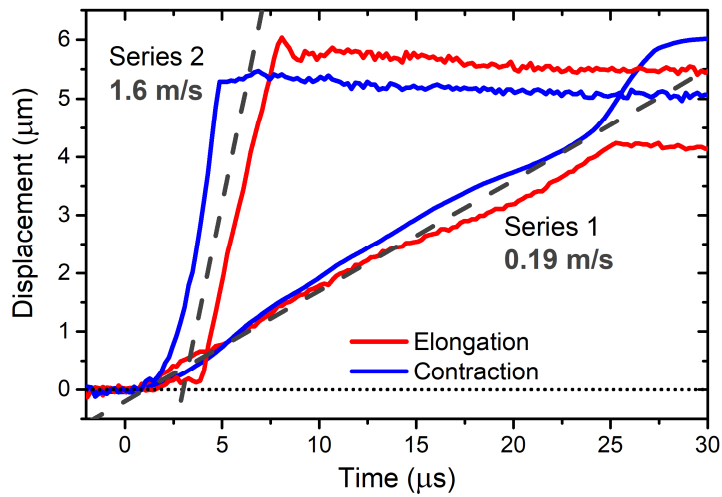


Figure 5.18: Measured displacement of the top side of the micropillar *versus* time during its elongation and contraction for two series of experiments with TB motion demonstrating different actuation speeds. The grey dashed lines are linear approximations of the growing signal, and numbers show the correspondent average velocities.

The average actuation velocities are 0.19 m/s and 1.6 m/s, for series 1 and 2, respectively (see the dashed lines in Figure 5.18). Based on this large difference in the micropillar actuation speeds in two series of measurements, we conclude that the most reasonable explanation is TB motion of different types. Namely, in series 1 we assume motion of a single TB of type 1, whereas in series 2 we see a much faster motion of type 2 TB. After recalculation of the average actuation velocities to TB velocities, we obtained 2.9 m/s and 25 m/s, for type 1 and type 2 TB velocities, correspondingly. These values are in a good agreement with previously measured data for single TB motion in bulky samples with $\sim 1 \times 1 \text{ mm}^2$ cross-sections (see Section 5.2.2). Similar dependencies we observed with another micropillar having a nearly same cross-section.

Our model suggests that we should see a pronounced scaling effect for the micropillars as compared to the millimetre-sized samples, because the micropillar's cross dimension is about 20 times smaller (see Section 3.4). We modelled the micropillar's elongation behaviour for single TB motion of both types, by numerical integration of Equation 3.3, with the parameters k_0 and α calculated according to the considered case "Elongation I" (see Section 3.3). For modelling, we assumed a cuboid shape of the pillar with cross-section of $40 \times 43 \text{ }\mu\text{m}^2$ (which corresponds to the average cross-section estimated from the SEM and optical images), and the initial twin variants configuration was chosen according to Figure 5.17(a), *i.e.*, with $L_0=0$. The time-dependent magnetic field-induced stress, σ_{mag} , was modelled from the measured current pulse, using Equations 1.1 and 1.2, with the maximum value of 3.05 MPa in saturation field. The dynamic twinning stress, σ_{res} , was modelled by a linear dependence for type 1 ($TS_1 = 2.0 + 0.4 \times v_{TB}$ [MPa]) and by a power law for type 2 ($TS_2 = 0.9 + 0.026 \times v_{TB}^{1.4}$ [MPa]). Here we used quasi-static twinning stress values close to the twinning stress measurements conducted for one of the studied micropillars.¹² The coefficients in the velocity-dependent terms were adjusted according to the average saturation velocity values, and the TB traveling distance was limited to 64 μm . The origin of the increase of the quasi-static twinning stress and the lower value of the saturation TB velocity for type 2 TBs in micropillars as compared to the bulk, is currently under investigation.

Experimental and modelled actuation velocity dependencies on time are presented in Figure 5.19 for both TB types. In the case of type 1 TB motion, large oscillations of the actuation velocity can be observed, whereas type 2 TB motion is much more stable. For type 2 TB motion, there is a clear delay of $\sim 1.8 \text{ }\mu\text{s}$ between the modelled curve and the measured signal onset. This delay can be only partially explained by the time it takes for the TB to cross the laser beam. The second reason could be some obstacles or defects on the pillar's tip for TB motion. Nevertheless, both curves demonstrate a very similar

¹² The twinning stress measurements were conducted at Institute of Physics of the Czech Academy of Sciences by M.Sc. D. Musienko (Lappeenranta University of Technology, Finland) and M.Sc. M. Vronka (Institute of Physics of the Czech Academy of Sciences, Czech Republic). The average twinning stress values were $\sim 0.8 \text{ MPa}$ for type 2 and $\sim 2.2 \text{ MPa}$ for type 1 TBs, for a particular micropillar.

behaviour as compared to single TB motion in the bulky samples (see Figure 5.7(b)), except the difference in time it takes to accelerate the TB up to the saturation speed.

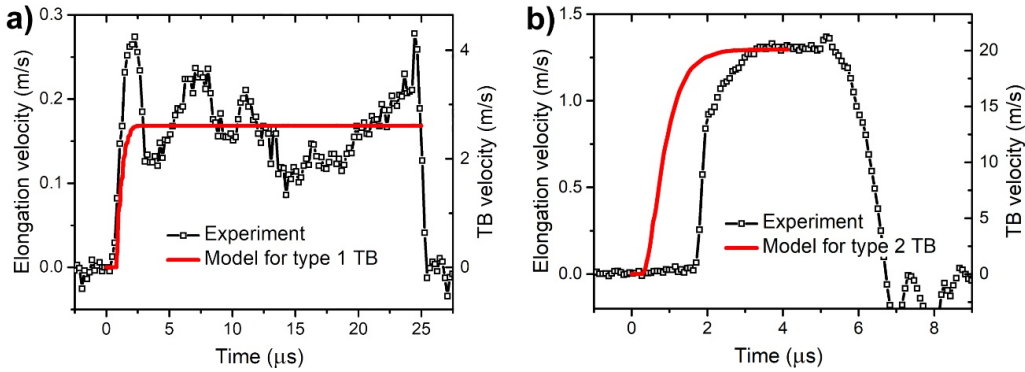


Figure 5.19: Measured and modelled elongation velocity *versus* time for type 1 (a) and type 2 (b) TB motion in the micropillar. The right axes show correspondent TB velocity scales. The dynamic twinning stress for type 1 TB was modelled as $TS_1 = 2.0 + 0.4 \times v_{TB}$ [MPa], and for type 2 – as $TS_2 = 0.9 + 0.026 \times v_{TB}^{1.4}$ [MPa]. The TB traveling distance in the model was limited to 64 μm .

To further clarify the scaling effect, we compared the above modelled velocity dependencies on time for micropillars with modelled dependencies for a sample with a cross-section of $1 \times 1 \text{ mm}^2$. In this numerical experiment, we fixed all the parameters used above for micropillars modelling, changing only the sample cross-section. The obtained graphs are presented in Figure 5.20, for the same time span of 25 μs . It can be seen, that there is no so much difference in the acceleration times for different sample sizes in the case of type 1 TB motion as compared to the used time span. But for type 2 TB motion, the acceleration times differ by about an order of magnitude, for different sample sizes. The calculated peak actuation accelerations values are 2.4×10^5 and $1.7 \times 10^6 \text{ m/s}^2$, for sample cross-section of $1 \times 1 \text{ mm}^2$ and $40 \times 43 \mu\text{m}^2$, correspondingly. Thus, the scaling leads here to an increase by ~ 7 times of the peak actuation acceleration with the decrease of the sample dimension, which leads to proportionally shorter acceleration times before the saturation velocity region.

Based on the described numerical experiment we conclude that the observed fast actuation of the micropillars is a result of both the high mobility of type 2 TBs and the scaling effect. The demonstrated actuation times of $\sim 5 \mu\text{s}$ for micropillar elongation and contraction suggest a possibility of high-frequency, of the order of 100 kHz, MSM-based microdevices actuation.

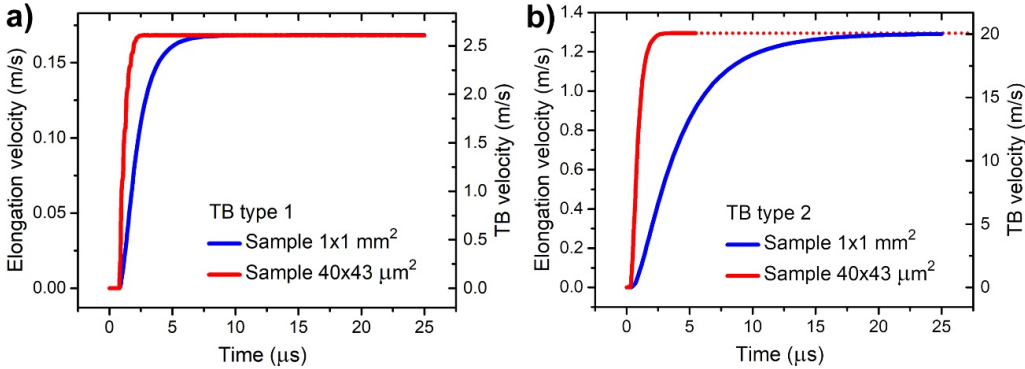


Figure 5.20: Modelled elongation velocity dependencies on time for type 1 (a) and type 2 (b) TBs, for different sample cross-sections. The right axes show correspondent TB velocity scales.

5.7 Discussion on the previous studies on twin boundary dynamics

In the present section, we compare the results obtained in this Thesis with the previous works related to TB dynamics in 5M Ni-Mn-Ga martensite. As all the previous studies dealt with average TB velocities, we will compare the existing literature data with the saturation velocity values presented in this Thesis.

5.7.1 Magnitude and limits for twin boundary velocity

The experimental results on multiple TBs motion and the analysis of the actuation displacement data, provided in Section 5.5, allows us to explain the estimated TB velocity value of 82.5 m/s, reported by Smith *et al.* (2014)¹³, by multiple TBs motion. Indeed, the only reliable result provided by the used displacement-proportional measurement technique, is the average contraction velocity of 4.6 m/s which can be achieved with just three TBs moving during a very short time, as we have shown in Section 5.5 (see Figure 5.14(a)). The TB velocity value, however, was estimated by Smith *et al.* based only on an assumption that a single TB was nucleated and moved during the actuation pulse. Thus, we assume that in their experiment few TBs moved simultaneously that has led to the observed signal, which is proportional to the volume fraction of the growing variant. This signal can be recalculated to the contraction velocity, but not directly to the TB position. As we could see from our experiments, the displacement measurement (especially taking into account the measurement noise) does not allow to distinctly conclude, was there a single TB or multiple TBs motion (see Figure 5.15).

The second, but not less important, argument is the theoretical value of a single TB velocity of 77.4 m/s obtained in the same paper by Smith *et al.* In their model, the applied force (normal stress multiplied by the sample cross-section) and the velocity of the

¹³ We refer the reader to the last paragraph in Section 1.2.3 for more details and comments on this paper.

moving variant are directed along the sample length instead of the shear direction (*i.e.*, along the TB plane – see Section 3.2). This incorrect assumption leads to an overestimation of both theoretical TB velocity and acceleration. Another mistake is the incorrect expression for the velocity of the moving mass: the authors treat it as the contraction velocity which is not equal to the velocity of the centre of mass. Finally, applying Equation 3.4 derived in this Thesis, with the magnetic field-induced stress of 3 MPa and twinning stress of 0.17 MPa used by Smith *et al.*, we obtained a value of ~ 55 m/s for the saturation TB velocity. This value is $\sim 30\%$ less than the estimated single TB velocity of ~ 80 m/s.

Earlier studies demonstrating fast sample actuation speeds up to 6 m/s (Marioni, 2003) under pulsed magnetic field actuation, can be also explained by multiple TBs motion (we demonstrated contraction speed of ~ 5.5 m/s with three TBs of type 2).

We note that the maximum velocity of ~ 40 m/s, which was observed in the present work for type 2 TBs, is related to a specific actuation mode with continuously increasing mass of the moving variant. In this case, the TB velocity is limited by the velocity-dependent twinning stress *and* inertia. Our results show that the total driving stress remains large, about 1 MPa. Theoretically, the same TB could move faster at the same magnetic driving force if the mass of the moving variant will decrease with time (see Section 3.3).

For type 1 TBs, it was shown that at the obtained maximum velocities of 3-7 m/s the total driving stress becomes small, less than 0.1 MPa. In this case, the model predicts similar saturation velocities for all actuation modes, for both increasing and decreasing mass of the moving variant.

5.7.2 Applicability of the kinetic relation approach for twin boundary dynamics

We found (see Section 5.4) that the kinetic relation approach based on a relation between the saturation (or peak) TB velocity and the driving force, is valid only for steady-state conditions and actually ignores the dynamics-related effects like inertia and velocity-dependent forces. Thus, the applicability of this approach is limited to some specific cases where the dynamics can be neglected.

Nevertheless, the obtained data can be compared with the previously published studies by Faran and Shilo (2011, 2012, 2013, 2014, and 2015) regarding TB motion in 5M Ni-Mn-Ga martensite (see Section 1.2.3 for more details on their works).

First, Faran and Shilo reported an order lower values of the TB velocities as compared to our results. It is difficult to explain such a large difference, but we can assume the following reasons. (i) The first and clear explanation could be the difference in the sample quality. Faran and Shilo reported on a big scattering of data points, and local mobility change by an order of magnitude when the TB position was shifted by only 30 μm . In contrast to that, we never observed such scattering with our samples. The TBs travelled similarly in all parts of the crystal and up to 4-5 mm paths were recorded during pulsed

actuation for type 2 TBs (0.3-0.5 mm for type 1). (ii) Faran and Shilo used “an insulating, non-constraining adapter” for the sample mounting. From our study, it follows that the sample should be rigidly fixed at some point to the adapter allowing the other part to move freely. Unfortunately, it is not clear if the sample was fixed or not in Faran and Shilo’s experiments. If not, then we can suspect that the sample could touch the adapter during actuation which uncontrollably affected the TB motion (see Section 3.6). (iii) In the experiments by Faran and Shilo, two TBs moved simultaneously under application of the magnetic field pulse. We show, however, that in such a case the TBs do not move independently and shear forces and variable-mass twin variants motion should be taken into account (see Section 3.5). (iv) Finally, inertia was neglected whereas the initial masses of the moving variants (dependent on the initial TBs positions) could affect the dynamics.

Second, our data on the saturation TB velocity *versus* magnetic driving force graphs, presented in Figure 5.11(b), clearly demonstrate the absence of any thresholds values of the driving force between 60 and 196 kJ/m³, in contrast to the data by Faran and Shilo (see Figure 1.4). The only found threshold (switching) field values correspond to the quasi-static twinning stresses. In other words, we did not find any signs of the bimodal behaviour. In addition, the dependencies for both TB types have quasi-linear trends instead of the dependence described by Equation 1.3 by Faran and Shilo. Therefore, our experimental data do not confirm the underlying physical mechanisms proposed for TB motion in their studies.

In this Thesis, we suggested and experimentally supported variable-mass model which includes velocity-dependent resistance stress or dynamic twinning stress. Physically it means that with increasing the TB velocity, the energy dissipation increases because of different mechanisms. First, we can expect non-magnetic velocity-dependent viscous-like damping mechanism related to the twinning dislocations motion. Second, both field- and velocity-dependent mechanisms connected to the magnetic subsystem, such as magnetization rotation and domain wall motion, affect the TB dynamics. In this respect, the suggested dynamic twinning stress concept allows one to probe different microscopic mechanisms by modelling and comparison with the experimentally obtained driving stress. Instead of the kinetic relation formalism, the dynamic twinning stress represents a true force acting on a moving TB and can be directly included in any dynamics equation as a force.

6 Conclusions

6.1 Contribution to the field

In this Thesis, we present new experimental and modelling approaches, and significant findings characterizing the twin boundary motion in Ni-Mn-Ga five-layered modulated martensite. The results provide an increased understanding of the material behaviour as compared to the earlier studies. The main contributions to the field can be formulated as follows.

First, a detailed characterization of single type 1 and type 2 twin boundary motion under pulsed magnetic field actuation has been performed by means of time-resolved direct velocity measurement and direct observation. This is a significant step in development of the experimental techniques in comparison with the early accessible displacement measurements and average velocity estimations. The used techniques allowed, for the first time, to precisely characterize the twin boundary dynamics in a wide range of velocities and magnetic fields.

Second, a new macroscopic model describing single twin boundary motion is presented and analysed. The model has been developed from the very basic theoretical investigations taking into account the nature of the shearing motion and variation of the twin variant's mass during the twin boundary motion. This modelling approach has been experimentally validated and allowed to adequately calculate the sample's dynamic response to a magnetic field pulse. The model permitted to extract the motion parameters from the measured velocity data, as well as to simulate the twin boundary motion at macro- and microscale. The developed concepts clearly state that the mass inertia and shear forces distribution have a crucial effect in twin boundary dynamics.

Third, the investigations have led to a novel concept which is the velocity-dependent or "dynamic" twinning stress. It is shown that the observed twin boundary velocity limitations arise from a strong dependence of twinning stress on the twin boundary velocity. These dependencies are experimentally characterized for both twin boundary types. The findings bring to the fore type 2 boundaries for applications demanding high actuation speeds and frequencies.

Finally, the presented experimental observations and concepts differ from the known "kinetic relation" approach developed in the studies by Faran and Shilo (2011, 2012, 2013, 2014, and 2015). In addition to the large quantitative differences in the measured twin boundary velocities, we demonstrated that: (i) inertia cannot be neglected, (ii) the twinning stress is dependent on the twin boundary velocity, and (iii) there are no signs of a bimodal nor a threshold-like behaviour in twin boundary motion at moderate driving forces up to saturation fields. Instead of the "kinetic relation" formalism, we suggested and experimentally supported the dynamic variable-mass model which includes dynamic twinning stress, for adequate description of the twin boundary dynamics.

Practically, the reported results demonstrate a potential for the development of new applications, especially microscale devices in which small masses of MSM elements can significantly increase the working frequency and could take full advantage of the high-speed of Ni-Mn-Ga actuation. Example applications include fast optical and electrical switches, pneumatic/hydraulic valves, microfluidic pumps and valves, micromanipulators and grippers.

6.2 Summary of the Thesis results

Based on the results presented in this Thesis and the attached original publications, the following detailed conclusions can be made:

- A new methodological approach to study twin boundary motion has been developed which permits a direct measurement of the sample actuation velocity using laser Doppler vibrometry technique. This approach allows much more precise characterization of the twin boundary motion giving reliable information on twin boundary velocity and acceleration down to sub-microsecond time-scale.
- For the first time, a direct observation of twin boundary motion under a pulsed magnetic field application was observed with a high-speed camera, with time resolution of 1.3 μs .
- A detailed characterization of single type 1 and type 2 twin boundary motion is provided. It was found that the two types exhibit substantially different dynamic properties. For type 1, the twin boundary velocity is limited to 3-7 m/s in saturation magnetic field, whereas for type 2, the twin boundary velocity can reach 33-39 m/s (at room temperature). The sample's actuation velocities of 0.2-0.4 m/s and 2-2.3 m/s were observed for single twin boundary motion of type 1 and type 2, respectively. Actuation accelerations of 0.4×10^5 and 3.7×10^5 m/s^2 have been obtained for type 1 and type 2 single twin boundary motion, respectively. The velocity onset time was measured to be of the order of 1 μs , which is the smallest reported value in the literature.
- It was experimentally revealed that primarily inertia and internal friction (such as twinning stress) affect the twin boundary dynamics. On the other hand, we demonstrated a negligible role of the field-dependent resistance forces such as magneto-static forces, torques and eddy currents, in twin boundary motion, in magnetic fields up to 2.5 T.
- A macroscopic variable-mass mathematical model has been developed which describes single twin boundary motion induced by a pulsed magnetic field. Four possible actuation modes, and effects of the sample's shape and size were analysed. The key model parameters include density and transformation strain of the alloy, initial twin boundary position, magnetic field-induced and resistance

stresses (such as twinning stress). In the case of increasing mass of the moving variant, the model predicts saturation of the twin boundary velocity under a limited magnetic driving force. Shorter acceleration times are predicted when reducing the ratio of the initial mass of the moving variant to the sample's cross-section area which is crucial for fast actuation, especially at microscale. The model was successfully applied for extraction of the driving stress from the measured data and for simulation of the experimental results at macro- and microscale, for bulk mm-sized samples and micropillars, respectively.

- We found that the observed twin boundary velocity limitations arise from a strong dependence of twinning stress on twin boundary velocity. For type 1, the twinning stress drastically increases from its quasi-static value of ~ 0.6 up to ~ 3.2 MPa, thus depleting the magnetic field-induced stress of 3.27 MPa. Type 2 boundaries show a gradual increase of twinning stress from ~ 0.1 MPa to ~ 2 MPa. This result is novel and differs from the kinetic relation approach in which the mobility coefficient is assumed as constant. The dynamic twinning stress at zero field is about twice the twinning stress in saturation field, for type 2 boundaries moving at velocities more than 5-8 m/s. This is explained by involving of additional energy dissipative mechanisms, primarily due to magnetization rotation and domain wall motion, at zero field.
- At moderate magnetic fields below saturation, which correspond to driving forces from ~ 60 to ~ 196 kJ/m³, the saturation velocity dependencies on the applied driving force obey quasi-linear trends with slopes of 2.1×10^{-4} and 4.7×10^{-5} m⁴/(J·s), for type 2 and type 1 boundaries, respectively. These observations are in agreement with the tendencies obtained at saturation fields, but an additional research is required to clarify the twinning stress behaviour at driving forces below ~ 60 kJ/m³, with the magnetic field distribution taken into account.
- Our studies on multiple twin boundary motion in saturation magnetic field $\mu_0 H > 0.7$ T show that the actuation velocity and acceleration can be increased by 2-2.5 times as compared to single twin boundary motion. The actuation velocities up to 5.5 m/s and actuation accelerations up to 7×10^5 m/s² were observed for multiple type 2 twin boundaries motion. These results point to the inertia effect and reveal that the resultant motion of the crystal cannot be reduced to a simple superposition of individual twin boundaries movements. In this case, one should take into account the shear forces acting on the twin variants and solve a system of differential equations to describe each twin variant's variable-mass motion. It is also shown that displacement measurements are insufficient to clearly differentiate between single and multiple twin boundaries motion.

- Investigation of the pulsed magnetic field actuation of MSM micropillars, having cross-sections of $\sim 50 \times 50 \mu\text{m}^2$, has been performed. Based on the experimental and modelling results, we differentiated type 1 and type 2 twin boundaries motion in the micropillars. In agreement with the model, actuation acceleration of micropillars is approximately an order of magnitude larger as compared to the bulky, mm-sized samples. This effect is caused by the different scaling of the driving force and the accelerated mass with the change of the sample size. This important result underline the perspectives of high-speed actuation at microscale. The demonstrated actuation times of $\sim 5 \mu\text{s}$ for micropillar elongation and contraction suggest a possibility of MSM-based microdevices fabrication with working frequencies of the order of 100 kHz. We conclude that the observed fast actuation of the micropillars is a result of both the high mobility of type 2 boundaries and the scaling effect.
- Based on the presented model and experimental data, we analysed the previous studies on twin boundary dynamics and conclude that the large value of twin boundary velocity of $\sim 80 \text{ m/s}$ estimated by Smith *et al.* (2014), can be explained by multiple TBs motion. Next, the main development points, which differ the presented concepts from the kinetic relation approach (Faran and Shilo, 2011, 2012, 2013, 2014, and 2015), are as follows: (i) inertia cannot be neglected, (ii) the resistance (twinning) stress is dependent on the twin boundary velocity, and (iii) there are no signs of a bimodal nor a threshold-like behaviour in twin boundary motion at magnetic driving forces between ~ 60 and $\sim 196 \text{ kJ/m}^3$. We conclude that the kinetic relation formalism can be applied only in some specific steady-state conditions because it ignores the dynamics-related effects like inertia and velocity-dependent forces.

6.3 Future work

Further investigations are required to specify more exactly the dynamic twinning stress dependencies on twin boundary velocity, in particular, by pure mechanical actuation with and without magnetic field. These experiments would shed light on the magnetic subsystem response to twin boundary motion.

The macroscopic model should be developed further in order to describe the twin boundary motion when the moving variant mass decreases with time. The next step in the model development is modelling of multiple twin boundary motion which is very important as it corresponds to the practically advantageous fine-twins samples configuration already used in prototype MSM-based devices. These twin variant configurations can be realized and studied experimentally.

The developed macroscopic model can be used as a powerful instrument for probing the twin boundary internal structure. Microscopic mechanisms, such as motion of twinning dislocations could be included into the model to simulate the velocity-dependent twinning stress and then compared with the experiment.

The presented setup based on the non-contact optical measurement approach could be completed with a temperature chamber. It is known that the twinning stress of type 1 twin boundaries has a strong temperature dependence. Therefore, variation of the temperature will allow a deeper characterization of the twin boundary dynamics. Reduction in the temperature will freeze the thermally activated processes that are involved in the twin boundary motion (such as motion of twinning dislocations or kinks). Thus, one will be able to evaluate the possible mechanisms of this motion.

References

- Aaltio I., Sozinov A., Ge Y., Ullakko K., Lindroos V.K., and Hannula S.-P., 2016. Giant Magnetostrictive Materials. In: S. Hashmi, ed.-in-chief. *Reference Module in Materials Science and Materials Engineering*. Oxford: Elsevier. pp.1-14.
- Aaltio, I., Söderberg, O., Ge, Y., Hannula, S.-P., 2010. Twin boundary nucleation and motion in Ni–Mn–Ga magnetic shape memory material with a low twinning stress. *Scripta Materialia*, 62, pp.9-12.
- Abeyaratne, R., Vedantam, S., 2003. A lattice-based model of the kinetics of twin boundary motion. *Journal of the Mechanics and Physics of Solids*, 51, pp.1675-1700.
- Chernenko, V. A., L'vov, V. A., 2008. Magnetoelastic Nature of Ferromagnetic Shape Memory Effect. *Materials Science Forum*, 583, pp.1-20.
- Chulist, R., Straka, L., Lanska, N., Soroka, A., Sozinov, A., Skrotzki, W., 2013. Characterization of mobile type I and type II twin boundaries in 10M modulated Ni–Mn–Ga martensite by electron backscatter diffraction. *Acta Materialia*, 61, pp.1913-1920.
- Glavatskaa, N.I., Rudenko, A.A., L'vov, V.A., 2002. Time-dependent magnetostrain effect and stress relaxation in the martensitic phase of Ni–Mn–Ga. *Journal of Magnetism and Magnetic Materials*, 241, pp.287-291.
- Enkovaara, J., Heczko, O., Ayuela, A., Nieminen, R.M., 2003. Coexistence of ferromagnetic and antiferromagnetic order in Mn-doped Ni₂MnGa. *Physical Review B*, 67, 212405(4pp.).
- Faran, E., Shilo, D., 2011. The kinetic relation for twin wall motion in NiMnGa. *Journal of the Mechanics and Physics of Solids*, 59, pp.975–987.
- Faran, E., Shilo, D., 2012. Implications of twinning kinetics on the frequency response in NiMnGa actuators. *Applied Physics Letters*, 100, 151901(4pp).
- Faran, E., Shilo, D., 2013. The kinetic relation for twin wall motion in NiMnGa – Part 2. *Journal of Mechanics and Physics of Solids*, 61, pp.726–741.
- Faran, E., Shilo, D., 2014. Dynamics of twin boundaries in ferromagnetic shape memory alloys. *Materials Science and Technology*, 30(13a), pp.1545-1558.
- Faran, E., Shilo, D., 2015. Multi-Scale Dynamics of Twinning in SMA. *Shape Memory and Superelasticity*, 1(2), pp.180–190.
- Heczko, O., 2010. Magnetoelastic Coupling in Ni-Mn-Ga Magnetic Shape Memory Alloy. *Materials Science Forum*, 635, pp.125-130.

- Heczko, O., Scheerbaum, N., Gutfleisch, O., 2009. Magnetic Shape Memory Phenomena. In: J.P. Liu *et al.*, eds. *Nanoscale Magnetic Materials and Applications*. New York: Springer. pp.399-439.
- Heczko, O., Kopecký, V., Sozinov, A., Straka, L., 2013a. Magnetic shape memory effect at 1.7 K. *Applied Physics Letters*, 103, 072405(4pp.).
- Heczko, O., Straka, L., Seiner, H., 2013b. Different microstructures of mobile twin boundaries in 10 M modulated Ni–Mn–Ga martensite. *Acta Materialia*, 61, pp.622-631.
- Heczko, O., Kopecký, V., Fekete, L., Jurek, K., Kopeček, J., Straka, L., Seiner, H., 2015. Magnetic Domains and Twin Microstructure of Single Crystal Ni–Mn–Ga Exhibiting Magnetic Shape Memory Effect. *IEEE Transactions on Magnetics*, 51(11), 2505304.
- Heczko, O., Vokoun, D., Kopecký, V., Beleggia, M., 2015. Effect of Magnetostatic Interactions on Twin Boundary Motion in Ni–Mn–Ga Magnetic Shape Memory Alloy. *IEEE Magnetic Letters*, 6, 1000204(4pp.).
- Henry, C.P., Feuchtwanger, J., Bono, D., Marioni, M., Tello, P.G., Richard, M., Allen, S.M., O’Handley, R.C., 2001. AC performance and modeling of ferromagnetic shape memory actuators. In: C.S. Lynch, ed. *Smart Structures and Materials 2001: Active Materials: Behavior and Mechanics, Proceedings of SPIE*, 4333, pp.151-162.
- Henry, C.P., Tello, P.G., Bono, D., Hong, J., Wager, R., Dai, J., Allen, S.M., O’Handley, R.C., 2003. Frequency response of single-crystal Ni–Mn–Ga FSMAs. In: D.C. Lagoudas, ed. *Smart Structures and Materials 2003: Active Materials: Behavior and Mechanics, Proceedings of SPIE*, 5053, pp.207-211.
- James, R.D., Tickle, R., Wuttig, M., 1999. Large field-induced strains in ferromagnetic shape memory materials. *Materials Science and Engineering*, A273–275, pp.320-325.
- Kaufmann, S., Rößler, U.K., Heczko, O., Wuttig, M., Buschbeck, J., Schultz, L., Fähler, S., 2010. Adaptive modulations of martensites. *Physical Review Letters*, 104(14), pp.145702(4pp.).
- Kelly, A., Groves, G.W., Kidd, P. (2000). *Crystallography and Crystal Defects*. Chichester: John Wiley & Sons.
- Korpiola, K., Sozinov, A., Niskanen, A., Perento, J., 2013. NiMnGa MSM Element Deformation Velocity on Pulsed and Saturated Magnetic Field. *Proceedings on the 4th International Conference on Ferromagnetic Shape Memory Alloys ICFMSA-2013*, Boise State University, Idaho, USA, pp.14-15.

- Lai, Y.-W., 2009. Magnetic Microstructure and Actuation Dynamics of NiMnGa Magnetic Shape Memory Materials. Ph.D. thesis, Technische Universität Dresden, Dresden.
- Lai, Y.-W., Schäfer, R., Schultz, L., McCord, J., 2008. Direct observation of AC field-induced twin-boundary dynamics in bulk NiMnGa. *Acta Materialia*, 56, pp.5130-5137.
- Lázpita, P., Barandiarán, J.M., Gutiérrez, J., Feuchtwanger, J., Chernenko, V.A., Richard, M.L., 2011. Magnetic moment and chemical order in off-stoichiometric Ni–Mn–Ga ferromagnetic shape memory alloys. *New Journal of Physics*, 13, 033039(14pp.).
- Likhachev, A.A., Sozinov, A., Ullakko, K., 2006. Modeling the strain response, magneto-mechanical cycling under the external stress, work output and energy losses in Ni–Mn–Ga. *Mechanics of Materials*, 38, pp.551-563.
- Likhachev, A. A., Ullakko, K., 1999. Quantitative Model of Large Magnetostrain Effect in Ferromagnetic Shape Memory Alloys. *EPJ direct B2*, pp.1-9.
- Likhachev, A.A., Ullakko, K., 2000. Magnetic-field-controlled twin boundaries motion and giant magneto-mechanical effects in Ni–Mn–Ga shape memory alloy. *Physics Letters A*, 275, pp.142-151.
- Marioni, M.A., 2003. Pulsed Magnetic Field-Induced Twin Boundary Motion in Ni-Mn-Ga. Ph.D. thesis, M.I.T., Cambridge, MA.
- Marioni, M.A., Allen, S.M., O’Handley, R.C., 2004. Nonuniform twin-boundary motion in Ni–Mn–Ga single crystals. *Applied Physics Letters*, 84(20), pp.4071-4073.
- Marioni, M., Bono, D., Banful, A.B., del Rosario, M., Rodriguez, E., Peterson, B.W., Allen, S.M., O’Handley, R.C., 2003a. Pulsed field actuation of Ni-Mn-Ga ferromagnetic shape memory alloy single crystal. *Journal de Physique IV France*, 112, pp.1001-1003.
- Marioni, M.A., Bono, D.C., O’Handley, R.C., Allen, S.M., 2002. Pulsed magnetic field actuation of single-crystalline ferromagnetic shape memory alloy Ni–Mn–Ga. *Smart Structures and Materials 2002: Active Materials: Behavior and Mechanics, Proceedings of SPIE*, 4699, pp.191-194.
- Marioni, M.A., O’Handley, R.C., Allen, S.M., 2003b. Pulsed magnetic field-induced actuation of Ni–Mn–Ga single crystals. *Applied Physics Letters*, 83(19), pp.3966-3968.
- Martynov, V., Kokorin, V., 1992. The crystal structure of thermally- and stress-induced Martensites in Ni₂MnGa single crystals. *Journal de Physique III*, 2(5), pp.739-749.

- Murray, S.J., Marioni, M., Allen, S.M., O'Handley, R.C., 2000. 6% magnetic-field-induced strain by twin boundary motion in ferromagnetic Ni–Mn–Ga. *Applied Physics Letters*, 77, pp.886-888.
- Musiienko, D., Saren, A., Ullakko, K., 2017. Magnetic shape memory effect in single crystalline Ni-Mn-Ga foil thinned down to 1 μm . *Scripta Materialia*, 139, pp.152-154.
- Musiienko, D., Straka, L., Klimša, L., Saren, A., Sozinov, A., Heczko, O., Ullakko, K., 2018. Giant magnetic-field-induced strain in Ni-Mn-Ga micropillars. *Scripta Materialia*, 150, pp.173-176.
- Müllner, P., Chernenko, V.A., Kosterz, G., 2003. A microscopic approach to the magnetic-field-induced deformation of martensite (magnetoplasticity). *Journal of Magnetism and Magnetic Materials*, 267, pp.325-334.
- O'Handley, R.C., 1998. Model for strain and magnetization in magnetic shape-memory alloys. *Journal of Applied Physics*, 83(6), pp.3263-3270.
- O'Handley, R.C., Allen, S.M., Paul, D.I., Henry, C.P., Marioni, M., Bono, D., Jenkins, C., Banful, A., Wager, R., 2003. Magnetic field-induced strain in single crystal Ni-Mn-Ga. In: D.C. Lagoudas, ed. *Smart Structures and Materials 2003: Active Materials: Behavior and Mechanics, Proceedings of SPIE*, 5053, pp.200-206.
- O'Handley, R. C., Murray, S. J., Marioni, M., Nembach, H., Allen, S. M., 2000. Phenomenology of giant magnetic-field-induced strain in ferromagnetic shape-memory materials (invited). *Journal of Applied Physics*, 87(9), pp.4712-4717.
- Paul, D.I., McGehee, W., O'Handley, R.C., Richard, M., 2007. Ferromagnetic shape memory alloys: A theoretical approach. *Journal of Applied Physics*, 101, 123917(9pp.).
- Pons, J., Santamarta, R., Chernenko, V.A., Cesari, E., 2005. Long-period martensitic structures of Ni–Mn–Ga alloys studied by high-resolution transmission electron microscopy. *Journal of Applied Physics*, 97, 083516(7pp.).
- Seiner, H., Straka, L., Heczko, O., 2014. A microstructural model of motion of macro-twin interfaces in Ni–Mn–Ga 10M martensite. *Journal of the Mechanics and Physics of Solids*, 64, pp.198–211.
- Smith, A.R., Tellinen, J., Ullakko, K., 2014. Rapid actuation and response of Ni–Mn–Ga to magnetic field-induced stress. *Acta Materialia*, 80, pp.373–379.
- Sommerfeld, A. (1959). *Lectures on Theoretical Physics, Mechanics, vol. I*. 2nd Printing. New York: Academic Press.

- Sozinov, A., Lanska, N., Soroka, A., Straka, L., 2011. Highly mobile type II twin boundary in Ni–Mn–Ga five-layered martensite. *Applied Physics Letters*, 99, 124103.
- Sozinov, A., Lanska, N., Soroka, A., Zou, W., 2013. 12% Magnetic field-induced strain in Ni–Mn–Ga-based non-modulated martensite. *Applied Physics Letters*, 102(2), 021902.
- Sozinov, A., Likhachev, A.A., Lanska, N., Ullakko, K., 2002. Giant magnetic-field-induced strain in NiMnGa seven-layered martensitic phase. *Applied Physics Letters*, 80(10), pp.1746-1748.
- Straka, L., Heczko, O., Seiner, H., Lanska, N., Drahokoupil, J., Soroka, A., Fähler, S., Hänninen, H., Sozinov A., 2011. Highly mobile twinned interface in 10 M modulated Ni–Mn–Ga martensite. *Acta Materialia*, 59, pp.7450-7463.
- Straka, L., Soroka, A., Seiner, H., Hänninen, H., Sozinov, A., 2012. Temperature dependence of twinning stress of type I and type II twins in 10 M modulated Ni–Mn–Ga martensite. *Scripta Materialia*, 67, pp.25-28.
- Straka, L., Sozinov, A., Drahokoupil, J., Kopecký, V., Hänninen, H., Heczko, O., 2013. Effect of intermartensite transformation on twinning stress in Ni-Mn-Ga 10M martensite. *Journal of Applied Physics*, 114, 063504.
- Suorsa, I., Pagounis, E., Ullakko, K., 2004. Magnetic shape memory actuator performance. *Journal of Magnetism and Magnetic Materials*, 272–276, pp.2029–2030.
- Söderberg, O., Sozinov, A., Ge, Y., Hannula, S.P., Lindroos, V.K., 2006. Giant magnetostrictive materials. In: Buschow, K.H.J. (Ed.), *Handbook of Magnetic Materials*. Amsterdam: Elsevier Science. Vol.16, pp. 1–39.
- Tellinen, J., Suorsa, I., Jääskeläinen, A., Aaltio, I., Ullakko, K., 2002. Basic properties of magnetic shape memory actuators. In: Borgmann, H. (Ed.), *Proceedings of 8th International Conference on New Actuators, Actuator 2002*. Bremen: Messe Bremen GmbH, pp. 566–569.
- Ullakko, K., 1996. Magnetically Controlled Shape Memory Alloys: A New Class of Actuator Materials. *Journal of Materials Engineering and Performance*, 5(3), pp.405-409.
- Ullakko, K., Huang, J.K., Kantner, C., O'Handley, R.C., Kokorin, V.V., 1996. Large magnetic-field-induced strains in Ni₂MnGa single crystals. *Applied Physics Letters*, 69(13), pp.1966-1968.
- Ullakko, K., Smith, A., Berhardt, E., Tellinen, J., 2013. Speed of twin boundaries, frequency response and work output of small Ni-Mn-Ga samples. *Proceedings on the*

4th International Conference on Ferromagnetic Shape Memory Alloys ICFSMA-2013, Boise State University, Idaho, USA, pp.16-17.

Webster, P.J., Ziebeck, K.R.A., Town, S.L., Peak, M.S., 1984. Magnetic order and phase transformation in Ni₂MnGa alloy. *Philosophical Magazine B: Physics of Condensed Matter: Statistical Mechanics, Electronic, Optical and Magnetic Properties*. 49, pp.295–310.

Xu, X., Nagasako, M., Ito, W., Umetsu, R.Y., Kanomata, T., Kainuma, R., 2013. Magnetic properties and phase diagram of Ni₅₀Mn_{50-x}Ga_x ferromagnetic shape memory alloys. *Acta Materialia*, 61, pp.6712–6723.

Zreihan, N., Faran, E., Shilo, D., 2018. The effect of loading rate on characteristics of type II twin boundary motion in Ni-Mn-Ga. *Scripta Materialia*, 144, pp.44-47.

Appendix A: Electrical circuit for pulsed magnetic field actuation setup

In this chapter we describe the passive electrical circuit developed for the pulsed magnetic field actuation setups presented in Sections 4.4 and 4.5. The purpose of this circuit is to provide close to square pulse shape with short rise and fall times at different current amplitudes and different pulse lengths.¹⁴

Figure A.1 represents a circuit diagram developed in the LTspice® simulation software. The left part, named “Pulse generator output circuit”, depicts the internal discharge circuit found in the used pulse generator (EMC, Transient 1000). The right part, “Load”, represents a solenoid or Helmholtz coil used as the magnetic field source in the experiments. The central part includes the passive circuit elements.

During the discharge of the capacitor C1, the chain C2-R3 and the coil L2 connected in parallel define the basic pulse shape having a short rise time and flattened peak. The pulse length is defined mostly by the inductance L2 when $L_3 \ll L_2$. The diode D1 cuts the decaying part of the pulse providing a short fall time. The wire resistor R4 serves for the current measurement based on the voltage drop on the resistor. The second diode, D2, cuts off the negative pulsations.

First, we used the LTspice® simulator for the initial adjustment of the passive circuit parameters C2, R3 and L2 (including both inductance and resistance) using the measured values of the load inductance, L, and resistance R (for the 16.3 mm solenoid, $L=22.8 \mu\text{H}$ and $R=1.23 \text{ Ohm @ } 1 \text{ kHz}$; for the Helmholtz coil, $L=13 \mu\text{H}$ and $R=0.75 \text{ Ohm @ } 5 \text{ kHz}$). Then, the final adjustment of these parameters was done experimentally.

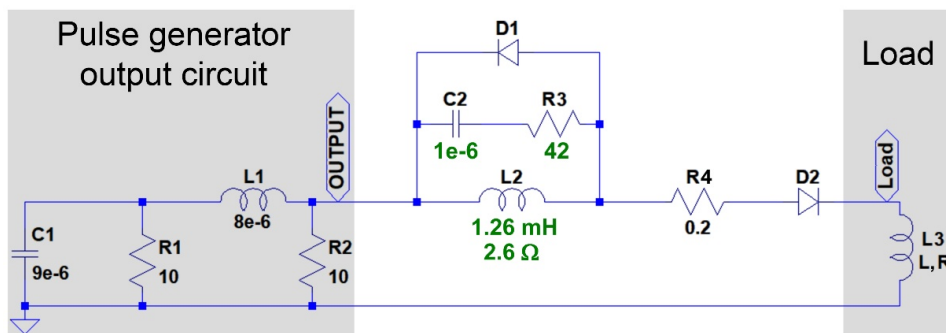


Figure A.1: Circuit diagram used for simulation in LTspice® software. The capacitor C1 can be charged to 250-4000 V. The set of adjustable passive circuit parameters marked by green allows generation of pulses with a length of $\sim 110\text{-}120 \mu\text{s}$.

¹⁴ The original idea of the circuit design belongs to Dr. Juhani Tellinen.

Figure A.2 shows the measured current pulses obtained with two different sets of the adjustable parameters C_2 , R_3 and L_2 , and the Helmholtz coil as a load. It is seen that the pulse shape is close to a square and the rise time is about $2.5 \mu\text{s}$ for the longer pulses and $\sim 5 \mu\text{s}$ for the shorter ones. The fall time is $15\text{-}20 \mu\text{s}$ in both cases. The current amplitude ranges from 5.5 A to 80 A for the longer pulses, and from 17 A to 270 A for the shorter ones.

The pulse shape can be widely changed by modification of the passive circuit parameters. For example, a pulse shape close to semi-sinusoidal is achieved when excluding the elements D_1 , C_2 and R_3 from the passive circuit.

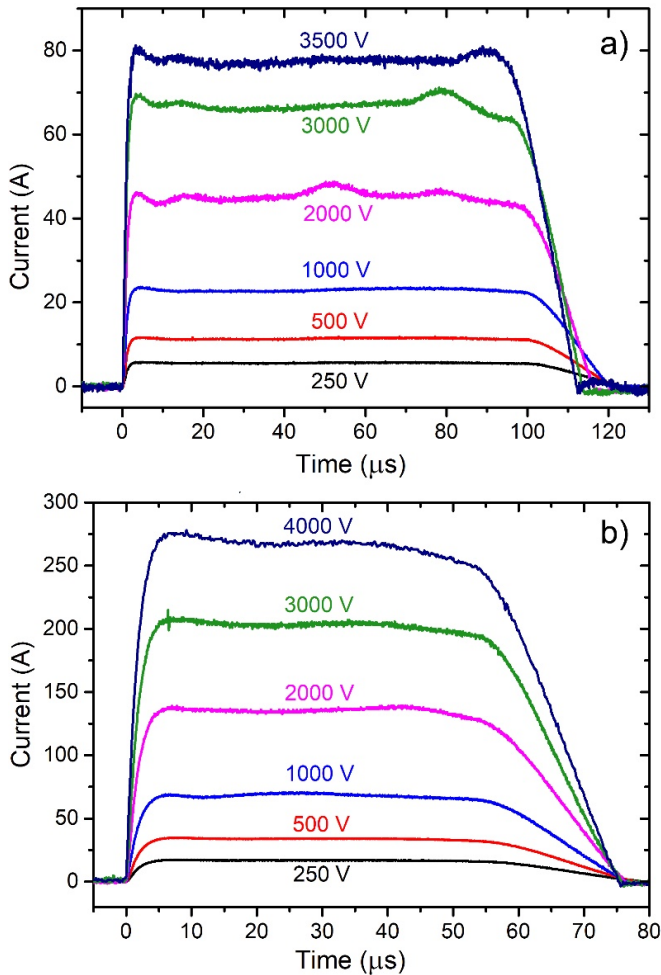


Figure A.2: Current pulses of two different lengths obtained at different charge voltages of the capacitor C_1 (see Figure A.1). (a) Pulses of $\sim 110\text{-}120 \mu\text{s}$ length obtained with the passive circuit parameters shown in Figure A.1. (b) Pulses of $\sim 75 \mu\text{s}$ length obtained with the following parameters: $C_2 = 1.7 \mu\text{F}$, $R_3 = 12 \text{ Ohm}$, and for L_2 , the inductance and resistance were 0.22 mH and 0.87 Ohm , respectively.

Appendix B: MATLAB code example for the model

The present chapter contains an example code written in MATLAB R2017a which implements a numerical solution of Equation 3.3 obtained for the case a of single TB motion with increasing mass of the moving variant. For convenience, the code is divided into three scripts named *Main.m*, *Load_Current.m*, and a function *EqSolver1.m*.

In the present example, a single TB motion of type 1 under a pulsed magnetic field is modelled, with the field calculated from the measured coil current. The temporal current dependence is loaded from a text file in the script *Load_Current.m*. The file contains two columns: time[microseconds] and current[amperes]. The field is calculated for the 16.3 mm solenoid and the magnetic field-induced stress is calculated using Equations 1.1 and 1.2. The dynamic twinning stress is modelled by a linear dependence (see Section 5.3).

Main.m:

```
%Material properties
Ro=8000;           %Volumetric mass density, kg/m^3
Eps0=0.06;        %Transformation strain
Ku=196000;        %Anisotropy constant, J/m^3
Ms=0.7;           %Saturation magnetization, T

%Calculated parameters
Alpha=atan(1-Eps0);
Beta=pi/2-2*Alpha;
k0=cos(Alpha)+sin(Alpha)/tan(Beta);
Ha=2*Ku/Ms;       %Anisotropy field, A/m

%TB properties
StaticTS=0.6E6;  %Quasi-static twinning stress value, Pa

%Sample geometry and initial TB configuration
A0=0.946E-6;     %Sample's cross-section, m^2 (on the right side)
H0=0.86E-3;     %Sample's height, m (on the right side)
L0=0.1E-3;      %Initial twin boundary position, m
m0=Ro*A0*(L0+H0/2/(1-Eps0)); %Initial mass, kg

%Load current curve from a text file and calculate Sigma_mag(t) matrix,
%i.e. magnetic field-induced stress vs time
dir_name = 'PATH/'; %File path
fn_current = 'FILENAME.txt'; %File name
Load_Current;

%Solve differential equation - function call
C1=k0*cos(Alpha)/Ro; %Parameter C1
C2=m0/Ro/A0-L0;     %Parameter C2
[t,y] = EqSolver1(C1,C2,dt,t_ST,t_FN,N0,L0,StaticTS,SMPulse);

%Plot velocity graph
figure;
plot(t,y(:,2),'-o');
xlabel('Time, s');
ylabel('TB velocity, m/s');
```

Load_Current.m:

```
%Reads current pulse from a text file and calculates magnetic field-induced stress
```

```

%The file name fn_current should be predefined in the calling script
fprintf('Loading current pulse from file '%s'...\n',fn_current);
CPulse = dlmread(strcat(dir_name,fn_current)); %Load file into matrix
N=length(CPulse); %Number of data points in the file
dt=CPulse(2,1)-CPulse(1,1); %Time step in microseconds
N0=ceil(-CPulse(1,1)/dt); %Point# where time=0
dt=dt*1E-6; %Time step in seconds
%Time scaling (microseconds to seconds)
CPulse(:,1)=CPulse(:,1)*1E-6;
%H-field [A/m] calculation for 16.3 mm solenoid using the same matrix
CPulse(:,2)=CPulse(:,2)*8240;
%Sigma_mag array calculation using the model parameters Ms, Ha and Ku
SMPulse=zeros(size(CPulse)); %Creating a new matrix for Sigma_mag
SMPulse(:,1)=CPulse(:,1); %Copying the time column
for i = 1:N %Magnetic stress calculation
    if CPulse(i,2)<0
        SMPulse(i,2)=0; %Put zero stress if a negative value occurs
    elseif CPulse(i,2)>Ha
        SMPulse(i,2)=Ku/Eps0; %Saturated magnetic stress if H>Ha
    else
        %Calculation of the average anizotropy energy
        h=CPulse(i,2)*Ms/2/Ku; %Parameter in formula
        SMPulse(i,2)=Ku*(2*h-h^2); %Average energy calculation (for homogeneous field)
        SMPulse(i,2)=SMPulse(i,2)/Eps0; %Magnetic field-induced stress calculation
    end
end
%Determination of the starting integration time
%Search for the threshold magnetic stress which is larger than the quasi-static TS
t_ST=SMPulse(N,1);
for i=N0:N
    if SMPulse(i,2)>StaticTS
        t_ST=SMPulse(i,1);
        break;
    end
end
%Determination of the maximum integration time
t_FN=SMPulse(N,1);

```

EqSolver1.m:

```

function [ t, y ] = EqSolver1(C1,C2,dt,t_ST,t_FN,N0,L0,StaticTS,SMPulse)
%Solves the differential equation for single TB motion

options = odeset('RelTol',1e-4,'Stats','on','OutputFcn',@odeplot);
[t,y] = ode45(@eq1, [t_ST t_FN], [L0; 0], options);

function dydt = eq1(t,y)
%Differential equation is presented as two 1st-order equations:
% 1). y(1)' = y(2)
% 2). y(2)' = (f(t,y(2))-y(2)^2) / (C0+y(1))
%where y(1)=L and y(2)=dL/dt, i.e. TB position and TB velocity
dydt=[y(2); (C1*(Smag(t)-Sres(y(2)))-y(2)^2)/(C2+y(1))];
end

function SM = Smag(t)
%Returns magnetic field-induced stress for the time t
SM=SMPulse(round(t/dt)+N0,2);
end

function SR = Sres(v)
%Returns resistance (dynamic twinning) stress for TB velocity v
SR=(StaticTS+0.6E6*abs(v))*sign(v);
end

end

```

Publication I

Saren, A., Musiienko, D., Smith, A.R., Ullakko, K.

Pulsed magnetic field-induced single twin boundary motion in Ni–Mn–Ga 5M martensite: A laser vibrometry characterization

Reprinted with permission from

Scripta Materialia

Vol. 113, pp. 154-157, 2016

© 2015, Elsevier Ltd.



Regular Article

Pulsed magnetic field-induced single twin boundary motion in Ni–Mn–Ga 5M martensite: A laser vibrometry characterization



A. Saren, D. Musiienko, A.R. Smith, K. Ullakko *

Material Physics Laboratory, Lappeenranta University of Technology, Lahtiakallio 3, 57170 Savonlinna, Finland

ARTICLE INFO

Article history:

Received 18 September 2015
 Received in revised form 7 October 2015
 Accepted 8 October 2015
 Available online xxxx

Keywords:

Ferromagnetic shape memory alloy
 Magnetic shape memory
 Twinning
 Twin boundary
 Ni–Mn–Ga

ABSTRACT

Pulsed magnetic field-induced motion of single twin boundaries in Ni–Mn–Ga 5M martensite has been studied using laser vibrometry technique. Maximum actuation velocities of 0.25 m/s for Type I and 2 m/s for Type II twin boundary motion were directly observed, which corresponds to velocities of 4.2 m/s and 33 m/s for these types of twin boundaries moving inside the crystal. Actuation response time of 2 μ s and actuating acceleration of about 2×10^5 m/s² for Type II boundary were achieved. The difference between Type I and Type II boundaries and the limiting role of inertia in twin boundary motion are discussed.

© 2015 Elsevier Ltd. All rights reserved.

Twin boundary movement caused by an internal magnetic-field-induced stress is the mechanism responsible for the large, reversible strains in the magnetic shape memory (MSM) alloy Ni–Mn–Ga [1]. This primary property makes Ni–Mn–Ga an attractive material for use as an actuator. Hence, deeper understanding of the dynamics of the field-induced twin boundary motion and the limits to the speed at which it can occur would enable the development of applications that could take full advantage of the material's properties.

The previous research on twin boundary kinetics in Ni–Mn–Ga under a magnetic field excitation was performed using AC field-induced strain measurement under load [2] and a pulsed magnetic field excitation [3–5] with a pulse duration in a sub-millisecond range. These approaches using different displacement measurement techniques allowed only an estimation for the averaged actuation velocity for the whole sample with uncontrolled twin boundary configuration, i.e. with multiple twin boundary initiation and propagation. The actuation response times lie in the range of 40–200 μ s. Based on model calculations, a conclusion was made that the mass inertia is the most important factor limiting the onset of the extension in the pulsed actuation [5]. In addition, it was noted that the effect of inertia depends on the position and number of mobile twin boundaries. Reported values for maximum actuation velocity and acceleration achieved at saturation driving force are 6 m/s and 50 m/s² respectively [5].

Stroboscopic imaging technique under AC excitation up to 600 Hz [6] was used to investigate the motion of individual twin boundaries

including averaged velocity calculation based on the changes in twin variant width during cycling. The maximum velocity observed was 0.21 m/s. The data implies that twin boundary velocity is not the limiting factor of the actuation performance.

In the recent studies using pulsed magnetic field [7–9], the velocity of single twin boundaries of Type I and Type II was measured to be of the order of 1–2 m/s in fields below 0.3 T. In these studies, one band of the second variant was introduced into the single variant sample and photo images were taken before and after the pulse. Average velocity evaluation of the individual twin boundaries was performed based on the measurements of the distance that individual interfaces pass due to the application of a magnetic field pulse. An assumption was made that the average velocity is approximately equal to the instantaneous velocity under the driving force value of the pulse amplitude. The authors assumed that the effect of inertia is negligible.

At the same time, some previous works indicate the possibility of rapid actuation of the sample when actual twin boundary pattern (consistently typically of multiple interfaces) was uncontrollable [5,10,11]. Actuation velocities of the order of few m/s were achieved (for example, 6 m/s in [5]). This implies that the maximum speed of individual twin boundaries should represent a noticeable part of this value (taking into account the maximum transformation strain).

Summarizing the abovementioned results, it can be concluded that (1) direct velocity measurements are necessary for precisely characterizing the twin boundary dynamics. (2) To avoid additional inertia effects, an optical velocity measurement technique should be used instead of any measurement device attached directly to the sample. (3) In order to observe the maximum velocities of individual twin boundaries one needs to reach magnetization saturation inside the

* Corresponding author.

E-mail address: Kari.Ullakko@lut.fi (K. Ullakko).

sample and have enough long actuation pulse to fully accelerate the mass behind the moving twin boundary.

In this study, we used a laser Doppler vibrometry (LDV) technique to measure the actuating velocity of a Ni–Mn–Ga sample that contained a single twin boundary when it was subjected to a pulsed magnetic field. The difference between Type I and Type II twin boundary motion was observed and it is discussed. Actuation response time and actuating acceleration are also considered based on the experimental results. The important role of the mass inertia during the twin boundary motion is also discussed.

The samples used in this study were cut from $\text{Ni}_{50}\text{Mn}_{28}\text{Ga}_{22}$ single crystals with austenite start temperature of 42 °C. The room temperature structure of the samples is 5M martensite. All faces of the samples are nearly parallel to the {1 0 0} planes of the austenite. The samples' cross-section is $1 \times 1 \text{ mm}^2$ and the length vary from 6 to 10 mm. Mechanical polishing and a few electropolishing steps provided low twinning stresses of 0.55 and 0.08 MPa for Type I and Type II single twin boundaries, respectively. The maximum strain was measured to be 6%. A solenoid connected to a high-voltage pulse generator (EMC, Transient 1000) was used to generate a pulsed magnetic field inside the sample. The solenoid had an inner diameter of 3.15 mm, a length of 6.7 mm, and consisted of 60 turns in 2 layers of insulated copper wire of 0.2 mm in diameter. The resistance of the coil was measured to be 0.51 Ω and the inductance 6 μH . Additional coils and/or resistors connected in series with the solenoid allowed generation of current pulses with duration times of 50–100 μs . The actuation velocity was measured using a laser vibrometer (Polytec, OFV-5000, OFV-534). A data acquisition board (National Instruments, USB-6361) connected to PC and triggered from the pulse generator was used to digitize the measured velocity signal. The pulse voltage and current curves were recorded by a 200 MHz oscilloscope (Metrix Scopix III OX 7204). The measurement setup is capable to measure transient velocities up to 10 m/s with time resolution of 0.5 μs . The laser head, solenoid and sample holder were mounted on a vibration isolation platform (VIBRAPLANE 2210, Kinetic Systems, Inc.) to exclude mechanical noises from the surroundings. For each pulse, the data including actuation velocity, pulse voltage and current were recorded and transferred to a PC for subsequent analysis. All measurements were performed at room temperature.

Fig. 1 shows the schematic of the LDV experimental setup for pulsed MSM actuation explaining the arrangement of the laser head, solenoid, sample holder and the sample. The sample was glued on one side (the right side in the figure) with an epoxy to the plastic holder, which enabled rigid mounting to the solenoid holder, so that the unglued end of the sample could be placed inside the solenoid. It was revealed that strong mounting of the sample is essential, because the torque applied by the field to the magnetic moments transfers to the mass of the crystal. This in turn would cause the sample, to swing at its free end, causing artifacts. In spite of the strong sample mounting, slight motion is visible in the measured velocity curves.

Prior to each measurement, the sample was set into a single variant state by applying a 1 T magnetic field along the axis of its shortest dimension, which fully elongated the sample. Further, by means of a mechanical stress, the very corner of the sample was converted to the second variant in which the shortest c -axis (equal to the easy axis of magnetization) was aligned along its length. Thus, a single twin

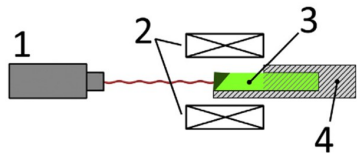


Fig. 1. Schematic of the experimental setup. (1) LDV laser head, (2) solenoid, (3) MSM sample, (4) sample holder.

boundary was created near the free unglued end. Before and after each pulse, the crystal was photographed in a polarized light, to reveal the traveling distance of the twin boundary. The type of the twin boundary was identified according to the difference in the projections on (1 0 0) plane (here applicable for the top side of the sample): Type I twin boundary exhibits nearly parallel projection relative to the crystal's edges while that of Type II twin boundary is inclined by about 6° [12].

Fig. 2 shows the optical images taken from the MSM sample before (a and b) and after (c) the magnetic field pulse exposition. The twin boundary was identified to be of Type II. During the pulse, the boundary traveled a distance of $2.01 \pm 0.05 \text{ mm}$, as it was calculated from the top view images. The driving force for this motion arises from the energy difference of the twin variants with different orientations of easy axis in respect to the magnetic field direction. In the present case, the left variant in Fig. 2 is growing at the expense of the right one having its easy axis perpendicular to the external field direction, and the boundary moves to the right. Consequently, contraction of the sample occurs along [1 0 0] direction of the crystal since the lengths of the martensitic crystallographic axes are different. Thus, the actuation velocity of the free end of the sample measured by the laser vibrometer, is directly proportional to the twin boundary velocity with a coefficient equal to the maximum strain of the sample.

Fig. 3 shows the measured time dependencies of the actuation velocity for the twin boundaries of both types along with a current–time curve. The calculated maximum magnetic field strength for the pulse is 900 kA/m and the magnetic induction is 1.8 T. The driving force for the twin boundary motion is the magnetic field induced stress, which causes the reorientation of the twin variants [1].

From the actuation velocity data, it can be clearly seen that the process involves three parts: acceleration, a constant velocity region and deceleration. First, during the beginning of the actuation pulse, the motion starts when the magnetic field induced stress is high enough to overcome the twinning stress. As the motion of the twin boundary

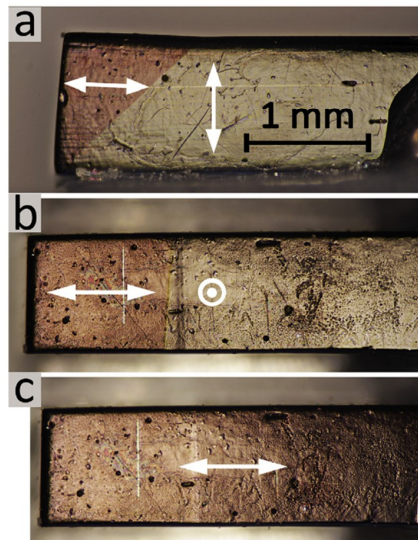


Fig. 2. Optical images of the sample with a single twin boundary of Type II. (a) Side view before the pulse, (b) top view before the pulse, (c) top view after the pulse. The color contrast that differentiates the twin variants is due to the use of polarizing filters. White arrows show the orientation of the easy axis inside the twin variants. (For interpretation of the references to color in this figure legend, the reader is referred to the web version of this article.)

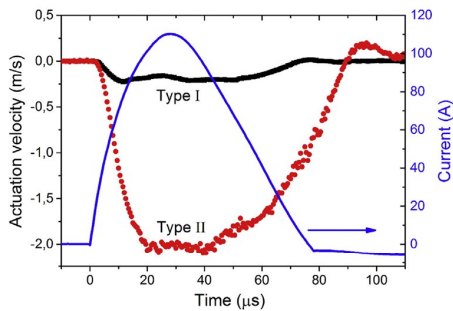


Fig. 3. Actuation velocity (left axis) measured for a single twin boundary of Type I (black squares) and Type II (red circles) propagating through the sample during the magnetic field pulse. The blue curve shows the measured current pulse. (For interpretation of the references to color in this figure legend, the reader is referred to the web version of this article.)

starts, both the mass behind it (left colored side of the sample in the Fig. 2) and the mass involved into the motion are accelerating. At some point, the magnetic field strength creates saturation inside the sample and the driving force that tends the boundary to propagate further reaches its maximum value (according to our calculations, the saturation occurs at $\sim 8 \mu\text{s}$). Further increase of the magnetic field above saturation can only reduce resulting acceleration and velocity by means of the increased magneto static force.

When the driving force is at the maximum and the moving mass is enough accelerated, a constant velocity region begins. Within this region, the whole mass behind the boundary is moving at a constant velocity. As the boundary propagates further inside the sample, new sample volumes are involved into the motion, being accelerated up to the same velocity. Inertia plays an important role for limiting the maximum velocity. As shown in the figure, the constant velocity region begins at $\sim 10 \mu\text{s}$ for Type I and $\sim 20 \mu\text{s}$ for Type II boundary. This difference can be explained by the different masses being involved into the motion during the acceleration path (the initial masses of the growing variant are nearly the same for both types).

At the descending part of the current pulse, when the field strength is not in saturation, the driving force drops and the motion slows down. Because of the inertia of the already moving part of the sample, and depending on the twinning stress, motion can last longer than the current pulse itself. Here the inertia again is manifested by the different times it takes the twin boundary to stop after the pulse ends (compare different deceleration times for different boundary types).

From the measured actuation velocity data, the velocity of a single twin boundary can be obtained by dividing the actuation velocity by the full transformation strain of 6%. This gives the maximum velocities of 4.2 m/s and 33 m/s for Type I and Type II boundaries, respectively. The large, about an order of magnitude, difference between the maximum velocities for twin boundaries of different types can be explained, to a first approximation, by different twinning stresses. The maximum driving force can be produced in saturation conditions, which was realized in the present study. In this case, the driving force is equal to the magnetocrystalline anisotropy energy [3] and does not depend on the type of the twin boundary. The twinning stress creates a nearly constant resistance force to the boundary motion, which is approximately 7 times higher for the Type I boundary as compared to the Type II boundary.

The twin boundary traveling distance obtained from the top view photo images can be further compared with the distance calculated from the actuation velocity data. For this, numerical integration of the actuation velocity temporal dependence was performed and the obtained value was divided by the full transformation strain. The calculated

traveling distance for the twin boundary of Type II is 2.05 mm. This value coincides well with the distance obtained from the corresponded photo images (see Fig. 2b and c). The same calculation performed for the Type I boundary gives a value of $187 \mu\text{m}$, which again is in a good agreement with the corresponding value of $0.19 \pm 0.01 \text{ mm}$ measured from the photo images (not presented).

Fig. 4 shows calculated actuation acceleration time dependencies for both boundary types, during the rising part of the excitation current pulse. The presented data was obtained by direct numerical differentiation of the actuation velocity data. It can be seen that actuation accelerations of 0.37×10^5 and $1.95 \times 10^5 \text{ m/s}^2$ have been reached for Type I and Type II twin boundaries, respectively. Actuation response time was calculated as the time of onset of the acceleration signal above the noise threshold, which is about $2 \mu\text{s}$ for Type II boundary and $2.5 \mu\text{s}$ for Type I boundary. It should be emphasized that no smoothing or filtering was applied to the original data.

In conclusion, a new methodological approach using laser Doppler vibrometry was exploited for studying the twin boundary dynamics in Ni–Mn–Ga, which permits direct measurement of the actuation velocity. The presented approach allows much more precise characterization of the twin boundary motion in MSM sample giving reliable information on actuation velocity and acceleration, as compared to the displacement measurements.

The maximum actuation velocities of 0.25 m/s and 2 m/s were observed for single twin boundary motion of Type I and Type II respectively during pulsed magnetic field excitation under saturation conditions. This implies that the twin boundary velocity along [1 0 0] direction of the crystal reaches the values of 4.2 m/s (Type I) and 33 m/s (Type II) in the Ni–Mn–Ga 5M martensite at room temperature. Actuation response times are measured to be of the order of 2–2.5 μs . Actuation accelerations of 0.37×10^5 and $1.95 \times 10^5 \text{ m/s}^2$ have been reached for Type I and Type II twin boundaries, respectively. The inertia is revealed to be an important factor in regard to twin boundary dynamics in Ni–Mn–Ga.

Further investigation including mathematical modeling of single twin boundary dynamics under the pulsed excitation is required.

The reported results has a potential for the development of new applications, especially in microscale devices in which small masses of MSM elements can significantly increase the working frequency.

The authors thank Alexei Sozinov and Juhani Tellinen for the discussions. This work was financially supported by the Academy of Finland (grant number 277996).

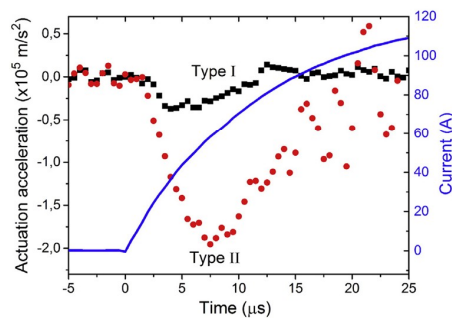


Fig. 4. Actuation acceleration (left axis) calculated from the data of Fig. 3 for single twin boundaries of Type I (black squares) and Type II (red circles). The blue curve shows the current pulse (right axis). (For interpretation of the references to color in this figure legend, the reader is referred to the web version of this article.)

References

- [1] K. Ullakko, J.K. Huang, C. Kantner, R.C. O'Handley, V.V. Kokorin, *Appl. Phys. Lett.* 69 (1996) 1966.
- [2] C.P. Henry, P.G. Tello, D. Bono, J. Hong, R. Wager, J. Dai, S.M. Allen, R.C. O'Handley, *Proc. SPIE* 5053 (2003) 207.
- [3] M.A. Marioni, R.C. O'Handley, S.M. Allen, *Appl. Phys. Lett.* 83 (2003) 3966.
- [4] M. Marioni, D. Bono, A.B. Banful, M. del Rosario, E. Rodriguez, B.W. Peterson, S.M. Allen, R.C. O'Handley, *J. Phys. IV France* 112 (2003) 1001.
- [5] M. A. Marioni, Ph.D. thesis, M.I.T., Cambridge, MA, 2003.
- [6] Y.-W. Lai, R. Schäfer, L. Schultz, J. McCord, *Acta Mater.* 56 (2008) 5130.
- [7] E. Faran, D. Shilo, *J. Mech. Phys. Solids* 59 (2011) 975.
- [8] E. Faran, D. Shilo, *Appl. Phys. Lett.* 100 (2012) 151901.
- [9] E. Faran, D. Shilo, *J. Mech. Phys. Solids* 61 (2013) 726.
- [10] K. Korpiola, A. Sozinov, A. Niskanen, J. Perento, *Proc. on the 4th Int. Conf. Ferromagnetic Shape Memory Alloys 2013*, p. 14.
- [11] A.R. Smith, J. Tellinen, K. Ullakko, *Acta Mater.* 80 (2014) 373.
- [12] A. Sozinov, N. Lanska, A. Soroka, L. Straka, *Appl. Phys. Lett.* 99 (2011) 124103.

Publication II

Saren, A., Nicholls, T., Tellinen, J., Ullakko, K

Direct observation of fast-moving twin boundaries in magnetic shape memory alloy Ni–Mn–Ga 5M martensite

Reprinted with permission from

Scripta Materialia

Vol. 123, pp. 9-12, 2016

© 2016, Elsevier Ltd.



Contents lists available at ScienceDirect

Scripta Materialia

journal homepage: www.elsevier.com/locate/scriptamat

Direct observation of fast-moving twin boundaries in magnetic shape memory alloy Ni–Mn–Ga 5 M martensite

A. Saren^a, T. Nicholls^b, J. Tellinen^a, K. Ullakko^{a,*}^a Material Physics Laboratory, Lappeenranta University of Technology, Laitaatsillantie 3, 57170 Savonlinna, Finland^b Photon (Europe) LTD., The Barn, Bottom Road, West Wycombe, Bucks, HP14 4BS, UK

ARTICLE INFO

Article history:

Received 2 February 2016

Accepted 2 April 2016

Available online xxxx

Keywords:

Ferromagnetic shape memory

Twinning

Dynamic phenomena

Ni–Mn–Ga

ABSTRACT

We report a direct observation of fast Type II twin boundary motion under a pulsed magnetic field excitation in Ni–Mn–Ga 5 M martensite, utilizing high-speed camera technique. Our results demonstrate saturation velocities up to ~39 m/s measured along [100] direction for individual boundaries moving at RT, showing an order of magnitude larger values as compared to the earlier studies. Actuation response times of ~1 μs were observed using laser vibrometry technique. The reported results show a minor role of magneto-static forces and emphasize the role of inertia and internal friction in twin boundary dynamics at the measured speeds.

© 2016 Elsevier Ltd. All rights reserved.

Magnetic shape memory (MSM) alloy Ni–Mn–Ga is considered to be a promising actuating material due to the unique combination of a large strain ~6–10% [1,2] and fast response to magnetic field [3–6]. Twin variants reorientation by twin boundary (TB) motion is the mechanism responsible for the reversible strains observed under mechanical load and magnetic field actuation [7]. Up to now, two types of TBs (Type I and II) were observed in Ni–Mn–Ga 5 M martensite, with substantially different stress and mobility [8,9]. Whereas TB kinetics determines the dynamic properties of MSM-based devices, characterizing the dynamics of individual TBs is one of the key issues in development of the applications.

Typically, a pulsed magnetic field excitation with pulse durations in a sub-millisecond range is used for fast actuation of Ni–Mn–Ga. In pioneering kinetics studies [4,10,11] this approach allowed to fully elongate single crystals of 5 M Ni–Mn–Ga of the size $5 \times 5 \times 10 \text{ mm}^3$ in 200 μs time. The TB configuration was uncontrollable, i.e. multiple twin boundaries formed and moved during the excitation pulse. Comparatively large actuation response (extension onset) times of 40–200 μs were attributed to the effect of mass inertia [11]. Similar studies [3,6,12] indicated the possibility of rapid actuation of initially single variant sample by a pulsed magnetic field with uncontrollable TB pattern. In [3], inertia was suggested to be one of the factors limiting the speed of actuation. Actuation velocity of 4.6 m/s and response time of 2.8 μs were achieved [12].

In [13] stroboscopic imaging technique under AC excitation up to 600 Hz was used to investigate the motion of individual TBs including

averaged velocity calculation based on the changes in twin variant width. The maximum velocity observed was 0.21 m/s.

In the studies [14–17] utilizing magnetic field pulses with duration times 10–120 μs, the average propagation velocities (in normal direction to the boundary) of individual TBs of Type I and Type II were measured to be of the order of 1–2 m/s in fields up to 0.3 T. At fields above 0.75 T (providing saturated driving force), TB velocity saturated at a value of ~2 m/s [17]. The average velocity evaluation was performed based on the measurements of the distance that individual interfaces pass due to the application of a magnetic field pulse. The effect of inertia was estimated to be negligible [14].

In our recent study [18], a laser Doppler vibrometry (LDV) technique was applied to study actuation response of a Ni–Mn–Ga sample subjected to a ~80 μs magnetic field pulse inside a solenoid. We introduced a single TB in the sample prior to the excitation pulse. Maximum actuation velocity of 2 m/s for Type II TB was observed, which corresponds to a velocity of 33 m/s along [1 0 0] direction. This approach allowed us to capture the transient motion of the sample, but still lacking the direct observation of TB movement.

In the present work, we especially focus on the direct experimental observation of the TB velocity saturation of fast-moving Type II TBs in Ni–Mn–Ga 5 M martensite, and pay attention to the possible contribution of the limiting factors such as inertia, internal friction and magneto-static forces.

Fig. 1a shows the schematic of the experimental setup. Two coaxial coils connected in series (Helmholtz configuration), were used to generate the magnetic field. Each coil has an inner diameter of 8.1 mm and consists of 20 turns of an insulated copper wire of 0.2 mm in diameter. The coils are separated by a distance of 4.2 mm. The total inductance and resistance of the coil pair are 13 μH and 0.8 Ω, respectively.

* Corresponding author.

E-mail address: Kari.Ullakko@lut.fi (K. Ullakko).

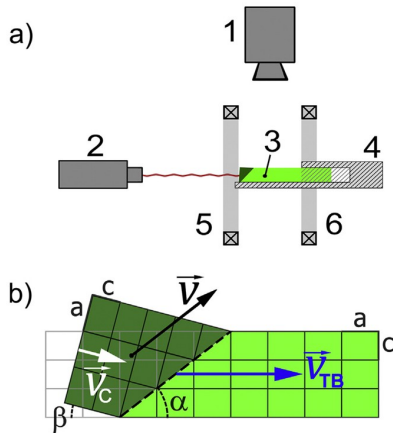


Fig. 1. (a) Experimental setup: (1) high-speed camera, (2) LDV laser head, (3) Ni–Mn–Ga sample, (4) sample holder, (5, 6) Helmholtz coils. (b) Schematic sample side view representing two differently oriented twin variants (axes orientations marked a and c) with a TB (dashed line). Description for the velocity vectors is presented in the text.

The coils' frame has an axial hole for placing the sample holder and a few windows between the coils to observe top and side surface of the sample. The coil pair is connected to a high-voltage pulse generator (EMC, Transient 1000), in series with additional passive circuit, which flattens and extends the pulse providing durations of $\sim 75 \mu\text{s}$.

A high-speed camera (Photron FASTCAM SA5 model 1000 K-M2) working at a frame rate of 775,000 fps with a shutter time of 369 ns and a resolution of 256×16 , was used to acquire real-time images of the sample during the pulsed excitation. These camera settings and optics accessories provided a time resolution of $1.29 \mu\text{s}$ and a spatial resolution of $\sim 8.3 \mu\text{m}/\text{pixel}$ in both directions.

The actuation velocity was measured with a laser vibrometer (Polytec, OFV-5000, OFV-534). A 200 MHz oscilloscope (Metrix Scopix III OX 7204) recorded the voltage, current and actuation velocity signals. The LDV measurement setup is capable to measure transient actuation velocities up to 10 m/s with a time resolution of $0.2 \mu\text{s}$. The high-speed camera and the oscilloscope were triggered using the pulse generator trigger output.

The three samples in this study (named hereafter S1, S2, S3) were mechanically and electrochemically polished $\text{Ni}_{50}\text{Mn}_{28}\text{Ga}_{22}$ single crystals with austenite start temperature of 42°C . All measurements were performed at RT, when the structure was 5 M martensite. The samples' cross-section was approximately $1 \times 1 \text{ mm}^2$ with a length of 6–8 mm. All faces were nearly parallel to the $\{100\}$ planes of the austenite. The maximum strain was measured to be 6%. Each sample was glued on one side (the right side in the Fig. 1a) with an epoxy resin to the plastic holder, which enabled rigid mounting inside the coils' frame. After installing the holder into the frame, the free end of the sample, about 3–4 mm long, was placed coaxially between the coils, as it is shown in the figure. Prior to each pulsed field measurement, the sample was set into a single variant state by applying a 1 T magnetic field along its shortest dimension, which fully elongated the sample. Further, by means of a mechanical stress, the very corner of the sample was converted to the second variant in which the shortest c -axis (equal to the easy axis of magnetization) was aligned along its long dimension. Thus, a single TB was created at the free end. Before and after the pulse, the crystal was photographed in a polarized light. The type of the TB was identified according to the difference in the projections on $\{100\}$ plane (here applicable for the top side of the sample): Type I

TB exhibits nearly parallel projection relative to the crystal's edges while that of Type II is inclined by about 6° [8].

Fig. 1b shows a schematic side view of the crystal. As a first approximation, the unit cell of Ni–Mn–Ga 5 M martensite can be considered tetragonal with a - b and $c/a \sim 0.94$. The constant $\varepsilon_0 = 1 - c/a$ gives an upper limit for the maximum strain available for the crystal during full conversion from one variant to another. If we introduce a TB inside the crystal, as it is shown in Fig. 1b, the crystal faces are tilted at the points where TB is crossing $\{100\}$ planes. Two specific angles, α and β , one can calculate from the geometry using the equations: $\tan\alpha = c/a$ and $\beta = \pi/2 - 2\alpha$. When the sample is subjected to a sufficiently strong magnetic field induced stress, the TB will move in the direction, which leads to the free energy minimization. Thus, TB will move to the right in the case of applying the magnetic field along the sample's length. The driving force for the motion arises from the energy difference of the twin variants with different orientations of the easy axis in respect to the magnetic field. In the figure, the left variant is growing at the expense of the right one having its easy axis perpendicular to the external field direction. As a result, the sample will contract with time at a velocity v_C , which is directly proportional to the TB velocity v_{TB} along $[100]$ direction, with a coefficient ε_0 . The mass of the crystal behind the TB accelerates in the direction parallel to the TB plane (see the vector \vec{v} in the figure).

Here we directly measured the contraction velocity v_C by using the laser vibrometer. (In the case of the measurement along the $[100]$ direction, we have to take into account the tilt angle β , but it gives only a small correction of $\sim 3\%$ that lies within the experimental error.) The velocity v_{TB} was directly measured by the high-speed camera utilizing the light intensity contrast between the two variants, which arises from the surface tilting, under appropriate lighting.

Fig. 2a and b show photo images taken from two sides of the sample S3 before the actuation, and Fig. 2c and d show frame sequences (each third frame shown) acquired by the high-speed camera during two identical field pulses. For the initial position of the TB, we superimposed and scaled the frames from the camera on the top of the photo images (see Fig. 2a, b), according to the clearly distinguishable features on the sample surface. This procedure was performed for every measurement revealing the actual spatial resolution. As it is seen in Fig. 2a (top view), the introduced TB is of Type II. The frames shown below (see Fig. 2c) clearly indicate that the boundary propagated through the visible part of the sample during the pulse without any signs of splitting or additional boundaries nucleation. One can clearly see the acceleration region, nearly constant velocity region, and deceleration region of the TB. From the side view frame sequence shown on Fig. 2d, one can conclude that the motion of the growing variant occurs in a direction, which is parallel to the TB plane, in accordance to the above explanation. The movies named TopViewMovie and SideViewMovie, showing at 20 fps the frames acquired during the measurements with S3, are presented in Supplemental section.

Note that the right part of the sample remains stable during the field pulse. Thus, the relative position of the TB for each top view frame can be determined as the coordinate of the boundary pixel multiplied by the spatial resolution. The calculated position data from three measurements with samples S1–S3 are shown in Fig. 3a, along with the magnetic field pulses. The lower field pulse was used to actuate samples S1 and S2. Both pulses produced field enough for sample saturation during $\sim 70\%$ of the pulse length, with rise times (to saturation level) less than $4 \mu\text{s}$.

Fig. 3b shows the TB velocity data numerically derived from the position dependencies. The samples exhibit a slightly different behaviour after the acceleration part ($\sim 20 \mu\text{s}$), reaching different maximum velocities ranging from 36 m/s for S1 to 39 m/s for S3. TB velocity for S1 after reaching its maximum value at ~ 22 – $32 \mu\text{s}$ starts to decrease and the boundary almost stops before the end of the pulse. From the high-speed camera frames, it was revealed that during the pulse an additional TB of Type I was nucleated and grew in the front of the initial TB

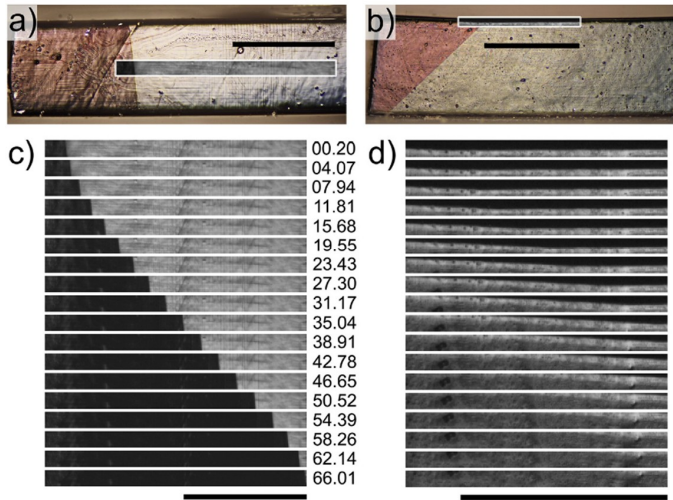


Fig. 2. (a, b) Optical top view (a) and side view (b) images of the sample S3 with a single TB before the actuation. The colour contrast that differentiates the twin variants is due to the use of polarizing filters. The areas captured by the high-speed camera are outlined. (c, d) High-speed camera images acquired during two identical field pulses: top view (c) and side view (d). Timestamps are in μs . The scale bars are of 1 mm.

preventing its motion. For S2, there were no signs of additional TBs nucleation during the pulse time. Nevertheless, the TB motion decelerates while the field is above the saturation threshold. On the other hand, TB

velocity for the sample S3 first saturates at the value of ~ 31 m/s and after that demonstrates second saturation region with higher velocities of 37–39 m/s. We attribute this behaviour to the samples internal and/

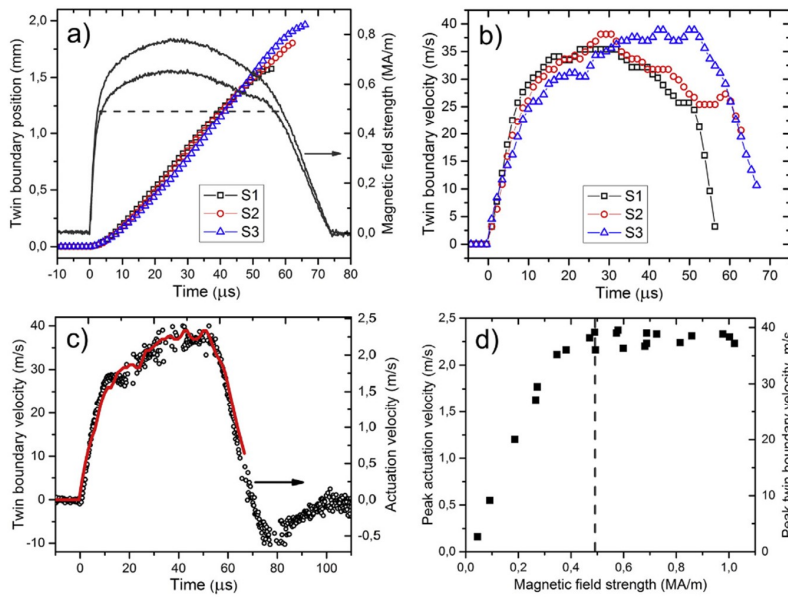


Fig. 3. (a) TB position detected with the high-speed camera for samples S1–S3 (left axis) and magnetic field (right axis) vs time. (b) Calculated TB velocity vs time. (c) Superimposed graphs for calculated TB velocity (left axis, red line) and actuation velocity simultaneously measured with LDV (open circles). (d) Peak actuation velocity dependence on magnetic field. Dashed lines in graphs a and d represent the field level that saturates the driving force for TB motion. (For interpretation of the references to color in this figure legend, the reader is referred to the web version of this article.)

or surface inhomogeneity, which affects the TB mobility. The other important feature of the observed motion is the acceleration region of $\sim 20\text{--}30\ \mu\text{s}$, under maximum driving force, that is pronounced for all samples before reaching the saturation velocity. This phenomenon is attributed to both inertia of the accelerating mass, and strong internal friction dependence on the TB velocity.

It is interesting to compare the direct TB velocity measurement described above with the actuation velocity measurement done using LDV technique. In Fig. 3c, the solid red line repeats the TB velocity data obtained for S3, and open circles represent simultaneously measured actuation velocity signal. Here, the scaling factor between the axes is equal to the ϵ_0 . The curves coincide well, thus the LDV measurement properly describes the TB motion. A small excursion in the negative direction after the field pulse ends, is mostly due to the glue acting as a spring, as is also visible in the high-speed camera frames. The response time, defined as the time between the start of the current pulse and the actuation velocity onset above the noise threshold, was $\sim 1\ \mu\text{s}$.

Fig. 3d shows the actuation velocity dependence on the magnetic field for sample S3, for single TB motion of Type II. The right axis represents the corresponding TB velocity scale. This graph clearly demonstrates velocity saturation between the threshold field of $\sim 0.5\ \text{MA/m}$ up to $1\ \text{MA/m}$. The conclusion can be made that there is no significant influence of the field-dependent resistance forces like magneto-static forces, on the TB motion.

In conclusion, we have directly observed for the first time fast-moving Type II TBs in Ni–Mn–Ga 5 M martensite at RT using high-speed camera imaging. The saturation TB velocity and corresponding actuation velocity achieved are $\sim 39\ \text{m/s}$ and $\sim 2.3\ \text{m/s}$, respectively. The measured response (velocity onset) time is $\sim 1\ \mu\text{s}$, which is the shortest time reported for TB motion in Ni–Mn–Ga. It is revealed that inertia and internal friction significantly affect the TB dynamics at the measured speeds. The results show a minor role of the field-

dependent resistance forces such as magneto-static forces on TB motion. The reported results would help the development of novel applications that could take full advantage of the high-speed of Ni–Mn–Ga.

Supplementary data to this article can be found online at <http://dx.doi.org/10.1016/j.scriptamat.2016.04.004>

Acknowledgement

The authors thank Kim Törnqvist (Cheos Oy, Finland) for providing the high-speed camera. This work was financially supported by the Academy of Finland (grant number 277996).

References

- [1] S.J. Murray, M. Marioni, S.M. Allen, R.C. O'Handley, Appl. Phys. Lett. 77 (2000) 886.
- [2] A. Sozinov, A.A. Likhachev, N. Lanska, K. Ullakko, Appl. Phys. Lett. 80 (2002) 1746.
- [3] J. Tellinen, I. Suorsa, A. Jääskeläinen, I. Aaltio, K. Ullakko, Proc. on the 8th Int. Conf. on New Actuators, 2002 566.
- [4] M.A. Marioni, R.C. O'Handley, S.M. Allen, Appl. Phys. Lett. 83 (2003) 3966.
- [5] I. Suorsa, E. Pagounis, K. Ullakko, J. Magn. Magn. Mater. 272–276 (2004) 2029.
- [6] K. Korpiola, A. Sozinov, A. Niskanen, J. Perento, Proc. on the 4th Int. Conf. Ferromagnetic Shape Memory Alloys, 2013 14.
- [7] K. Ullakko, J.K. Huang, C. Kantner, R.C. O'Handley, V.V. Kokorin, Appl. Phys. Lett. 69 (1996) 1966.
- [8] A. Sozinov, N. Lanska, A. Soroka, L. Straka, Appl. Phys. Lett. 99 (2011) 124103.
- [9] L. Straka, O. Heczko, H. Seiner, N. Lanska, J. Drahoukoupil, A. Soroka, S. Fähler, H. Hänninen, A. Sozinov, Acta Mater. 59 (2011) 7450.
- [10] M. Marioni, D. Bono, A.B. Banful, M. del Rosario, E. Rodriguez, B.W. Peterson, S.M. Allen, R.C. O'Handley, J. Phys. IV France 112 (2003) 1001.
- [11] M.A. Marioni, Ph.D. thesis, M.I.T., Cambridge, MA, 2003.
- [12] A.R. Smith, J. Tellinen, K. Ullakko, Acta Mater. 80 (2014) 373.
- [13] Y.-W. Lai, R. Schäfer, L. Schultz, J. McCord, Acta Mater. 56 (2008) 5130.
- [14] E. Faran, D. Shilo, J. Mech. Phys. Solids 59 (2011) 975.
- [15] E. Faran, D. Shilo, Appl. Phys. Lett. 100 (2012) 151901.
- [16] E. Faran, D. Shilo, J. Mech. Phys. Solids 61 (2013) 726.
- [17] E. Faran, D. Shilo, Mater. Sci. Technol. 30 (2014) 1545.
- [18] A. Saren, D. Musienko, A.R. Smith, K. Ullakko, Scr. Mater. 113 (2016) 154.

Publication III

Saren, A., Ullakko, K.

Dynamic twinning stress and viscous-like damping of twin boundary motion in magnetic shape memory alloy Ni-Mn-Ga

Reprinted with permission from

Scripta Materialia

Vol. 139, pp. 126-129, 2017

© 2017, Acta Materialia Inc. Published by Elsevier Ltd.



Regular Article

Dynamic twinning stress and viscous-like damping of twin boundary motion in magnetic shape memory alloy Ni-Mn-Ga



A. Saren, K. Ullakko *

Material Physics Laboratory, Lappeenranta University of Technology, Lahtiakallio 3, 57170 Savonlinna, Finland

ARTICLE INFO

Article history:

Received 9 May 2017

Received in revised form 7 June 2017

Accepted 10 June 2017

Available online xxxx

Keywords:

Ferromagnetic shape memory

Twinning

Dynamic phenomena

Modeling

Ni-Mn-Ga

ABSTRACT

We demonstrate a strong dependence of twinning stress (TS) on twin boundary (TB) velocity in $\text{Ni}_{50}\text{Mn}_{28}\text{Ga}_{22}$ 5M martensite. Different types of TBs exhibit substantially different dynamic properties under magnetic field actuation. For type 1 interface, the dynamic TS drastically increases from its quasi-static value of ~ 0.6 to ~ 3.2 MPa, limiting the TB velocity to 3–4 m/s at saturation magnetic driving force. Type 2 TBs show a gradual increase of the TS from ~ 0.1 MPa to ~ 2 MPa, reaching velocities of ~ 35 m/s. Our findings bring to the fore type 2 interfaces for applications demanding high actuation speeds and frequencies.

© 2017 Acta Materialia Inc. Published by Elsevier Ltd. All rights reserved.

Twin boundary (TB) motion is the mechanism responsible for the large magnetically and mechanically induced deformation in magnetic shape memory (MSM) alloys. From the pioneer studies by Ullakko and co-workers [1,2], Ni-Mn-Ga-based alloys are considered to be highly promising actuating MSM materials due to the unique combination of a large transformation strain ~ 6 – 10% [3,4] and fast sub-millisecond response to magnetic fields [5–10]. The investigation of TB dynamics in MSM alloys on the level of individual TBs has attracted recently more attention [11–19], since the TB mobility dictates the dynamic properties of MSM-based devices, especially in high frequency or high-speed applications.

The five-layered modulated (5M) Ni-Mn-Ga martensite having typical transformation strain of $\sim 6\%$, has approximately tetragonal lattice with a slight monoclinic distortion [20]. In this material, the shortest c -axis is the axis of easy magnetization (in which the cell magnetic moment is oriented), and the difference between longer a and b axes is only about 0.4%. Numerous martensitic twin variants with nearly perpendicular c -axis orientations can coexist in a single crystalline sample, being connected by TBs. Two crystallographically different types of TBs have been observed in 5M Ni-Mn-Ga: type 1 having rational twinning plane and irrational shear direction, and type 2 with irrational twinning plane and rational shear direction [20,21].

Twinning stress (TS), a key property of MSM materials, determines the level of an applied stress required for twin variant reorientation via TB motion. Type 1 and type 2 twin interfaces demonstrate

substantially different TS: ~ 1 MPa for type 1, and ~ 0.05 – 0.3 MPa for highly mobile type 2 [20,21]. These values are usually measured using conventional stress-strain apparatus, thus describing TB properties in a limited range of TB velocities, typically well below 0.1 m/s. Currently, there is no experimental data in the literature on the TS dependence on the TB velocity. Moreover, in the kinetic relation approach the mobility coefficient is assumed as constant [13–17].

In [18,19] we reported on experimental investigation of single TB motion for both type 1 and type 2 TBs, under a pulsed magnetic field excitation in Ni-Mn-Ga 5M martensite, utilizing laser Doppler vibrometry (LDV) and high-speed camera techniques. These results showed a minor role of magneto-static forces and emphasized the role of inertia and internal friction in TB dynamics. In the present study, we develop a macroscopic variable-mass model to describe the observed phenomenon. This approach allowed us to evaluate the TS change with TB velocity.

Few samples with cross-section of $\sim 1 \times 1$ mm² and length of ~ 6 – 10 mm were cut from a single crystal with composition $\text{Ni}_{50}\text{Mn}_{28}\text{Ga}_{22}$ and austenite start temperature of 42 °C, and prepared as described elsewhere [18,19]. Quasi-static TS of the studied samples was measured to be of ~ 0.6 MPa for type 1 and ~ 0.1 MPa for type 2 TBs [18]. Magnetic anisotropy measurements were performed with a custom-made setup. The saturation magnetization, M_s , was revealed to be 0.7 T, and the anisotropy field, H_a , 560 kA/m, at RT. For the anisotropy constant, K_u , we obtained: $K_u = \mu_0 M_s H_a / 2 = 196$ kJ/m³, which coincides with the previous result obtained for a similar alloy composition at RT [22].

The LDV setup described in [18] was used to measure the contraction velocity of the sample during magnetic field actuation, with a temporal resolution of 0.2 μ s. The magnetic field source was a 16 mm length

* Corresponding author.

E-mail address: Kari.Ullakko@lut.fi (K. Ullakko).

solenoid with 4 mm inner diameter, which consisted of 140 turns of 0.2 mm insulated copper wire. The solenoid was connected to a high-voltage pulse generator, in series with an additional passive circuit used to square and extend the current pulse to ~100 μ s.

Fig. 1 schematically explains the twin variants arrangement in the sample before the actuation pulse and the shape change during the TB motion. The sample consists of two differently oriented variants, with a single TB in between. As a first approximation, we consider the unit cell of Ni-Mn-Ga 5M martensite tetragonal with $a \sim b$ and $c/a \sim 0.94$. From the ratio c/a , one can directly derive the transformation strain $\epsilon_0 = 1 - c/a \sim 0.06$, as well as the angles $\alpha = \arctan(c/a) \sim 43.23^\circ$ and $\beta = \frac{\pi}{2} - 2\alpha \sim 3.54^\circ$. Different TB types visually differ in the projections on the top side: type 1 boundary exhibits nearly parallel projection relative to the crystal's edges while that of type 2 is inclined by about 6° [20]. The projections on the side view for both types are the same.

When the sample is subjected to a magnetic field pulse, the TB will move in the direction, which leads to the free energy minimization. The driving force for the motion arises from the energy difference of the twin variants with different orientations of the easy c -axis in respect to the magnetic field direction. In the present case, the left variant is growing at the expense of the right variant having its easy axis perpendicular to the external field, applied along the direction X . As a result, the sample will contract with time at velocity v_c . Two steps of this motion are shown in Fig. 1, describing TB position change from L_0 to L_1 . The TB velocity, v_{TB} , defined here as the velocity of the boundary along $[1\ 0\ 0]$ direction, is directly proportional to the contraction velocity: $v_{TB} = v_c/\epsilon_0$. From the geometry, it follows that any point and the whole mass of the crystal behind the TB move in the direction, which is parallel to the TB plane – see vector \vec{v} in Fig. 1. The absolute values v and v_{TB} are directly proportional as $v_{TB} = k_0 v$, where $k_0 = \cos\alpha + \sin\alpha/\tan\beta \sim 11.8$.

An important conclusion coming from the above description is that the moving mass behind the TB changes all the time during the TB motion, showing an example of a variable-mass system (note that the sample is glued to the holder on its right side, so that only the left variant moves). Hence, we can write Newton's second law in the form of the momentum change [23]: $d\vec{p}/dt = \vec{F}_{ext}$, where $\vec{p} = m\vec{v}$ is the momentum of the mass m (the mass of the growing variant) moving at the velocity \vec{v} , t is time, and \vec{F}_{ext} is the vector sum of all external forces applied to the mass in the direction of \vec{p} (see Fig. 1). The mass m can be expressed as a function of the TB position L : $m(L) = m_0 + \rho A_0(L - L_0)$, where m_0 is the initial mass of the moving variant, ρ – volumetric mass density of the alloy, ~ 8000 kg/m³, A_0 – cross-sectional area of

the sample on the right side of the TB, and L_0 – initial position of the TB. Now we can write Newton's second law in the following form:

$$\rho A_0 \frac{dL}{dt} \vec{v} + (m_0 + \rho A_0(L - L_0)) \frac{d\vec{v}}{dt} = \vec{F}_{ext} \quad (1)$$

In order to convert Eq. (1) into a scalar form, we can take into account the proportionality between v_{TB} and v , and the relationship $v_{TB} = dL/dt$. Defining the positive direction as the direction of the vector \vec{v} , we get a scalar differential equation for the function $L(t)$:

$$\frac{\rho A_0}{k_0} \left(\frac{dL}{dt} \right)^2 + \frac{m_0 + \rho A_0(L - L_0)}{k_0} \frac{d^2L}{dt^2} = F_{ext} \quad (2)$$

The value F_{ext} in the right part of Eq. (2) is the absolute value of the vector \vec{F}_{ext} , and is positive if the vectors \vec{F}_{ext} and \vec{v} are co-directional. More definitely, the force F_{ext} can be represented by a difference between the magnetic driving force, F_{mag} , which promotes the TB motion, and a sum of resistance forces of different nature, F_{res} : $F_{ext} = F_{mag} - F_{res}$. These forces are naturally shear forces, and may have a distribution along the TB plane. For a convenience of the further discussion, we change these forces to equivalent normal stresses (or pressures) acting on the TB in the direction X (see Fig. 1). Thus, the equivalent magnetic field-induced stress (MFIS) will relate to the force F_{mag} as $\sigma_{mag} = F_{mag}/(A_0 \cos\alpha)$, and for the resistance stress we can write: $\sigma_{res} = F_{res}/(A_0 \cos\alpha)$. Substituting in Eq. (2) forces by the stresses and multiplying both sides by $k_0/(\rho A_0)$, we get:

$$\left(\frac{dL}{dt} \right)^2 + \left[\frac{m_0}{\rho A_0} + (L - L_0) \right] \frac{d^2L}{dt^2} = \frac{k_0}{\rho} \cos\alpha [\sigma_{mag} - \sigma_{res}] \quad (3)$$

Eq. (3) allows evaluation of the total driving stress, $\sigma_{mag} - \sigma_{res}$, applied to the TB during its motion, based on the measured contraction velocity $v_c(t)$, supposing possibility of integration and differentiation of the velocity signal. From Eq. (3), it follows that at a limited driving stress the TB velocity will saturate reaching a maximum value of

$$v_{TB}^{max} = \left(\frac{dL}{dt} \right)_{max} = \sqrt{\frac{k_0}{\rho} \cos\alpha [\sigma_{mag} - \sigma_{res}]} \quad (4)$$

The velocity saturation indicates a state when the momentum of the moving variant is increasing only because of the growth of the mass.

We specially designed our setup to have saturation field conditions during the actuation pulse. Physically saturation means that all the individual magnetic moments in both variants are aligned with the magnetic field and correspondent MFIS approaches its maximum value. Thus, magnetic fields exceeding H_a provide a constant value of the MFIS: $\sigma_{mag} = K_u/\epsilon_0 = 3.27$ MPa [24]. In addition, the effects of magnetization rotation at the TB interface and domain walls motion are excluded from σ_{res} in saturation field.

The applied magnetic field pulse (calculated based on the electric current measurement) is presented in Fig. 2a. The saturation field is achieved at ~ 1.8 μ s and maintained during ~ 100 μ s. Prior to each actuation, the samples were photographed in polarized light to evaluate the TB type and parameter m_0 . Fig. 2b shows $v_{TB}(t)$ dependencies derived from the measured contraction velocity data $v_c(t)$, for both types of individual TBs propagated in the MSM samples. The boundaries traveled ~ 5 mm in the case of type 2, and ~ 0.3 mm of type 1. The velocity graphs clearly demonstrate three parts of the kinetics: (1) acceleration and (2) velocity saturation during the magnetic field pulse, and (3) deceleration after the field drops to zero. There is a distinct, about an order, difference between saturation velocities achieved for type 1 ($v_{TB} \sim 2\text{--}4$ m/s) and type 2 ($v_{TB} \sim 35$ m/s) boundaries. The acceleration and deceleration parts are very short for type 1 interface, whereas in the case of type 2, there is a very clear sign of the inertia effect. This effect is more

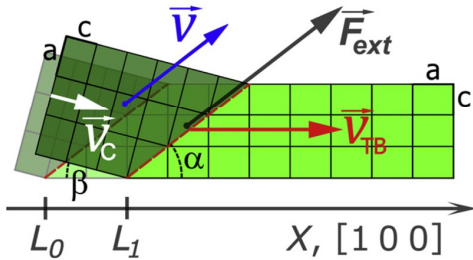


Fig. 1. Schematic side view of the Ni-Mn-Ga sample. Two subsequent configurations of the sample during the TB motion are shown, with correspondent TB positions measured along $[1\ 0\ 0]$ direction, L_0 and L_1 . The red dashed line denotes the TB. Description for the angles α and β , velocity and force vectors is presented in the text. The ratio d/c is enlarged for clarity. (For interpretation of the references to colour in this figure legend, the reader is referred to the web version of this article.)

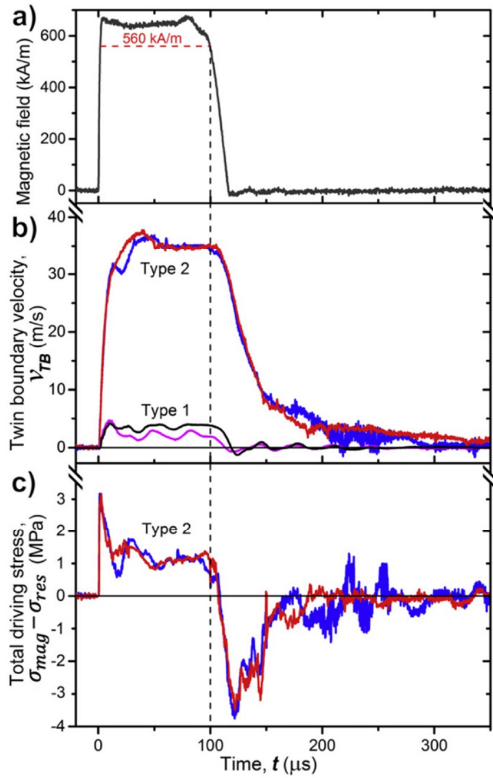


Fig. 2. (a) Magnetic field pulse used for MSM samples actuation. (b) TB velocity dependence on time, for single TBs motion of type 1 and 2, obtained from the measured contraction velocity. (c) The total driving stress, $\sigma_{mag} - \sigma_{res}$, vs time dependencies, derived from the TB velocity data for type 2.

pronounced after the field turns off and the mass (about 8 times larger compared to m_0 , for type 2 TBs), moving at 3 m/s velocity, starts to decelerate because of the resistance forces. There are also oscillations visible in the measured velocity signal, which represent second-order effects, and will not be discussed in the present paper.

Based on the velocity data and the known parameters m_0 and A_0 , the temporal dependence of the total driving stress was evaluated for the type 2 case. The result is shown in Fig. 2c. At $t \sim 1.5\text{--}2\ \mu\text{s}$ from the beginning of the field pulse, the total driving stress sharply reaches ~ 3 MPa and then drops down to $1\text{--}1.5$ MPa within $\sim 10\text{--}20\ \mu\text{s}$. The TB velocity changes from ~ 10 to 33 m/s. After few oscillations, the driving stress remains stabilized at $\sim 1\text{--}1.2$ MPa for both samples, until the magnetic field is switched off. After the field is removed, the driving stress immediately becomes negative reaching about ~ 3.5 MPa, meaning that the resistance forces begin to decelerate the moving mass. Again, two different parts can be distinguished during deceleration: (1) fast deceleration part lasting approximately $50\ \mu\text{s}$, with the velocity dropping from 30 down to 5 m/s, and (2) slow deceleration part when the resistance stress approaches a nearly zero value (slight oscillations are caused by the noise) and the TB velocity diminishes very slowly.

The investigation of the possible resistance forces acting on the TB during its motion was of our particular interest. The TS is the first obvious term that should be included in σ_{res} . If substituted into Eq. (4), the

predicted saturation velocities reach values of 53–58 m/s for TS ranged from 0.6 down to 0.1 MPa, at $\sigma_{mag} \sim 3.27$ MPa. These values are much higher as compared to experimentally observed saturation TB velocities. Thus, additional terms should be added to the quasi-static TS in order to explain the difference.

We discuss first the saturation field conditions. One can expect few possible effects arising from the magnetic field that could suppress the motion of the TB. First, the skin effect from the eddy currents can influence on the MFIS at quickly rising/falling fields. The estimated penetration depth is of the order of 1 mm at the front of the actuation pulse. This effect can only explain the observed lag of $\sim 0.8\ \mu\text{s}$ between the magnetic field pulse start and the velocity signal onset, as the field pulse has nearly square shape. Other possible effects are related to magneto-static forces, torques because of the kinked shape of the sample, and eddy currents generated because of the motion of the sample in a strong magnetic field. All these magnetic field-related effects should be dependent on the field strength. However, our previous results [19] showed no decrease of the maximum TB velocity at fields beyond H_0 . Thus, the above-mentioned field-related effects can be excluded. Furthermore, these effects are not related to the TB type. Therefore, they would suppress the supposed 53–58 m/s velocities to a similar extent, whereas an order of magnitude difference appears between the saturation velocities for the two different TB types.

Our hypothesis, which explains the experimental results, is velocity-dependent or dynamic TS caused by viscous-like damping of the TB

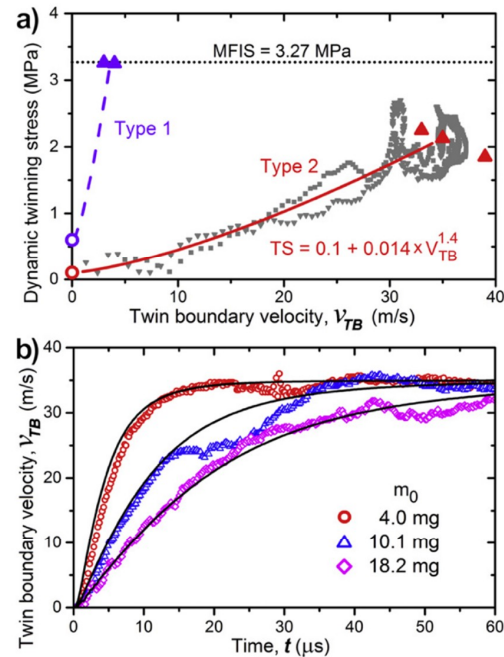


Fig. 3. (a) Estimated dynamic TS dependencies on TB velocity in saturation magnetic field, for different TB types. Open circles represent the quasi-static TS and solid triangles – dynamic TS values at saturation velocities for different samples, according to Eq. (4). Gray symbols represent the dynamic TS derived from the data displayed in Fig. 2c for $t < 100\ \mu\text{s}$. Solid line is a power law fit to the gray symbols. (b) Measured (symbols) and simulated (lines) type 2 TB velocity dependencies on time in saturation magnetic field, for different initial masses m_0 . The dynamic TS was modeled with the formula in panel a and Eq. (3) solved using Mathcad software with time interval of 10^{-8} s.

motion. We describe the resistance stress σ_{res} as a sum of quasi-static TS value and a second, velocity-dependent term. To reveal the relationship between the TB velocity and the dynamic TS in saturation field, we subtract the total driving stress (values depicted in Fig. 2c at $t < 100 \mu\text{s}$) from the saturation MFIS value of 3.27 MPa. Fig. 3a shows the obtained dynamic TS versus TB velocity for type 2 TBs (see the gray symbols). As it is seen from the graph, there is a very weak TS dependence on the velocity up to ~ 8 – 10 m/s. Above these velocities, the dynamic TS starts to grow gradually, approaching ~ 2 MPa at velocities higher than 30 m/s. The solid triangles represent the dynamic TS, σ_{res} , obtained with Eq. (4) for saturation velocities measured with different samples, including our earlier results [19]. The solid line is a fitting to a power law of the TS data, connecting two fixed points: at zero velocity (quasi-static TS, open circle) and saturation velocity of 35 m/s.

Due to the oscillations in the measured velocity, we could not perform the above calculations for type 1 boundary. Nevertheless, the TS estimation can be done based on the saturation TB velocity measured as 2–4 m/s. From Eq. (4), it follows that the dynamic TS changes from the quasi-static value of ~ 0.6 MPa up to ~ 3.26 MPa, actually depleting the MFIS. Taking into account previous studies showing velocity-independent TS at small TB velocities, at least up to 10^{-2} m/s [17], we conclude, that the dynamic TS for type 1 boundary has a sublinear and sharp dependence on the TB velocity (dashed line in Fig. 3a).

According to the total driving stress dependence obtained for type 2 TBs moving at zero field (at $t > 120 \mu\text{s}$ in Fig. 2c), the dynamic TS is about two times that in saturation field, for same velocity values. Evidently, compared to saturation field conditions, additional energy dissipative mechanisms are involved, primarily due to magnetization rotation and domain wall motion as the TB propagates further. From our data, these contributions are estimated to have negligible effect at velocities less than ~ 5 – 8 m/s. Since this type of resistance forces is not related to the TB type, we can expect no such effect for type 1 TBs moving at ~ 3 – 4 m/s.

Finally, to provide a validation of the proposed model, we compared experimental and simulated dependencies $v_{TB}(t)$ in saturation field, changing the parameter m_0 . The modeled curves demonstrated good agreement with the measured data, as seen in Fig. 3b.

In summary, a macroscopic variable-mass model describing single TB motion in Ni-Mn-Ga 5M martensite is developed. Based on the proposed model and actuation velocity measurements, we demonstrate that TS is strongly dependent on the TB velocity. Furthermore, the TS dependence on the TB velocity is substantially different for two crystallographically different TB types. The type 2 TBs exhibit dynamic TS of

~ 2 MPa in saturation field, reaching TB velocities of 35–39 m/s, whereas type 1 interfaces were found to deplete the driving MFIS at an order smaller velocities of ~ 3 – 4 m/s. The dynamic TS at zero field is about twice the dynamic TS in saturation field for type 2 TBs, and has negligible effect for both TB types at velocities less than ~ 5 – 8 m/s. Our findings suggest that type 2 interfaces are preferable in applications demanding high actuation speeds and frequencies. Further investigations are required to specify more exactly the dynamic TS dependencies.

Acknowledgement

A.S. thanks Juhani Tellinen and Alexey Sozinov for useful discussions. This work was supported by the Academy of Finland (grant numbers 277996 and 287016).

References

- [1] K. Ullakko, J. Mater. Eng. Perform. 5 (3) (1996) 405.
- [2] K. Ullakko, J.K. Huang, C. Kantner, R.C. O'Handley, V.V. Kokorin, Appl. Phys. Lett. 69 (1996) 1966.
- [3] S.J. Murray, M. Marioni, S.M. Allen, R.C. O'Handley, Appl. Phys. Lett. 77 (2000) 886.
- [4] A. Sozinov, A.A. Likhachev, N. Lanska, K. Ullakko, Appl. Phys. Lett. 80 (2002) 1746.
- [5] J. Tellinen, I. Suorsa, A. Jääskeläinen, I. Aaltio, K. Ullakko, Proc. on the 8th Int. Conf. on New Actuators, 2002 566.
- [6] M.A. Marioni, R.C. O'Handley, S.M. Allen, Appl. Phys. Lett. 83 (2003) 3966.
- [7] I. Suorsa, E. Pagounis, K. Ullakko, J. Magn. Magn. Mater. 272–276 (2004) 2029.
- [8] K. Korpiola, A. Sozinov, A. Niskanen, J. Perento, Proc. on the 4th Int. Conf. Ferromagnetic Shape Memory Alloys, 2013 14.
- [9] M. Marioni, D. Bono, A.B. Banful, M. del Rosario, E. Rodriguez, B.W. Peterson, S.M. Allen, R.C. O'Handley, J. Phys. IV France 112 (2003) 1001.
- [10] M. A. Marioni, (Ph.D. thesis, M.I.T., Cambridge, MA), 2003.
- [11] Y.-W. Lai, R. Schäfer, L. Schultz, J. McCord, Acta Mater. 56 (2008) 5130.
- [12] A.R. Smith, J. Tellinen, K. Ullakko, Acta Mater. 80 (2014) 373.
- [13] E. Faran, D. Shilo, J. Mech. Phys. Solids 59 (2011) 975.
- [14] E. Faran, D. Shilo, Appl. Phys. Lett. 100 (2012) 151901.
- [15] E. Faran, D. Shilo, J. Mech. Phys. Solids 61 (2013) 726.
- [16] E. Faran, D. Shilo, Mater. Sci. Technol. 30 (2014) 1545.
- [17] E. Faran, D. Shilo, Shape Mem. Superelast. 1 (2) (2015) 180.
- [18] A. Saren, D. Musienko, A.R. Smith, K. Ullakko, Scr. Mater. 113 (2016) 154.
- [19] A. Saren, T. Nicholls, J. Tellinen, K. Ullakko, Scr. Mater. 123 (2016) 9.
- [20] A. Sozinov, N. Lanska, A. Soroka, L. Straka, Appl. Phys. Lett. 99 (2011) 124103.
- [21] L. Straka, O. Heczko, H. Seiner, N. Lanska, J. Drahokoupil, A. Soroka, S. Fähler, H. Hänninen, A. Sozinov, Acta Mater. 59 (2011) 7450.
- [22] I. Aaltio, A. Sozinov, Y. Ge, K. Ullakko, V.K. Lindroos, S.-P. Hannula, (Ed-in-chief) in: S. Hashmi (Ed.), Reference Module in Materials Science and Materials Engineering, Elsevier, Oxford 2016, pp. 1–14.
- [23] A. Sommerfeld, Lectures on Theoretical Physics, Mechanics, vol. I, Academic Press, New York, 1959.
- [24] A.A. Likhachev, K. Ullakko, Phys. Lett. A 275 (2000) 142.

Publication IV

Saren, A., Tellinen, J., Musiienko, D., Ullakko, K.

**Fast Actuation of Magnetic Shape Memory Material Ni-Mn-Ga Using Pulsed
Magnetic Field**

Reprinted with permission from

Proceedings of the 15th International Conference on New Actuators (ed. H. Borgmann)
pp. 101-103, 2016

© 2016, MESSE BREMEN, WFB Wirtschaftsförderung Bremen GmbH

Fast Actuation of Magnetic Shape Memory Material Ni-Mn-Ga Using Pulsed Magnetic Field

A. Saren, J. Tellinen, D. Musiienko, K. Ullakko
Lappeenranta University of Technology, Savonlinna, Finland

Abstract:

Pulsed magnetic field-induced actuation of magnetic shape memory material Ni-Mn-Ga 5M martensite has been studied. Saturation velocities of fast-moving single type II twin boundaries in a range of 35–39 m/s were directly observed using high-speed camera technique. Corresponding actuation velocities of 2.1–2.3 m/s were acquired using laser Doppler vibrometry technique, both for elongation and contraction of the sample. In a case of multiple twin boundaries motion, actuation velocities of 4–5.5 m/s and actuation accelerations of $(4-7) \times 10^5$ m/s² were achieved. The actuation response time was measured to be less than 1 μ s. The reported results have a potential for the development of new applications, especially in microscale devices where the working frequency can be significantly increased. Example potential applications are fast optical and electrical switches, pneumatic/hydraulic valves, microfluidic pumps and valves, micromanipulators and grippers.

Keywords: Magnetic Shape Memory, Ni-Mn-Ga, Twinning, Twin Boundary Dynamics, Magnetic Field Actuation

Introduction

Magnetic Shape Memory (MSM) alloy Ni-Mn-Ga is a promising actuating material due to the combination of a large strain ~6-10% [1, 2] and fast response to magnetic field [3]. Twin variants reorientation by twin boundary (TB) motion is the mechanism responsible for the reversible strains observed under mechanical load and magnetic field actuation [4]. Up to now, two types of TBs (type I and II) were observed in Ni-Mn-Ga 5M martensite, with substantially different stresses [5]. Recently, we observed about an order of magnitude difference in saturation velocities of TBs of these types [6]. Here we focus on the direct experimental observation of fast-moving type II single TBs under pulsed magnetic field excitation, and actuation velocity measurements for both elongation and contraction of the sample, in saturation magnetic field. The contribution of the limiting factors such as inertia and internal friction are discussed.

Experimental procedures

The MSM samples used in the study were mechanically and electrochemically polished Ni₅₀Mn₂₈Ga₂₂ single crystals with austenite start temperature of 42 °C. All measurements were done at RT. The samples' cross-section was $\sim 1 \times 1$ mm² with a length of 8-10 mm, with faces nearly parallel to the {1 0 0} planes of the austenite. The maximum strain, ϵ_0 , was measured to be 6%. The experimental setup is shown in Fig. 1a. A Helmholtz coil, connected to a pulse generator (EMC, Transient 1000), created a magnetic field pulse providing saturation field inside the sample during ~70% of the pulse length, with rise time (to saturation level) about 5 μ s. A high-speed camera (Photron FASTCAM SA5) at a frame rate of 775000 fps was used to acquire real-time images

from the top surface, while a laser Doppler vibrometer (LDV) (Polytec, OFV-5000, OFV-534) was observing the left facet of the sample. Each sample was glued on its one end to a holder providing a proper alignment inside the coil frame. Prior to the pulsed excitation, the sample was set into a single variant state by placing it into a constant magnetic field of ~1 T, with subsequent introduction of a single

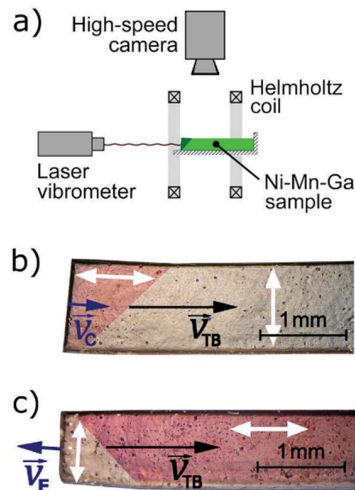


Fig. 1: (a) Schematic of the experimental setup. (b, c) Optical side-view images of the sample with a single TB, for two twin variant arrangements. Color contrast is due to the use of polarized light. The easy axis directions are marked with white arrows. See the description of the velocity vectors in the text.

TB at the free unglued end, by means of mechanical stress. In the first twin variant configuration (see Fig.1b), the introduced variant at the left end has its shorter easy axis aligned along the sample largest dimension. When the magnetic field is applied to the sample along its length, the left favorable variant will grow, and TB will move to the right. As a result, the sample will contract with time at a velocity v_C , which is directly proportional to the TB velocity v_{TB} along $[1\ 0\ 0]$ direction, with a coefficient equal to ϵ_0 . In the second configuration, the introduced variant has its easy axis aligned perpendicularly (see Fig.1c) to the sample length. In this case, we observed elongation of the sample at a velocity v_E when placing it into a perpendicular magnetic field (by rotation the Helmholtz coil by 90° compared to the arrangement shown in Fig.1a).

Results

Fig.2a shows sample top-view image taken prior to the field pulse, with introduced a single TB of type II (twin variants arrangement according to Fig.1b). The high-speed camera was observing a part of the sample, which is outlined. A set of acquired frames is shown in Fig.2b. The light intensity contrast between two variants arises from the surface tilt angle of $\sim 3.5^\circ$. The frames clearly indicate that the TB propagated through the visible part of the

sample during the pulse without any signs of splitting or additional TBs nucleation. One can clearly see the acceleration region, nearly constant velocity region, and deceleration region of the TB motion. The relative position of the TB for each top-view frame was determined and is shown in Fig.2c, along with the applied magnetic field pulse. Further, TB velocity data was numerically derived from the position dependencies and is shown in Fig.2d. Different samples exhibited a slightly different behavior with maximum TB velocities ranging from 36 to 39 m/s. We attribute this behavior to the samples internal and/or surface inhomogeneity, which affects the TB mobility. An important feature of the observed motion is the acceleration region of $\sim 20\text{--}30\ \mu\text{s}$, under maximum driving force, that is pronounced for all samples before reaching the maximum velocity. This phenomenon is attributed to both inertia of the accelerating mass, and strong internal friction dependence on the TB velocity.

Direct actuation velocity measurements provided by the LDV, showed corresponding contraction velocities of 2.1–2.3 m/s, in agreement with high-speed camera data. Better time resolution obtainable with LDV setup, allowed us to estimate the actuation response time (defined here as the time between the start of the current pulse and the actuation velocity onset above the noise threshold) to be less than 1 μs .

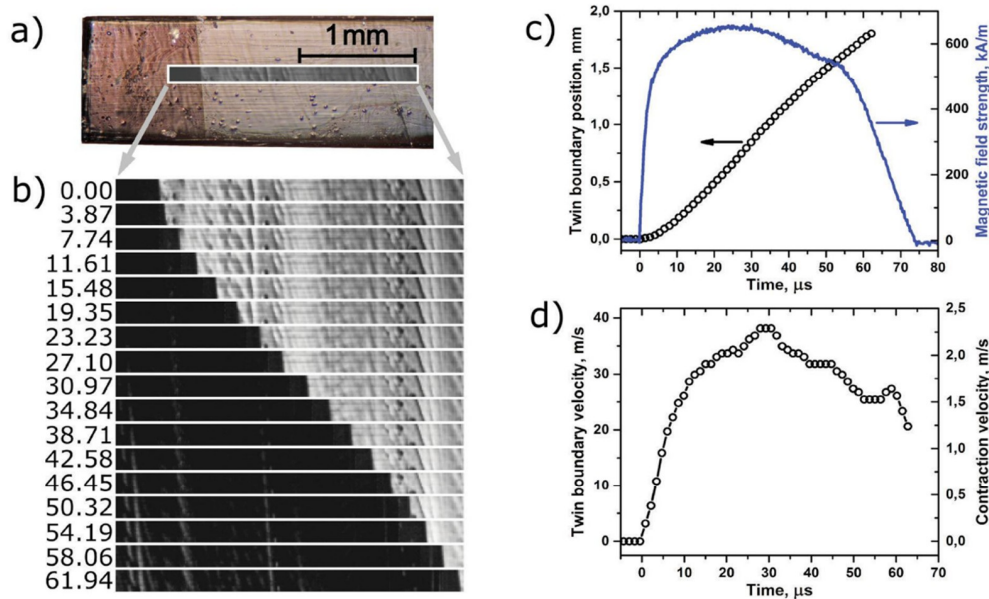


Fig. 2: (a) Optical top-view image of the sample with a single TB of type II before the pulse. The area captured by the high-speed camera is outlined. (b) High-speed camera images acquired during the pulse (each third frame shown). Timestamps are in μs . (c) TB position dependence on time (open circles, left axis) and magnetic field pulse (solid line, right axis) used. (d) TB velocity v_{TB} calculated from the TB position data (left axis). Right axis shows the corresponding scale for the contraction velocity v_C .

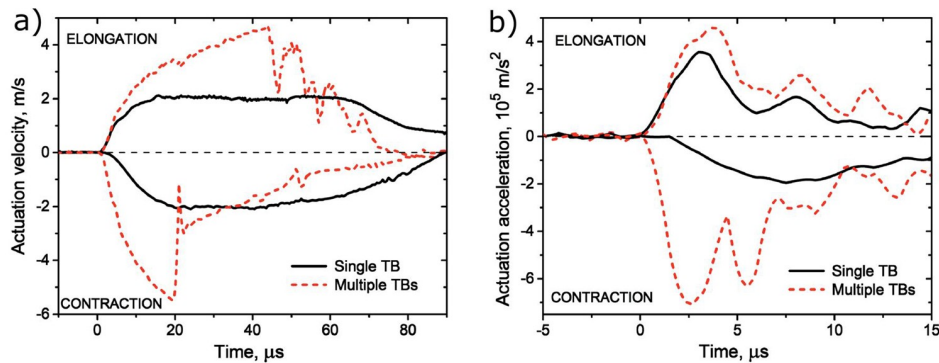


Fig. 3: (a) Actuation velocity measurements for single TB (solid lines) and multiple TBs (dashed lines) motion under pulsed magnetic field excitation. Positive values correspond to elongation mode, and negative values – for contraction mode. (b) Actuation acceleration numerically derived from the velocity data for single TB and multiple TBs motion.

In addition to contraction mode, we explored elongation of the sample in perpendicular magnetic field. Twin variants arrangement was done according to Fig. 1c, and the Helmholtz coil was rotated by 90° , in comparison to the setup described in Fig. 1a. The maximum elongation velocity was measured to be 2.1 m/s, which corresponds to the TB velocity of the magnitude similar to the contraction mode. We also tried to actuate motion of multiple TBs under pulsed magnetic field excitation. Here we introduced a few bands of the second twin variant by a mechanical stress. All TBs between different variants were of type II. The number of TBs varied from 3 to 5.

Fig. 3a summarizes the results on actuation velocity measurements, obtained for contraction and elongation modes, for single TB and multiple TBs motion. As it is seen from the graphs, in the case of multiple TBs motion, the actuation velocity can be significantly increased due to the simultaneous motion of the introduced TBs, in comparison with single TB motion. Nevertheless, the extended acceleration region points to the limiting effect of inertia.

Fig. 3b shows actuation acceleration curves derived numerically from the actuation velocity data. These graphs demonstrate accelerations up to 3.5×10^5 and 7×10^5 m/s², for single TB and multiple TBs motion, respectively.

In conclusion, we have directly observed for the first time fast-moving type II twin boundaries in Ni-Mn-Ga 5M martensite at RT using high-speed camera imaging. The TB velocities and corresponding contraction velocities achieved are 35–39 m/s and 2.1–2.3 m/s, respectively. The measured response time is less than 1 μ s, which is the shortest one reported for TB motion in Ni-Mn-Ga. In the case of multiple twin boundaries motion, actuation velocities

of 4–5.5 m/s and actuation accelerations of $(4-7) \times 10^5$ m/s² were observed. Inertia and internal friction significantly affect the TB dynamics at the measured speeds.

The reported results have a large potential for the development of new applications based on the MSM material, especially in microscale devices where the working frequency can be significantly increased. Example applications include fast optical and electrical switches, pneumatic/hydraulic valves, microfluidic pumps and valves, micromanipulators and grippers.

The authors would thank Kim Törnqvist (Cheos Oy, Finland) for providing the high-speed camera. This work was financially supported by the Academy of Finland (grant number 277996).

References

- [1] S.J. Murray, M. Marioni, S.M. Allen, R.C. O’Handley, *Appl. Phys. Lett.* 77 (2000) 886–888
- [2] A. Sozinov, A.A. Likhachev, N. Lanska, K. Ullakko, *Appl. Phys. Lett.* 80 (2002) 1746–1748
- [3] M.A. Marioni, R.C. O’Handley, S.M. Allen, *Appl. Phys. Lett.* 83 (2003) 3966–3968
- [4] K. Ullakko, J.K. Huang, C. Kantner, R.C. O’Handley, V.V. Kokorin, *Appl. Phys. Lett.* 69 (1996) 1966–1968
- [5] A. Sozinov, N. Lanska, A. Soroka, L. Straka, *Appl. Phys. Lett.* 99 (2011) 124103(1-3)
- [6] A. Saren, D. Musiienko, A.R. Smith, K. Ullakko, *Scripta Mat.* 113 (2016) 154–157

ACTA UNIVERSITATIS LAPPEENRANTAENSIS

791. WU, JING. Soft computing methods for performance improvement of EAMA robot in fusion reactor application. 2018. Diss.
792. VOSTATEK, PAVEL. Blood vessel segmentation in the analysis of retinal and diaphragm images. 2018. Diss.
793. AJO, PETRI. Hydroxyl radical behavior in water treatment with gas-phase pulsed corona discharge. 2018. Diss.
794. BANAEIANJAHROMI, NEGIN. On the role of enterprise architecture in enterprise integration. 2018. Diss.
795. HASHEELA-MUFETI, VICTORIA TULIVAYE. Empirical studies on the adoption and implementation of ERP in SMEs in developing countries. 2018. Diss.
796. JANHUNEN, SARI. Determinants of the local acceptability of wind power in Finland. 2018. Diss.
797. TEPLOV, ROMAN. A holistic approach to measuring open innovation: contribution to theory development. 2018. Diss.
798. ALBATS, EKATERINA. Facilitating university-industry collaboration with a multi-level stakeholder perspective. 2018. Diss.
799. TURA, NINA. Value creation for sustainability-oriented innovations: challenges and supporting methods. 2018. Diss.
800. TALIKKA, MARJA. Recognizing required changes to higher education engineering programs' information literacy education as a consequence of research problems becoming more complex. 2018. Diss.
801. MATTSSON, ALEKSI. Design of customer-end converter systems for low voltage DC distribution from a life cycle cost perspective. 2018. Diss.
802. JÄRVI, HENNA. Customer engagement, a friend or a foe? Investigating the relationship between customer engagement and value co-destruction. 2018. Diss.
803. DABROWSKA, JUSTYNA. Organizing for open innovation: adding the human element. 2018. Diss.
804. TIAINEN, JONNA. Losses in low-Reynolds-number centrifugal compressors. 2018. Diss.
805. GYASI, EMMANUEL AFRANE. On adaptive intelligent welding: Technique feasibility in weld quality assurance for advanced steels. 2018. Diss.
806. PROSKURINA, SVETLANA. International trade in biomass for energy production: The local and global context. 2018. Diss.
807. DABIRI, MOHAMMAD. The low-cycle fatigue of S960 MC direct-quenched high-strength steel. 2018. Diss.
808. KOSKELA, VIRPI. Tapping experiences of presence to connect people and organizational creativity. 2018. Diss.
809. HERALA, ANTTI. Benefits from Open Data: barriers to supply and demand of Open Data in private organizations. 2018. Diss.

810. KÄYHKÖ, JORMA. Erityisen tuen toimintaprosessien nykytila ja kehittäminen suomalaisessa oppisopimuskoulutuksessa. 2018. Diss.
811. HAJIKHANI, ARASH. Understanding and leveraging the social network services in innovation ecosystems. 2018. Diss.
812. SKRIKO, TUOMAS. Dependence of manufacturing parameters on the performance quality of welded joints made of direct quenched ultra-high-strength steel. 2018. Diss.
813. KARTTUNEN, ELINA. Management of technological resource dependencies in interorganizational networks. 2018. Diss.
814. CHILD, MICHAEL. Transition towards long-term sustainability of the Finnish energy system. 2018. Diss.
815. NUTAKOR, CHARLES. An experimental and theoretical investigation of power losses in planetary gearboxes. 2018. Diss.
816. KONSTI-LAAKSO, SUVI. Co-creation, brokering and innovation networks: A model for innovating with users. 2018. Diss.
817. HURSKAINEN, VESA-VILLE. Dynamic analysis of flexible multibody systems using finite elements based on the absolute nodal coordinate formulation. 2018. Diss.
818. VASILYEV, FEDOR. Model-based design and optimisation of hydrometallurgical liquid-liquid extraction processes. 2018. Diss.
819. DEMESA, ABAYNEH. Towards sustainable production of value-added chemicals and materials from lignocellulosic biomass: carboxylic acids and cellulose nanocrystals. 2018. Diss.
820. SIKANEN, EERIK. Dynamic analysis of rotating systems including contact and thermal-induced effects. 2018. Diss.
821. LIND, LOTTA. Identifying working capital models in value chains: Towards a generic framework. 2018. Diss.
822. IMMONEN, KIRSI. Ligno-cellulose fibre poly(lactic acid) interfaces in biocomposites. 2018. Diss.
823. YLÄ-KUJALA, ANTTI. Inter-organizational mediums: current state and underlying potential. 2018. Diss.
824. ZAFARI, SAHAR. Segmentation of partially overlapping convex objects in silhouette images. 2018. Diss.
825. MÄLKKI, HELENA. Identifying needs and ways to integrate sustainability into energy degree programmes. 2018. Diss.
826. JUNTUNEN, RAIMO. LCL filter designs for parallel-connected grid inverters. 2018. Diss.
827. RANAEI, SAMIRA. Quantitative approaches for detecting emerging technologies. 2018. Diss.
828. METSO, LASSE. Information-based industrial maintenance - an ecosystem perspective. 2018. Diss.

Acta Universitatis
Lappeenrantaensis
829



ISBN 978-952-335-304-6
ISBN 978-952-335-305-3 (PDF)
ISSN-L 1456-4491
ISSN 1456-4491
Lappeenranta 2018
